Affordable Flexible Hybrid Manipulator for Miniaturised Product Assembly

Xavier Herpe

Submitted for the degree of Doctor of Philosophy

Heriot-Watt University
Institute of Mechanical, Process and Energy Engineering
School of Engineering and Physical Sciences
May 2018

ABSTRACT

Miniaturised assembly systems are capable of assembling parts of a few millimetres in size with an accuracy of a few micrometres. Reducing the size and the cost of such a system while increasing its flexibility and accuracy is a challenging issue. The introduction of hybrid manipulation, also called coarse/fine manipulation, within an assembly system is the solution investigated in this thesis. A micro-motion stage (MMS) is designed to be used as the fine positioning mechanism of the hybrid assembly system. MMSs often integrate compliant micro-motion stages (CMMSs) to achieve higher performances than the conventional MMSs. CMMSs are mechanisms that transmit an output force and displacement through the deformation of their structure. Although widely studied, the design and modelling techniques of these mechanisms still need to be improved and simplified.

Firstly, the linear modelling of CMMSs is evaluated and two polymer prototypes are fabricated and characterised. It is found that polymer based designs have a low fabrication cost but not suitable for construction of a micro-assembly system. A simplified nonlinear model is then derived and integrated within an analytical model, allowing for the full characterisation of the CMMS in terms of stiffness and range of motion. An aluminium CMMS is fabricated based on the optimisation results from the analytical model and is integrated within an MMS. The MMS is controlled using dual-range positioning to achieve a low-cost positioning accuracy better than 2µm within a workspace of $4.4\times4.4mm^2$. Finally, a hybrid manipulator is designed to assemble mobile-phone cameras and sensors automatically. A conventional robot manipulator is used to pick and place the parts in coarse mode while the aluminium CMMS based MMS is used for fine alignment of the parts. A high-resolution vision system is used to locate the parts on the substrate and to measure the relative position of the manipulator above MMS using a calibration grid with square patterns. The overall placement accuracy of the assembly system is ±24µm at 3σ and can reach 2µm, for a total cost of less than £50k, thus demonstrating the suitability of hybrid manipulation for desktop-size miniaturised assembly systems.

The precision of the existing system could be significantly improved by making the manipulator stiffer (i.e. preloaded bearings…) and adjustable to compensate for misalignment. Further improvement could also be made on the calibration of the vision system. The system could be either scaled up or down using the same architecture while adapting the controllers to the scale.

ACKNOWLEDGEMENTS

Firstly, I would like to thank my supervisors Dr. Xianwen Kong and Dr. Matthew Dunnigan for their help as well as their technical and financial support through my whole PhD project. I would also like to thank Heriot-Watt University for awarding me the James Watt Scholarship, allowing me to meet my financial needs, and the support from the Engineering and Physical Sciences Research Council (EPSRC), UK under Grant No. EP/K018345/1, without which the project wouldn't even exist.

A particular thank you to the STMicroelectronics staff, Colin Campbell and Joseph Hannan for their technical support, especially for providing me with test parts.

Thank you to all the members of staff of Heriot-Watt University, technicians and researchers, who contributed to my work with their advice, technical expertise and equipment.

Thank you to my co-worker Dr. Ross Walker for his valuable contribution to my project. In particular for helping me writing my papers and solving engineering problems.

More importantly, I would like to thank the people who led me where I am, without whom none of this would have been possible. Firstly, my grandfather, Jean Vuidepot, who gave me the first kick and changed a potential failure in high school to a success at the highest level of education. Then, my parents, Béatrice and Didier Herpe, who have been supporting me for 28 years at every step of my life. Finally, my best friends, Craig Ewing and Guillaume Danjou, for making these three years feel like a fun time. They are my role models and their success in life pushes me to work harder.

Last but not least, I would like to thank my wife to be, Susan Roozbeh. She shared my PhD life and was there for me in good and bad times.

ACADEMIC REGISTRY
Research Thesis Submission

Name*:*			
School:			
Version: *(i.e. First, Resubmission, Final)*		Degree Sought:	

Declaration

In accordance with the appropriate regulations I hereby submit my thesis and I declare that:

1) the thesis embodies the results of my own work and has been composed by myself
2) where appropriate, I have made acknowledgement of the work of others and have made reference to work carried out in collaboration with other persons
3) the thesis is the correct version of the thesis for submission and is the same version as any electronic versions submitted*.
4) my thesis for the award referred to, deposited in the Heriot-Watt University Library, should be made available for loan or photocopying and be available via the Institutional Repository, subject to such conditions as the Librarian may require
5) I understand that as a student of the University I am required to abide by the Regulations of the University and to conform to its discipline.
6) I confirm that the thesis has been verified against plagiarism via an approved plagiarism detection application e.g. Turnitin.

* *Please note that it is the responsibility of the candidate to ensure that the correct version of the thesis is submitted.*

Signature of Candidate*:*		Date:	

Submission

Submitted By *(name in capitals):*	
Signature of Individual Submitting:	
Date Submitted:	

For Completion in the Student Service Centre (SSC)

Received in the SSC by *(name in capitals):*			
Method of Submission *(Handed in to SSC; posted through internal/external mail):*			
E-thesis Submitted (***mandatory for final theses***)			
Signature:		Date:	

TABLE OF CONTENTS

ABSTRACT ii
ACKNOWLEDGEMENTS iii
TABLE OF CONTENTS v
LIST OF ABBREVIATIONS viii
LIST OF FIGURES ix
LIST OF TABLES xiii
LIST OF PUBLICATIONS xiv
Chapter 1 Introduction 1
1.1 Background 1
1.2 Objectives 2
1.3 Thesis Structure 2
Chapter 2 Literature Review 5
2.1 Assembly Systems 5
2.1.1 Micro-Assembly Systems 7
2.1.2 Desktop Micro-Factories 9
2.1.3 Hybrid Manipulators 12
2.1.4 Grippers 13
2.2 Compliant Mechanisms in Micro-Motion Systems 15
2.2.1 Compliant Mechanisms 16
2.2.2 Common Types of joint 17
2.2.3 Compliant Joints Integrated to Conventional Parallel Robots 20
2.2.4 Compliant Micro-Motion Stages 22
2.2.5 Material and Fabrication of Compliant Mechanisms 24
2.2.6 Modelling and Analysis of Compliant XY Stages 25
2.3 Dual-Range Motion Stages 28
2.4 Actuation and Sensing for Micro-Motion 32
2.4.1 Actuators 32
2.4.2 Sensors 33
2.5 Summary 34
Chapter 3 Linear Modelling and Characterisation of a Compliant Micro-Motion XY Stage 35
3.1 Linear Modelling of a Compliant XY Stage 35

3.1.1 Pseudo-Rigid Body Model 36
3.1.2 Euler-Bernoulli Model 37
3.1.3 Travel Range Limitations 38
3.1.4 Evaluation of the Linear Model Using FEA 40
3.2 Characterisation of a PLA Compliant Stage 45
3.2.1 Frequency Response Analysis 45
3.2.2 Force-Displacement Test 47
3.3 Characterisation of a Nylon-66 Compliant Stage 48
3.3.1 Travel Range Limitation 49
3.3.2 Motion Loss analysis 50
3.3.3 Force-Displacement Analysis 51
3.3.4 Dynamic Analysis 52
3.4 Summary 53
Chapter 4 Nonlinear Modelling and Characterisation of a Compliant Micro-Motion XY Stage 54
4.1 Nonlinear Modelling of a Compliant Stage 54
4.1.1 Stiffness Modelling 54
4.1.2 Travel Range Limitations 61
4.2 Dynamic Model of a Compliant XY Stage 62
4.2.1 Stiffness Matrix 62
4.2.2 Dynamic Model 65
4.3 Design Optimisation 66
4.4 Evaluation of the Nonlinear Model Using FEA 69
4.4.1 Force-Displacement Analysis 69
4.4.2 Stress Analysis 70
4.4.3 Buckling Analysis 71
4.4.4 Coupling Analysis 72
4.4.5 Modal Analysis 74
4.5 Fabrication and Characterisation of an Aluminium-7075 T6 Compliant XY Stage 75
4.5.1 Force-Displacement Test 76
4.5.2 Coupling Test 77
4.5.3 Frequency Response 77
4.6 Summary 78

Chapter 5 Implementation and Testing of a Dual-Range Manipulator Using the Fabricated Compliant Micro-Motion XY Stage 80
5.1 First Prototype Using the Initial Design of the Compliant Stage 80
5.1.1 Open-Loop Behaviour 81
5.1.2 Dual-Range Positioning 83
5.2 Second Prototype Using the Final Design of the Compliant Stage 87
5.2.1 Input Position Control 88
5.2.2 Dual-Range Positioning 89
5.3 Summary 90
Chapter 6 Hybrid Manipulator 92
6.1 Pick-and-Place Manipulator 92
6.2 Vision System 94
6.2.1 Strategy 94
6.2.2 Camera Location 97
6.2.3 Part Location 97
6.3 Control System 98
6.4 Calibration 99
6.4.1 Vision System Calibration 99
6.4.2 Gripper Offset 101
6.5 Design for Automated Assembly 102
6.6 Position Accuracy and Assembly Test 104
6.6.1 Measurement Accuracy of the Vision System 104
6.6.2 Assembly Tests 106
6.6.3 Positioning Accuracy 108
6.7 Summary 109
Chapter 7 Conclusion and Outlook 111
7.1 Summary 111
7.2 Contribution 113
7.3 Future Work 113
7.3.1 Micro-Motion XY Stage 113
7.3.2 Hybrid Assembly System 114
REFERENCES 117

LIST OF ABBREVIATIONS

Abbreviation	Full name
VCA	Voice Coil Actuator
DOF	Degree Of Freedom
AFM	Atomic Force Microscope
SCARA	Selective Compliance Assembly Robot Arm
PCB	Printed Circuit Board
PKM	Parallel Kinematic Machine
FFT	Fast Fourier Transform
PZT	Lead Zirconate Titanate
WEDM	Wire Electric Discharge Machining
BCM	Beam Constraint Model
LVDT	Linear Variable Differential Transformer
CAD	Computer Aided Design
PLA	Polylactic Acid
CMM	Coordinate Measurement Machine
CNC	Computer Numerical Control
CMMS	Compliant Micro-Motion Stage
MMS	Micro-Motion Stage
PRBM	Pseudo-Rigid Body Model

LIST OF FIGURES

Figure 2.1 Micro-assembly system Chronogrip®, courtesy of Pecipio Robotics.....7
Figure 2.2 Modular assembly station from [47].....10
Figure 2.3 Miniaturised SCARA robot from [23].....10
Figure 2.4 PocketDelta® robot from [28] used in [17].....11
Figure 2.5 Hybrid manipulator from [26] 13
Figure 2.6 Capillary force gripper from [11] 14
Figure 2.7 Vacuum gripper used on a miniature SCARA robot [79] 14
Figure 2.8 Conventional mechanical gripper from [5] 15
Figure 2.9 Typical leaf-spring flexure hinge.....17
Figure 2.10 Typical notch-type flexure hinges, (a) Right angle, (b) Elliptic, (c) Circular 17
Figure 2.11 Common parallelogram structures. (a) Basic parallelogram. (b) Double parallelogram. (c) Compound basic parallelogram. (d) Compound double parallelogram 20
Figure 2.12 End effector of a DELTA robot with large displacement flexure hinge from [85].....21
Figure 2.13 MMS driven by electromagnetic actuators from [120] 23
Figure 2.14 MMS driven by VCAs from [129] 24
Figure 2.15 PRBM of a basic parallelogram.....26
Figure 2.16 Spring equivalent model for the stiffness matrix from [108] 27
Figure 2.17 BCM from [109].....27
Figure 2.18 Dual-range MMS from [169].....30
Figure 2.19 Dual-range MMS from [176].....31
Figure 2.20 Dual-range MMS from [156].....32
Figure 3.1 Conceptual design of the first CMMS.....36
Figure 3.2 Pseudo-Rigid Body Model of a single beam 37
Figure 3.3 Euler-Bernoulli beam deflection model of a single beam 37
Figure 3.4 Buckling force diagram 39
Figure 3.5 Beam dimensional parameters.....40
Figure 3.6 a) FEA of the force-displacement relationship compared with the analytical models, b) Error from comparison with analytical models.....41
Figure 3.7 a) FEA with variable beam's length, b) FEA with variable beam's width.....41

Figure 3.8 Buckling point when a load is applied along Y 42
Figure 3.9 Stress analysis of the CMMS a) in comparison with analytical models b) with variable beam's length, c) with variable beam's width. 43
Figure 3.10 Deformed CMMS with input displacement applied along X and Y directions 44
Figure 3.11 a) Y-Displacement with and without preload, b) Cross-axis coupling. 44
Figure 3.12 Frequency response of the CMMS for different a) beam's widths, b) beam's lengths. 45
Figure 3.13 Vibration testing setup 46
Figure 3.14 Frequency response of the 3-D printed CMMS with a) One accelerometer, b) Two accelerometers 47
Figure 3.15 a) Loading Test Rig, b) Experimental results compared to FEA results of the 3d-printed CMMS loading test. 48
Figure 3.16 Dimensions of the Nylon-66 CMMS 48
Figure 3.17 Fabricated Nylon-66 CMMS 49
Figure 3.18 Stress and output displacement response to a large input displacement 50
Figure 3.19 Output displacement error for single direction loading 51
Figure 3.20 Loading test of the fabricated CMMS 52
Figure 3.21 Vibration test rig 53
Figure 4.1 Schematic top view of the CMMS 55
Figure 4.2 Nonlinear spring-equivalent model of the CMMS 56
Figure 4.3 Spring-equivalent model of a beam 56
Figure 4.4 Spring-equivalent model of orthogonal beam configuration 58
Figure 4.5 Buckling: a) Force diagram, b) FEA result 62
Figure 4.6 Coordinate transformation 63
Figure 4.7 Properties of the CMMS as a function of the height, length and thickness of the beams. a) first and second resonant frequencies, b) third resonant frequency, c) maximum displacement, d) input force. (NB: each layer corresponds to a different beam thickness between 0.5mm and 1mm) 67
Figure 4.8 Pareto front 69
Figure 4.9 Stiffness along a single direction 70
Figure 4.10 Stress concentration coefficients in function of the beam’s thickness and length 71
Figure 4.11 Stress analysis: linear and nonlinear models compared with FEA 71

Figure 4.12 Stress and output displacement response to a large input displacement 72
Figure 4.13 Deformed CMMS with input displacement applied along X and Y directions 72
Figure 4.14 Parasitic displacement for single direction loading 73
Figure 4.15 Input/output displacement difference after applying a preload along the Y-axis 73
Figure 4.16 Modal analysis results from FEA 74
Figure 4.17 Fabricated Aluminium-7075 T6 CMMS 75
Figure 4.18 Fabricated MMS. 1) Linear actuator, 2) Capacitive sensor head, 3) CMMS, 4) Target, 5) Moving Platform 6) Linear encoder, 7) VCA.....76
Figure 4.19 Experimental vibration test setup. 1) Data acquisition card, 2) Amplifier, 3) 3D accelerometer, 4) CMMS 78
Figure 5.1 First prototype of the MMS 81
Figure 5.2 CMM test rig with 1) Probe, 2) MMS, 3) Control electronics, 4) Control software 81
Figure 5.3 CMM measurements for a single direction loading 82
Figure 5.4 CMM measurements of the parasitic displacement compared with FEA 83
Figure 5.5 Exploded view of the dual-range MMS with 1) CMMS, 2) Linear actuator, 3) Capacitive sensor head, 4) Linear encoder, 5) VCA.....84
Figure 5.6 Control system of the dual-range MMS 85
Figure 5.7 Measuring points of the MMS within the workspace (scaled up).....86
Figure 5.8 Fabricated dual-range MMS 88
Figure 5.9 Fine positioning control loop for the MMS.....89
Figure 5.10 Capacitive sensors readings in fine positioning mode along a) the X-axis at position 0mm, b) the Y-axis at position 0mm, c) the X-axis at position 2.2mm, d) the Y-axis at position 2.2mm 90
Figure 6.1 Pick-and-place manipulator: 1-X and Y belt drives, 2-Z screw drive, 3-Motorised lens/focus system, 4-Camera, 5-Ring light, 6- θ drive, 7-Picker head.....93
Figure 6.2 Hybrid miniaturised products assembly system: 1-Fine positioning mechanism, 2-Coarse positioning mechanism.....94
Figure 6.3 Fabricated MMS with assembly substrate: 1-Linear actuator, 2-Capacitive sensor head, 3-Moving Platform, 4-Target, 5-CMMS, 6-Backlight, 7-Linear encoder, 8-VCA, 9-Parts to assemble, 10-Assembly area with tape, 11-Mask, 12-Grid.....96
Figure 6.4 Vision system's line detection function.....98

Figure 6.5 Vision system's part location function 98
Figure 6.6 Control System of the hybrid manipulator 99
Figure 6.7 Calibration of the vision system: a) Line detection of one square on the grid and b) Coordinates determination of the points 100
Figure 6.8 Calibration verification: a) 1mm distance and b) 5mm distance 101
Figure 6.9 Offset measurement between the gripper tip and the camera 102
Figure 6.10 Sequence diagram of the assembly program 103
Figure 6.11 Line reading accuracy path 105
Figure 6.12 Part reading accuracy path 105
Figure 6.13 Histogram of the reading error for: a) the position error along X, b) the position error along Y 107
Figure 6.14 Assembly of a lens into a holder 107
Figure 6.15 Scatter attained position 109

LIST OF TABLES

Table 2.1 Comparison of micro-assembly systems.....6
Table 3.1 Initial geometrical parameters for the Nylon CMMS 49
Table 4.1 Masses of a beam, inner, and outer parallelogram.....66
Table 4.2 Parameters of the CMMS.....68
Table 4.3 Resulting resonant frequencies 75
Table 5.1 Sensors rating.....84
Table 5.2 Accuracy and repeatability of the Nylon-66 MMS.....87
Table 6.1 Gantry drives specifications.....94
Table 6.2 Attained positions, accuracy and repeatability of the hybrid manipulator ...110
Table 7.1 Cost estimation.....112

LIST OF PUBLICATIONS

Journal Papers

[1] **X. Herpe**, R. Walker, M. Dunnigan, and X. Kong, "*On a Simplified Nonlinear Analytical Model for the Characterisation and Design Optimisation of a Compliant XY Micro-Motion Stage*," Robotics and Computer Integrated Manufacturing, vol. 49, pp. 66-76, 2017.

[2] **X. Herpe**, M. Dunnigan, and X. Kong, "*Design, Fabrication and Testing of a Dual-Range XY Micro-Motion Stage Driven by Voice Coil Actuators*," Advances in Science, Technology and Engineering Systems Journal (ASTESJ), vol. 2(3), pp. 498-504, 2017.

Conference Papers

[1] **X. Herpe**, R. Walker, M. Dunnigan, and X. Kong, "*Design, Fabrication and Testing of a Hybrid Micro-motion XY stage Driven by Voice Coil Actuators*," in Proceeding of the International Conference for Students on Applied Engineering (ICSAE), 2016, pp. 153-158. Best Student Paper Award

[2] **X. Herpe**, R. Walker, M. Dunnigan, and X. Kong, "*Analysis and characterisation of a kinematically decoupled compliant XY stage*," in Proceeding of the 21st International Conference on Automation and Computing (ICAC), 2015, pp. 1-6. Best Student Paper Award

Chapter 1 Introduction

Nowadays, there is a growing tendency for product miniaturisation and the perpetual need for agile changeover to meet the rapid production changes in the manufacturing sector. This led to a need for on-demand/single-component prototyping and production systems. Although the existing miniaturised product assembly systems can reach the micrometre scale accuracy, they are costly and have a low flexibility, making them only suitable for medium to large production applications. There is therefore a need to develop compact, flexible and affordable systems for miniaturised product assembly.

1.1 Background

Assembly systems capable of assembling thousands of parts a day using a parallel configuration are extremely costly, have very little flexibility, a large footprint and a limited placement accuracy. They are only used for mass production. Serial assembly systems with a lower throughput can offer fully automated assembly of miniaturised components with higher flexibility, accuracy and a smaller footprint. However, the cost of these systems can reach a few hundreds of thousands of sterling pounds. Smaller systems used for small batch production or prototyping are available but the ratio between accuracy, cost and workspace is not always optimal [1-3]. That is why new, compact and cheap assembly systems with a low throughput but a high accuracy and high flexibility need to be developed.

Micro-motion stages (MMSs) offer a great potential for low-cost high accuracy positioning [4] and can be implemented within a micro-assembly system, thus resulting in a hybrid manipulator [5]. Although a multitude of compliant micro-motion stages (CMMSs) have been developed in the past decade, several challenges still need to be overcome, including the modelling of compliant mechanisms and their control as well as cost reduction.

The assembly system presented in this thesis is designed to assemble mobile phone cameras and their associated sensors, such as time-of-flight sensors. The application of the presented assembly system can be extended to parts of similar size such as printed circuit board (PCB) components and miniaturised sensors. By scaling down the system and increasing the position resolution and stiffness of the sub-systems while keeping the same concept of hybrid manipulation and the same control system architecture, the

application could be extended to systems smaller than 1mm requiring a placement accuracy of less than 1µm.

1.2 Objectives

Although a multitude of assembly systems exist, they are often large, costly, and are suitable for mass or batch production. The aim of the project is to fabricate an assembly system that can fit on a desktop, costs less then £50,000 to fabricate and can manipulate a wide range of parts without requiring any major modification. The target parts sizes are between 1mm and 10mm in width and between 0.2mm and 6mm in thickness. The test parts, provided by STMicroelectronics, must be picked from the top, orientated about the Z-axis with an accuracy greater than 1° and stacked on the top of each other with an overall positioning accuracy greater than 5µm. To achieve such a high positioning accuracy at such a low cost, the concept of hybrid manipulation will be used by integrating an MMS. A simplified modelling technique of CMMS will be developed to design a dual-range MMS with a target positioning accuracy of 1µm.

1.3 Thesis Structure

The thesis is structured as follows:

Chapter 1 introduces the thesis. The background, objectives and design constraints of the project are summarised. Chapter 2 gives a review of recently developed micro-assembly systems and desktop assembly systems, followed by an in-depth review of CMMSs, their design, modelling techniques and application. In Chapter 3, the first design of a CMMS is presented, from linear modelling to prototype testing. A final design is presented in Chapter 4 with an analytical model, including a simplified nonlinear stiffness model, used for design optimisation. The fabricated CMMS is then implemented in a dual-range MMS in Chapter 5. Chapter 6 presents the hybrid manipulator consisting of the pick-and-place robot, the fabricated MMS, the vision system and its calibration, the control system architecture, the assembly tests and the overall placement accuracy of the manipulator. Finally, conclusions are drawn in Chapter 7 and future work is presented.

Chapter 1: *Introduction*. This chapter introduces the thesis, setting up the scope of study, the limitations and the design constraints, and detailing the structure of the thesis.

Chapter 2: *Literature Review*. The first part of the literature survey covers the current status of micro-assembly systems, followed by a review of the existing desktop assembly systems and finishing with an overview of the gripping techniques used for miniaturised products. The second part of the literature review focuses on compliant mechanisms and their application in CMMS. The latest developed CMMSs are reviewed and particular attention is given to the stiffness modelling techniques and their limitations. The last part of the literature review concerns the study of dual-range MMSs, which often include a CMMS. The latest developed dual-range MMSs are presented along with their actuation and sensing methods.

Chapter 3*: Linear Modelling and Characterisation of a Compliant Micro-Motion XY Stage*. A CMMS is designed and two linear models are derived, the first one based on the Pseudo-Rigid Body Model (PRBM) and the second one based on the Euler-Bernoulli model. Finite Element Analysis (FEA) is then carried out to evaluate these two models and to fully characterise the designed CMMS in terms of working range, stiffness, kinematic coupling and resonant frequencies. A first prototype is then proposed to evaluate the design, and a second prototype is built at full scale using polymer rather than metal and abrasive jet machining instead of Wire Electric Discharge Machining (WEDM). The test results show a potential for a low cost CMMS but with changing and unpredictable material properties

Chapter 4: *Nonlinear Modelling and Characterisation of a Compliant Micro-Motion XY Stage*. To compensate for the large errors observed in Chapter 3 between the linear models and FEA, a simplified nonlinear model is proposed here. Combined with a linear model used for a dynamic analysis, this analytical model is used for design optimisation and a final CMMS is fabricated using WEDM. The CMMS is then characterised and the results are compared with FEA and the analytical model. As the results are all in accordance, the analytical model can be used for the characterisation and design optimisation of CMMS with a similar structure.

Chapter 5: *Implementation and Testing of a Dual-Range Manipulator Using the Fabricated Compliant Micro-Motion XY Stage*. The CMMS fabricated in Chapter 3 is integrated to a first prototype of a dual-range MMS. The kinematic coupling is then evaluated and dual-range sensing is used to compensate the positioning error of the MMS. As the results are promising, a final dual-range MMS is fabricated using the CMMS described in Chapter 4 and the positioning accuracy of the MMS is measured.

Chapter 6: *Hybrid Manipulator*. A hybrid manipulator is designed, comprising a pick-and-place robot for the coarse positioning, the dual-range MMS fabricated in Chapter 5 for the fine positioning and a high-resolution vision system for part detection and visual servoing. The control system is briefly presented and the automatic assembly procedure is explained. The calibration of the vision system is detailed and its measuring uncertainty is estimated. Finally, an assembly test is carried out and the overall positioning accuracy is measured.

Chapter 7: *Conclusion and Outlook*. The contribution of the thesis is summarised in this chapter and some future work is proposed for further development and improvement of the hybrid manipulator.

Chapter 2Literature Review

This chapter outlines a survey of existing assembly systems, from micro-assembly systems to desktop-size miniaturised product assembly systems. An in-depth study of compliant mechanisms is then presented, with particular attention given to CMMSs and their modelling techniques. Recently developed dual-range MMSs are then detailed. Finally, a brief review of the actuation and sensing solutions used for micro-manipulation is presented.

2.1 Assembly Systems

Miniaturised product assembly is the process of manipulating and orientating small parts in order to assemble them, thus resulting in a miniaturised system that could not be assembled manually with the same level of accuracy. The main challenges are to achieve high precision within a large workspace with a wide manipulation capability and flexibility. Such a system must be capable of manipulating parts larger than one millimetre with an accuracy of more than 1μm. This is commonly called the mesoscale [6] and differs from microscale. Microscale applies to micro-assembly systems manipulating parts smaller than 1mm with an accuracy of less than 1μm. Miniaturised assembly tasks can be operated by human operators, either manually using tweezers or by using a robot, or automatically. A typical positioning accuracy for parts larger than 1mm is in a range of 10 to 25μm [6, 7]. Applications of miniaturised product assembly are numerous, from fibre alignment, wire bonding, Surface Mount Technology (SMT) assembly, microrobots, watch components and mini gearheads to gas sensors and mobile phone loudspeakers [8-17]. Several systems capable of accurately assembling micro-parts for prototyping purposes have been fabricated and evaluated over the past few years. This section presents an overview of these systems. The systems' workspaces and accuracies are listed in Table 2.1.

Reference	Vision Resolution	Workspace	DOF	Accuracy/ repeatability (manipulator)	Assembly Pose Accuracy (Overall)	Part Size
[6]	2μm/pix	Unknown	4	Coarse: 25μm	Unknown	Down to 50μm
[13]	640pix*480pix	Unknown	6	0.5±0.2μm (xy stage only)	Unknown	Down to 1mm (50μm thick)
[18]	3.2μm/pix	$8cm^3$	19	2±6μm (at 3σ) along Y	Unknown	Down to 800μm (100μm thick)
[19]	0.8μm/pix	$20mm^3$	6	2μm repeatability	Unknown	Less than 100μm
[5]		Unknown	4	±10μm	±35μm	126μm to 30mm
[11]	2μm/pix	Unknown	3	±2μm	Unknown	0.9mm to 1.6mm
[20]	1.54μm/pix to 0.56μm/pix	Unknown	4	μm scale (using PI stages)	±1μm	40μm to 100μm
[21]	0.4μm/pix to 0.25μm/pix	Unknown	4	μm scale (using PI stages)	±0.7μm	Unknown
[22]	19μm/pix	160 x 400 x $15mm^3$	4	0.6μm repeatability at 3σ	Unknown	Unknown
[23]	NA	60 x 45 x $20mm^3$	4	14μm repeatability (at 3σ)	Unknown	1mm
[24]	NA	60 x 45 mm^2	3	34μm repeatability (at 3σ)	Unknown	1mm
[25]	Unknown	400 x 160 x $130mm^3$	4	Unknown	Unknown	10 to 80mm
[26]	NA	$40mm^3$	3	10μm (max error)	Unknown	
[27]	Unknown	$40mm^3$	3	20μm	Unknown	3mm
[28] / [17]	Unknown	80 x 80 x $30mm^3$	4	5μm	Unknown	2mm to 12mm
[9]	Unknown	Unknown	4	Unknown	Unknown	Down to 1mm
[29]	Unknown	25 x 22 x $2mm^3$	4	Unknown	1μm	1.6mm down to 50μm
[30]	1μm/pix	$25mm^3$	4	Unknown	<1μm repeatability	1.3mm down to 100μm
[15]		Unknown	4	Unknown	Unknown	Unknown
[31]	Unknown	Unknown	6	Unknown	±3μm	mm scale
[32]	NA	Unknown	3	1μm repeatability	Unknown	5mm down to 0.5μm
[33]	1280x960pix - 0.95μm/pix	Unknown	5	Unknown	up to 0.3μm	400μm
[34]	1600x1200pix - 0.835μm/pix	Unknown	2	±2μm	Unknown	30μm
[16]	15.3μm/pix to 1.87μm/pix	Unknown	5	Unknown	up to 5μm	Unknown

Table 2.1 Comparison of micro-assembly systems

2.1.1 Micro-Assembly Systems

Typical micro-assembly systems usually have a workspace limited by the field of view (FOV) of the microscope/camera used to monitor the assembly. Most of the micro-assembly systems are not relevant to the application covered in this thesis, but some of them introduce interesting technologies and solutions that can be combined with larger scale solutions. These systems can assemble parts between 30μm and 1mm and can reach an overall positioning accuracy of less than 1μm. Although they have a very high accuracy and often have a six-degree-of-freedom (DOF) mobility, the FOV of the vision system is between a few hundred microns and a couple of millimetres, thus limiting the workspace. An example of a commercially available micro-assembly system having an accuracy of ±2μm is shown in Figure 2.1.

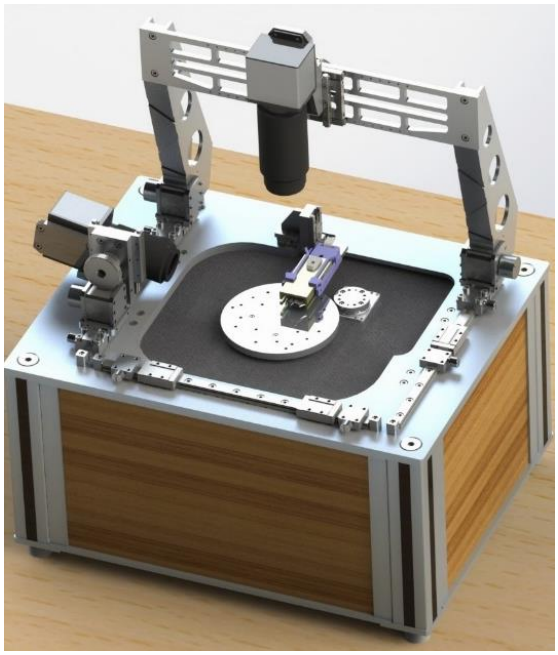

Figure 2.1 Micro-assembly system Chronogrip®, courtesy of Pecipio Robotics

The vision system of a micro-assembly system can be used as visual feedback for tele-operated assembly tasks. For instance, the system developed in [29] uses a gripper attached to a 3-DOF MMS to manipulate parts between 50μm and 1.6mm in size with a maximum accuracy of 1μm. Because the camera is attached to the MMS, the workspace covered corresponds to the workspace of the MMS, which is $25\times22mm^2$. The assembly system from [13] can manipulate 1mm parts with 6 DOFs and the MMSs used for the actuation allow for a positional accuracy of less than 1μm. The workspace in this case is

limited to the FOV of the fixed camera. The 4-DOF system from [18, 35] can assemble parts of 800µm with a positioning accuracy of 8µm within a workspace of $80\times80mm^2$. The system developed in [34] includes a compliant gripper mounted on the MMS from [36]. The test results show that parts as small as 30 microns can be aligned with an accuracy of ±2µm using visual servoing. The range of motion is nevertheless very small.

The vision system of a micro-assembly system can also be used for automatic assembly tasks using visual servoing and/or sometimes part recognition. For instance, the 6-DOF system presented in [31, 37-39] can perform a fully automatic assembly with an overall accuracy of 3µm. However, the range of parts manipulated is very limited. The vision system is only used for visual servoing as the initial location of the parts is known and the grippers are dedicated to the parts. The 4-DOF system presented in [40] can automatically assemble 4µm thick parts using two motion MMSs and a vision system. The FOV is limited to a few tens of microns and this system is only suitable for a very short range of motion. Visual servoing was also used in [33, 41], where the pose accuracy can reach 0.3µm for parts as small as 400 microns. However, the workspace is limited to the $1.216\times0.912mm^2$ FOV. In the work from [42], sub-millimetre parts can be automatically assembled with an accuracy better than 10µm. The FOV is $4.224\times5.632mm^2$, allowing for the manipulating of larger parts within a larger workspace. The system developed in [30] can manipulate parts between 100µm and 1.3mm with 6 DOFs and with an overall positioning accuracy of less than 1µm using three MMSs and four cameras. The actuators allow for a motion of 25mm along each direction but the workspace is limited by the FOV of the cameras. The vision system is used for visual servoing through pattern recognition. Another system developed in [19, 43-45] can manipulate parts of less than 100µm with 6 DOFs within a workspace of $20\times20mm^2$, with the camera being able to move above the substrate. The 4-DOF assembly system from [20, 21] can manipulate parts between 40µm and 100µm with an accuracy better than 1µm. The workspace is nevertheless also limited to the camera's FOV. The system developed in [11] to manipulate parts larger than 1mm has only 3-DOF and is composed of an MMS and a separate Z linear actuator. A higher simplicity means a higher accuracy, with an overall accuracy of 2µm for parts of sizes varying between 0.9mm and 1.6mm. Finally, the system developed in [16] can assemble fibres with an accuracy of 5µm by combining an active and a passive alignment mechanism. Two cameras are used for visual servoing of the fibre and the groove positions, allowing for automatic assembly.

2.1.2 Desktop Micro-Factories

Systems with less DOFs and lower accuracy but larger workspace and higher flexibility than the micro-assembly systems presented in Section 2.1.1 are more important in miniaturised assembly. Such systems can fit on a desktop and be integrated with other modules, resulting in what is commonly called desktop micro-factories. Micro-factories are made of compact modules carrying various manufacturing and assembly tasks [32, 46-53]. Conveyor belts, rotating platforms or planar motors are used to transfer parts between each substation. A multitude of miniaturised robotic manipulators such as DELTA or Selective Compliance Assembly Robot Arm (SCARA) robots have recently been developed for manipulating parts larger than 1mm using new available backlash-free gearings, mini servomotors, high precision sensors, etc. These systems usually cost no more than a few thousand sterling pounds, have a repeatability between 10µm and 34µm and have a footprint between $0.2\times0.2m^2$ and $0.5\times0.5m^2$. They are designed to fit within micro-factories and perform assembly tasks. Their workspace varies between $40\times40mm^2$ and $250\times250mm^2$. In most of the applications, the workspace of the manipulator does not need to be more than a few centimetres as the parts are often conveyed between different substations and are placed directly under the assembly station.

For instance, a compact modular assembly system was designed in [47]. The system consists of subsystems that are placed around a planar motor (Figure 2.2). The motor is used to convey the substrate between the subsystem with a positioning accuracy of 20µm. Each subsystem has its own purpose (handling, screwing, bonding…). The subsystems have no more than 3 DOFs as simple kinematics is crucial to ease the control and enhance the accuracy. A micro-factory was presented in [32] where parts are conveyed between the substations by a linear drive. The parts are between 0.5mm and 5mm in size and the positioning accuracy is better than 100µm.

[23, 54] designed a miniature SCARA robot (Figure 2.3) with 4 DOFs which can achieve a repeatability of 14µm within a $60\times45\times20mm^3$ workspace. The robot's footprint is $100\times53mm^2$. Based on this design, [24] presented a similar manipulator using Lead Zirconate Titanate (PZT) motors instead of DC motors in order to reduce the cost of the system. However, the repeatability was reduced to 34µm.

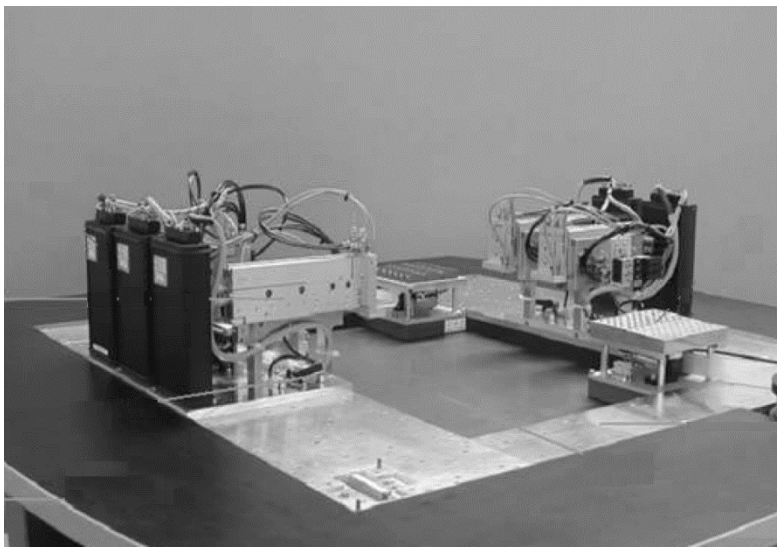

Figure 2.2 Modular assembly station from [47]

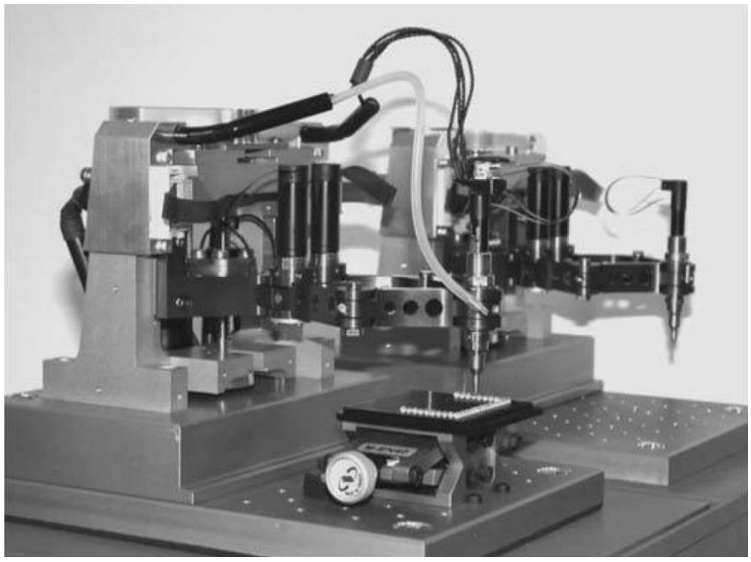

Figure 2.3 Miniaturised SCARA robot from [23]

A SCARA robot used for precision assembly was presented in [22]. The robot has a repeatability of 0.6μm and a vision system is used to monitor the position of the parts relative to each other. A combination of a 2-DOF Cartesian manipulator serially assembled to a 3-DOF parallel SCARA manipulator was developed in [8]. The Cartesian manipulator uses a motor-belt mechanism to reduce the moving mass, distributing the load on the fixed parts rather than the moving part. The footprint of the robot is $200\times300mm^2$, which is smaller than its $400\times160mm^2$ workspace, making it compact but capable of covering a large working range. The system features an interchangeable gripper with a standardised interface. The parts are simply picked from a feeding system, rotated by a sub-system and then picked and placed in the jigs of the chuck. The accuracy

and repeatability of this robot was reported to be poor, with most of the errors caused by significant backlash and low stiffness. This robot was used in [25] for assembling gas sensors. A similar 4-DOF miniature parallel SCARA based robot with an additional Z translation at its base was designed in [7]. This system was designed to be implemented within a modular micro-assembly line. The parts are conveyed between each station, assembled in a circular pattern to enhance the process. The workspace achieved is $200\times200\times45mm^3$ and the footprint is $250\times250\times75mm^3$. Another modular assembly system was designed in [5], including a 4-DOF robot manipulator and a 3-DOF MMS. The reconfigurability of the end-effector allows for manipulation of parts between 126μm and 30mm. A large working range is achieved with an accuracy of 35μm for chip alignment. A modular micro-assembly station was also designed in [26], including two miniaturised parallel manipulators. The first one is a miniaturised Delta robot which has a $40\times40\times40mm^3$ workspace and an accuracy greater than 10μm. The second robot from [26] is a miniaturised 4-DOF parallel SCARA manipulator. This robot includes a coarse vertical stage and the fine positioning stage is attached to the substrate. Another modular reconfigurable micro factory was developed in [27, 55], which uses two miniaturised DELTA robots to manipulate and assemble parts with an accuracy of 20μm within its $40\times40\times40mm^3$ workspace. The footprint of the micro factory is $500\times500\times460mm^3$. A similar micro factory was designed in [17] where the assembly module is based on a PocketDelta® robot developed in [28], with 5μm repeatability, a workspace of $80\times80\times30mm^3$ and a footprint of $300\times200\times220mm^3$ (Figure 2.4).

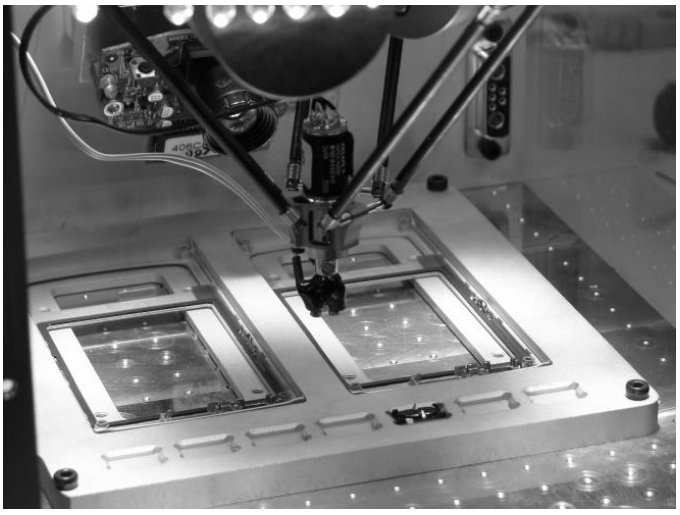

Figure 2.4 PocketDelta® robot from [28] used in [17]

Finally, [9] fabricated an assembly station using a commercial 4-DOF parallel SCARA manipulator. The assembly tasks are performed using both vision feedback and force sensing and vibration of the end-effector to stochastically align parts between 2.2mm and 6.3mm in size.

2.1.3 Hybrid Manipulators

Errors occurring during the assembly process can result from the actuators and drives, the control system, the sensors, the calibration or the manufacturing errors. One solution is to have very tight manufacturing tolerances and use very high precision manipulators, but this significantly increases the cost of the system. Alternatively, hybrid manipulation, also called multiscale manipulation, can be used. A coarse positioning system will pick a part and place it at a desired location. It has a low accuracy and compliance but allows for fast and large displacement for which accuracy is not critical. The position error is then compensated by a fine positioning system within a small workspace.

Some of the systems described in Sections 2.1.1 and 2.1.2 have added a fine positioning mechanism in their application. Most of the time, the fine positioning mechanisms consist in an MMS with 2 to 3 DOFs. For instance, the manipulators in [20] combine two 3-DOF MMSs assembled in series, the first one for coarse positioning and the second one for fine positioning. The coarse MMS is screw-driven and has a resolution of 0.05μm and a travel range of 15mm along each axis of motion, while the fine positioning system is PZT actuated and has a 100μm travel range and 1nm resolution. A similar configuration was used in [16], [18] and [30]. To continue, the SCARA robot designed in [26] is combined with a 3-DOF MMS (Figure 2.5). The system from [40] combines two MMSs. The coarse stage is a 4-DOF MMS driven by stick-slip PZT motors and has a travel range of 21mm. The fine stage is a 3-DOF MMS driven by PZT stack actuators with a travel range of 100μm. Alternatively, for larger scale manipulation, [5] used a Gantry manipulator for coarse pick-and-place operations and a conventional MMS for the fine positioning of the parts.

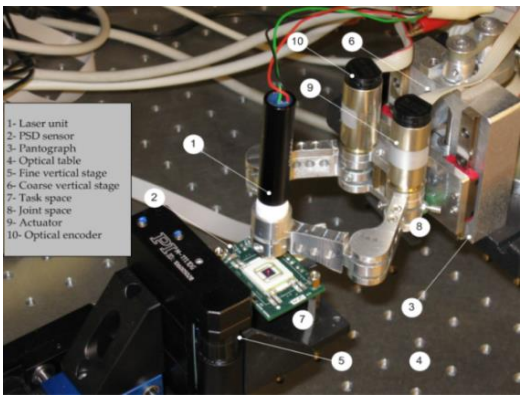

Figure 2.5 Hybrid manipulator from [26]

Hybrid manipulation can also be achieved through the vision system, by having a wide view camera and a narrow view camera or by using the camera only for fine positioning, as in [16, 20, 21, 44].

2.1.4 Grippers

Gripping is a critical part of an assembly system. The choice of gripper is based on the available energy (electric or pneumatic), the size and cost limitations, and the required degrees of mobility, but more importantly on the dimensions and the materials of the parts to manipulate. At macroscale, gravity is the dominant force and only the gripping force needs to be considered. At microscale, the gravity becomes insignificant when compared with other forces such as Van der Waals, Casimir attractive, capillary, electrostatic and magnetic forces detailed in [56-59]. With mesoscale, gripping parts with a size of around 1mm becomes challenging but this can be overcome by selecting an appropriate gripper.

Shape memory alloy grippers [60], PZT grippers [61-63], Ionic Polymer Metal Composite (IPMC) [64], electro-mechanical and electro-thermal grippers [13, 40, 65, 66] are mechanical passive grippers that deform when a current flows through the material. They are more common at smaller scale because the opening range of the jaws is usually very small. An electromagnetic gripper was used in [17] but it limits the range of parts material to metals. Other grippers used in micro-assembly such as pneumatic pipe tip, electrostatic needle or tips using fluid surface tension can be used. For instance, the gripper used in [11] uses capillary force, which uses the contact force of oil to pick and place parts (Figure 2.6). This gripper has the advantage to allow for a larger positioning error when picking parts like spheres, which will self-centre under the gripper tip once

picked. However, this would not be applicable to other types of geometries or to larger parts and could leave undesirable stains on parts such as lenses.

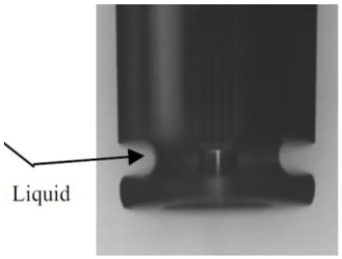

Figure 2.6 Capillary force gripper from [11]

A multitude of compliant grippers have been designed in the past few years [61, 64, 67-75]. This type of gripper is also more common for parts smaller than 1mm because the grasping range is usually very small. The advantage of compliant grippers is that force sensing can be integrated using, for example, strain gauges. The use of compliance in the end-effector also allows for a reduction of the positional accuracy requirement. For instance, [76] uses a compliant passive gripper to manipulate small parts. However, the parts designed need to be adapted to properly mate with the gripper. For parts larger than 1mm, vacuum grippers are mainly used as they are easy to include in the design (Figure 2.7), to operate and avoid damages caused by grasping force [8, 9, 23-27, 77, 78].

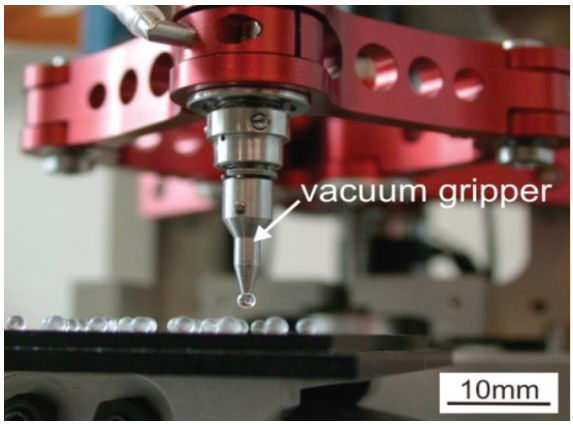

Figure 2.7 Vacuum gripper used on a miniature SCARA robot [79]

Although less common, conventional mechanical grippers can be used [5] but this solution is not suitable to achieve micrometre scale accuracy, it makes part assembly more complicated and increases the size of the end-effector (Figure 2.8). Another gripper using inflatable rubber tips was presented in [80]. Although this gripper is too large, reducing its size could make it suitable for smaller part manipulation.

Generally, flexibility such as interchangeability of grippers is important and is often integrated in the assembly systems [5, 7, 8, 13, 79, 81], allowing for different grasping range but also grasping method.

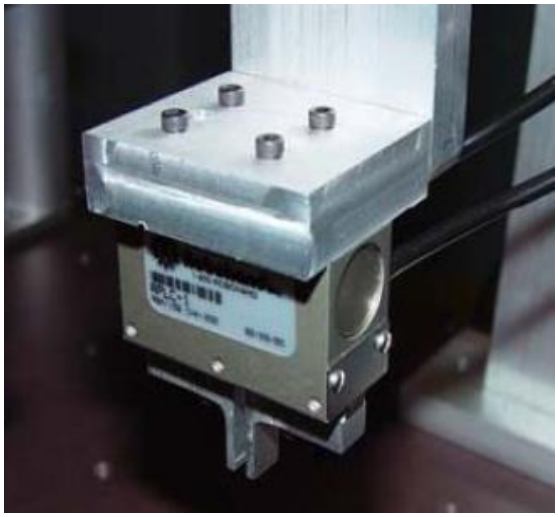

Figure 2.8 Conventional mechanical gripper from [5]

2.2 Compliant Mechanisms in Micro-Motion Systems

Compliant mechanisms are deformable structures that transmit an input force through flexible joints to obtain an output displacement. Due to their numerous advantages such as compactness, cost reduction and enhanced performances, they are a promising alternative to conventional rigid-body mechanisms. They have many applications in micro-electro-mechanical systems as micro-grippers, switching mechanisms, accelerometers, variable passive components, etc. [82]. Micro-motion systems such as micro-motion stages or micro-motion manipulators are systems that can achieve micrometre scale positioning accuracy, regardless of their workspace. The inclusion of compliant mechanisms in micro-motion systems has allowed for accuracy and repeatability values in the nanometre scale. However, because motion is obtained through the deformation of material, compliant mechanisms' design and analysis are more challenging than for rigid mechanisms. This section outlines the different compliant mechanisms developed over the past decade to perform micro-motion with high accuracy and repeatability. A short introduction to compliant mechanisms is presented, followed by an overview of existing mechanisms, design methodologies, analysis and modelling

techniques used. Finally, key elements and main challenges for future development are discussed.

2.2.1 Compliant Mechanisms

Conventional mechanisms are structural elements connected together with joints to enable a motion in a particular plane or axes. These mechanisms mainly use conventional joints, such as revolute, spherical and prismatic joints. Conventional joints allow for large displacements and are highly rigid but also have many disadvantages such as backlash, stick-slip effect, noise and slower response. In addition, they need regular lubrication and high precision manufacturing to reduce backlash. In miniaturised assembly, because of the high precision and tight tolerances required, conventional mechanisms are not always a viable and cost-effective solution. An alternative solution is to use compliant mechanisms to overcome the above stated issues and obtain highly accurate and repeatable motions. Most of the time, compliant mechanisms have a monolithic structure, giving them numerous advantages. They have no backlash, no friction, do not require lubrication, are easy to fabricate, operate under vacuum, are compact, lightweight and emit no noise. However, due to the fact that displacement is achieved by deflection of the joints, compliant mechanisms also have several disadvantages such as non-linear behaviour, high stress concentration, limited working area and off-axis deviation which induce errors if neglected. This implies more complex modelling, analysis and control, making the design of compliant mechanisms harder than for conventional mechanisms.

As with conventional mechanisms, compliant mechanisms with more than one DOF can either have a parallel configuration or a serial configuration. Parallel mechanisms have a high rigidity, high output force and high accuracy [83, 84]. Serial CMMSs often combine two 1-DOF compliant prismatic joints stacked on the top of each other, and have the advantage of being easier to design and fabricate, are naturally decoupled, making the control easier, but are less stiff and accumulate assembly tolerance errors. On the other hand, parallel mechanisms make the static and dynamic study more complex and are more difficult to control.

Compliant mechanisms have various applications. For instance, they can be integrated in MMS, which are used for bonding of optic components [85] and integrated circuits [86], for fibre alignment and semi-conductor positioning [87], for ultra-precision micromachining centre, optical alignment [88], wafer stage or scanner for Atomic Force

Microscope (AFM) [4, 89]. Alternatively, large displacement compliant joints are usually integrated into existing conventional robots for micro-manipulation tasks such as a basic 2-DOF robot based on five-bar mechanism [90], a Delta based robot [91, 92] or a 3-DOF CMMS [93, 94]. Compliant micro-grippers are used for micro-manipulation from micro-assembly tasks [95] to single-cell manipulation [65].

2.2.2 Common Types of joint

As with conventional mechanisms, different types of joints are used to obtain desired rotation and translation, defining the number of DOFs of the mechanism. Most of the basic compliant joints are flexure hinges. Flexure hinges are widely used, either to generate rotational motion or, when integrated in a parallelogram structure, to generate translational motion.

There are various types of flexure hinges. According to [89] and [96], the most common types of compliant flexure hinges are flat springs (also called leaf-springs as shown in Figure 2.9), and notch-type flexures (right angle, elliptic and circular flexure hinges as shown in Figure 2.10).

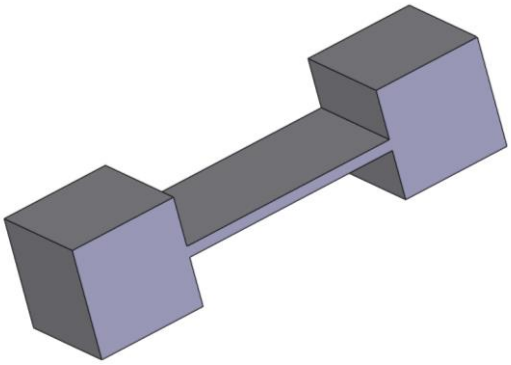

Figure 2.9 Typical leaf-spring flexure hinge

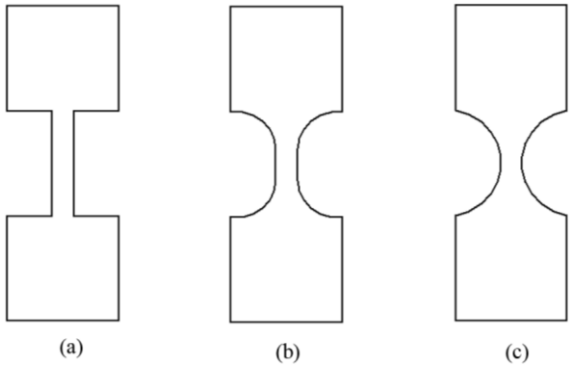

Figure 2.10 Typical notch-type flexure hinges, (a) Right angle, (b) Elliptic, (c) Circular

According to [97] and [98], compliant mechanisms can have lumped compliance (notch-type flexures), distributed compliance (leaf-spring flexures) and hybrid compliance. Notch-type flexures are subjected to higher stress concentration than flat spring flexures [93, 99]. From the study carried out in [100], circular flexure hinges have the greatest fatigue life amongst the other notch-type flexures. Furthermore, according to [101], circular flexure hinges have a greater accuracy than other flexure hinges, and [102] claims that using circular flexure hinges instead of leaf-spring beams increases the stiffness. Also, [99] and [90] argue that leaf-spring flexure hinges have a low torsional stiffness and can be subjected to buckling. However, [89] clearly confirmed that leaf-spring flexures could achieve the largest displacement range among other types of flexure hinges. In addition, [97] claims that distributing the deformation across several areas avoids high stress concentration and increases the fatigue life. A hybrid compliant-notch flexure parallelogram structure has been designed in [91] and used for a CMMS. This parallelogram structure combines a flat spring on one end of each beam and circular flexure on the other end. The circular flexures allows for higher stiffness and the flat springs reduces the stress concentration. A less common type of circular flexure hinge has been developed in [94]. Its structure avoids buckling and a deformation test shows that it can achieve a ±7° larger deflection than right-angle flexure hinge. However, the motion trajectory of this circular flexure hinge is not symmetric and the location of the rotation centre has to be carefully considered when integrating the flexure on a system. In addition to the most common types of flexure hinges, other types of flexure have been developed. For example [87] and [103] designed a novel flexure hinge with a thin shaft configuration, allowing for large deflection with high torsional stiffness. Unlike the common types of flexure, this one has been designed to be assembled to a limb or link. Therefore, it cannot be used for monolithic compliant structures. To obtain a larger rotation, more complex flexure pivots have been developed, such as cartwheel flexures, axial-strip flexures and cross-strip flexures. These are rotational flexures made of leaf-springs. According to [99] and [104], these compliant joints allow for more than 10° rotation angle. A list of flexures is presented in [105], giving a good overview of common types of large displacement flexures.

Conventional prismatic joints are composed of two parts sliding along each other. Because of the monolithic nature of compliant joints, translation can only be achieved by converting a rotational motion into a translational motion using the flexures listed in the previous paragraph. Most of the time, parallelogram structures based on a four-bar

mechanism are used. Four types of parallelogram structures exist [106]: basic parallelogram (Figure 2.11a)), compound basic parallelogram (Figure 2.11c)), double parallelogram (Figure 2.11b)) and compound double parallelogram (Figure 2.11d)).

A basic parallelogram (Figure 2.11a)) is a simple set of two parallel beams attached to the base on one end and to the moving plate on the other end. The major disadvantage of this structure is the cross-axis deflection due to the bending of the beams [96, 107].

A compound basic parallelogram (Figure 2.11c)) is a symmetrical arrangement of two basic parallelograms. This structure increases the stiffness thanks to the symmetric arrangement of the beams, cancels the cross-axis deflection and according to [108] avoids uneven thermal expansion. As explained in [102], if compound basic parallelograms were rigid bodies, translation would not be possible. Nevertheless, in compliant mechanisms, a very small elongation of the beams is tolerated. A small translation is therefore possible without cross-axis error as long as the elongation of the beam is much smaller than the length of the beam [96].

A double parallelogram (Figure 2.11b)) is a set of two parallel beams attached from the base to an intermediate moving plate which is attached to a second moving plate by another set of two parallel beams. This structure allows for a larger range of motion than the basic parallelogram structure but according to [102] and [109], it has a low stiffness due to the uncontrollable mass of the intermediate plate. According to [110], by only using beams which have the same length within a double parallelogram structure, the cross-axis deflections of the two moving plates compensate each other.

A compound double parallelogram (Figure 2.11d)) is a symmetrical arrangement of two double parallelograms. This structure allows for greater cross-axis stiffness than a double parallelogram structure but it also has a lower stiffness than the compound basic parallelogram structure.

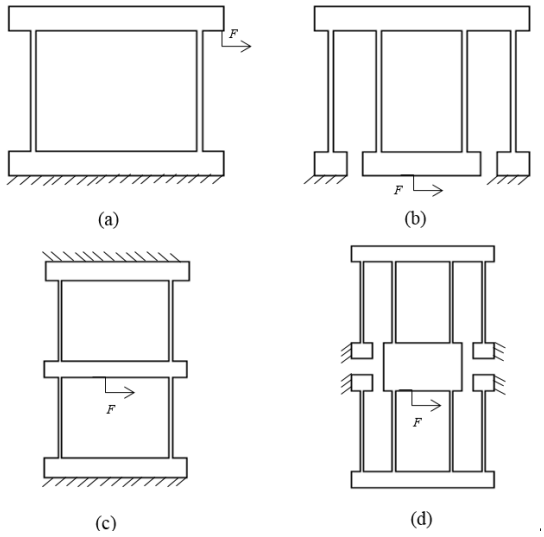

Figure 2.11 Common parallelogram structures. (a) Basic parallelogram. (b) Double parallelogram. (c) Compound basic parallelogram. (d) Compound double parallelogram

Although the basics of flexures hinges and parallelogram structures are well known, there are still some areas of improvement that must be further investigated. For instance, [97] demonstrated that by statically balancing a parallelogram structure, a larger range of motion could be achieved with near-zero force being needed to actuate the mechanism, as the positive stiffness would be compensated by preloading the mechanism. To continue, [99] demonstrated that increasing the number of beams in the parallelogram structure increases the stiffness ratio, which is the ratio between the off-axis stiffness and the axial stiffness. Another area of improvement is the integration of fatigue life in the design of flexure hinges. Significant research has been carried out on the mechanical behaviour of flexure hinges under static loading, but fatigue life has not been fully taken into consideration. Fatigue life has been integrated to the design of flexure hinges in [100] and [111], taking into account the stress concentration, surface finish, non-zero mean stresses at various loading conditions. However, very few papers evoke the fatigue life analysis of compliant mechanisms. Finally, the evolution of accuracy over time under different loading conditions is not taken into consideration. [91] stated that temperature change in flexure hinges (caused by a high strain rate or by the environmental conditions) could have an effect on accuracy but this effect has not been investigated yet.

2.2.3 Compliant Joints Integrated to Conventional Parallel Robots

Large displacement compliant joints can be integrated on existing robots to achieve micrometre positioning accuracy within macro workspace. The main challenge is to

design compliant joints that are highly elastic in the desired direction and highly rigid in other directions.

A few robot platforms have recently been developed, offering sub-micrometre accuracy in a workspace varying from $2\times2\times2mm^3$ to $4\times4\times4mm^3$ [94, 112, 113]. A larger workspace is obtained using larger displacement flexure hinges integrated on conventional spatial robots. Such flexures have been developed in [85] and [114] and are made of flat springs layered in series that can achieve ±24.58° deflection and can be combined in parallel to obtain compliant universal joints (Figure 2.12). These flexures have then been integrated on a 3-DOF robot with a Delta-based architecture. The robot has a workspace of $50\times50\times5mm^3$ with sub-micron repeatability. Another rotational flexure was developed in [115] using steel ropes.

Figure 2.12 End effector of a DELTA robot with large displacement flexure hinge from [85]

Similarly, [91] and [92] developed a universal joint based on a combination of notch-type flexure hinges and can achieve a ±20° rotation. The joint was also implemented on a Delta type robot which can cover a $200\times200\times60mm^3$ volume with a 0.3µm repeatability and a 0.125µm resolution. The use of compliant joints with parallel kinematic mechanisms (PKMs) for micro-assembly and micro-manipulation is proven to be efficient. For instance, the repeatability achieved in [116] for the same system was 3 to 4 time greater with compliant joints than with conventional joints. To continue, [99] and [93] proposed a range of large displacement compliant joints to be implemented within PKMs. The joint designed in [90] had a ±45° rotational range and was implemented on a 5-bar parallel robot with a repeatability in a range of 50µm to 84µm within a $200\times100mm^2$ workspace. However, a large drift of the rotation axis was observed during experimental studies and the stiffness still needed to be improved. A

range of large displacement compliant joints was proposed in [99] and [93] to be implemented within PKMs.

2.2.4 Compliant Micro-Motion Stages

The most common application of compliant mechanisms is micro-motion stages. Most of the high precision MMS are compliant mechanisms combining high precision actuators and sensors and prismatic flexure joints. This section gives an overview of some of the CMMSs developed in the last decade.

When designing a CMMS, a few parameters have to be taken into consideration to obtain good performances. First of all, the system's structural frequency and bandwidth must be kept high to improve the system's response time [117]. Moreover, the ratio between off-axis stiffness and axial stiffness must be as high as possible [118], and cross-axis deflection must be kept as low as possible [99]. In this context, the main challenge is to achieve large workspace and full decoupling, meaning decoupling of the actuators (input) and the moving platform (output). In addition, [110] affirms that coupled motion may induce stress stiffening phenomena and input coupling could damage the actuators. However, [36] claims that combining both force and displacement decoupling is hard to achieve and generates complexity. A trade-off must therefore be made when designing a CMMS.

A CMMS with decoupled axes (output decoupling) using a novel parallel kinematic mechanism was designed in [119]. The CMMS can achieve a 50nm accuracy, a $87\times87\mu m^2$ workspace and has a resonant frequency of 563Hz along the X-axis and 536Hz along the Y-axis. Although very high accuracy is achieved, the high stiffness causes the workspace to be very small. Another CMMS with complete decoupling was developed in [102]. This CMMS is only composed of circular flexure hinges based on compound basic parallelograms. The experimental results show that the CMMS has a first natural frequency of 720.52Hz, less than 5% coupling and a potential $105\times105\mu m^2$ displacement range. The first natural frequency is kept high because basic compound parallelograms are used. However, the workspace remains very small. The CMMS fabricated in [4] shows that increasing the width of the beams increases the stiffness of the CMMS but reduces the working range, while increasing the length of the beams will increase the working range. The working range of the CMMS is $150\times150\mu m^2$ and the first resonant frequency is 377Hz. A fully decoupled CMMS was designed in [36] and

[120], where input decoupling is achieved using electromagnetic actuators (Figure 2.13). The CMMS can achieve sub-micron accuracy and a $1\times1mm^2$ working range and the first three resonant frequencies are 134.5Hz, 176Hz and 444.6Hz. The CMMSs presented in this paragraph show that a clear connection exists between the resonant frequencies and the range of motion. To facilitate the input decoupling and to increase the range of motion of PZT driven CMMSs, amplification mechanisms are often integrated [4, 110, 118, 121-123]. The mechanisms are usually inspired from a conventional lever mechanism as in [124] and [125].

As mentioned previously, it is important to cancel any parasitic rotation and increase the off-axis stiffness. A decoupled CMMS composed of compound basic parallelograms was developed in [109]. The compound basic parallelograms are rigidly fixed two by two with connecting bars, improving the load distribution and the stiffness. This structure results in highly constrained parasitic rotation and no cross-axis motion. A similar CMMS was designed in [98] to cancel any parasitic rotation and the translation along the Z-axis by integrating a spatial three double-beam mechanism. To continue, [126] designed a CMMS with a working range of 5×5 mm^2 and a coupling error of less than 0.8%. The outside parallelograms are also connected together with rigid bars to reduce the coupling between the axes. A more complex CMMS with parasitic translation compensation was proposed in [127], with a first natural frequency of 100Hz and a theoretical workspace of $10\times10mm^2$. The CMMS from [128] achieves full decoupling by using only double compound parallelogram structures. Although the workspace is $10\times10mm^2$, the first resonant frequency is only 18Hz.

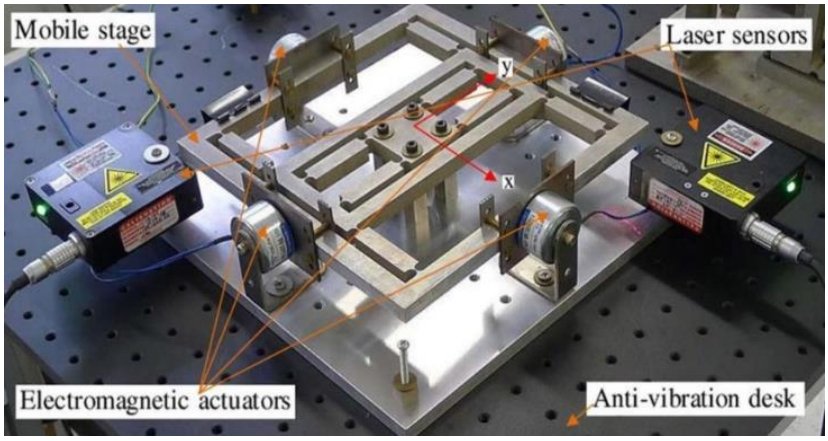

Figure 2.13 MMS driven by electromagnetic actuators from [120]

Larger displacement is achieved in [89], where the 1-DOF CMMS designed can achieve more than 11mm stroke. This CMMS has a multitude of double compound parallelogram structures serially connected, thus increasing the working range but reducing the first natural frequency to 60Hz. Based on the same structure, [129] designed a CMMS which has a 10.5×10.5mm^2 workspace, has resonant frequencies of 48.3Hz, 48.7Hz and 100.Hz along the X, Y and Z directions respectively and less than 1.6% coupling (Figure 2.14). The CMMS designed in [130] implements the Roberts mechanism to achieve a workspace of 14×14mm^2, a coupling of 0.08% and resonant frequencies of 32.3Hz, 32.5Hz and 58.7Hz. Another CMMS designed in [131] can achieve a workspace of 20×20mm^2 with a coupling of less than 1.56%. It is important to note that a large workspace often implies a large footprint, which is not desirable in a confined environment where compactness is a key issue. The out-of-plane stiffness is increased by incorporating spatial compliant joints, making it 7.1 times stiffer along the Z-axis than without this mechanism. Finally, the CMMS fabricated in [132] has a reachable workspace of 20×20mm^2, a coupling of 1.3% and the first three resonant frequencies are 60Hz, 60.5Hz and 128.5Hz.

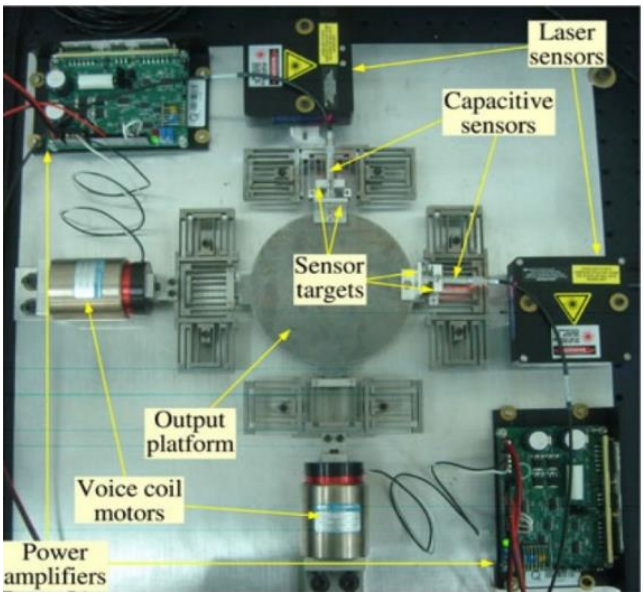

Figure 2.14 MMS driven by VCAs from [129]

2.2.5 Material and Fabrication of Compliant Mechanisms

Most of the prototype of CMMSs with a monolithic structure fabricated in the literature used the wire electric discharge machining (WEDM) process. WEDM is a

material removal technique that uses electric sparks to erode the material with high precision [133]. This technique is used to machine components as small as 100µm [134]. Because material with high yield strength and yield strength to Young's modulus ratio is desirable [135], Aluminium Alloy 7075 is widely used for CMMS [4, 36, 89, 101, 102]. Alternatively, a 3D printed prototype was fabricated in [109] with ABS Plus3. Other materials such as stainless steel [119], spring steel [85, 94] and beryllium-copper [87, 103, 136] are used, mainly for large deflection compliant joints rather than CMMS. Shape Memory Alloy [91, 92] can achieve large deflection with low deviation due to its super-elastic properties and its large reversible strain which can be up to 17%. This material also has a longer fatigue life than spring steel. The flexure hinges from [137] are made of medium carbon steel (S45C).

2.2.6 Modelling and Analysis of Compliant XY Stages

2.2.6.1 Force-displacement relationship

There are various ways to derive the stiffness of a CMMS. A commonly used method is the Pseudo-Rigid Body Model (PRBM). This method, first introduced by Howell and Midha in 1994 [138], allows flexible elements to be modelled as rigid bodies connected together by torsional springs (Figure 2.15). This method was used to produce accurate results for small deflections [89, 107, 139, 140] but becomes inefficient when the deflection is in a range of a few millimetres with for example errors as large as 12.8% reported in [130]. One limitation of this method is that it often considers the compliance of the flexure joints in the direction of rotation but considers the beams as rigid bodies. Nevertheless, the PRBM is constantly being developed and improved to accurately model large deflections, as explained in [141]. Some recent models include the compression of the beams. For instance, the model derived in [140] takes into account the compression of the beams to estimate the motion loss. Based on this method, the nonlinear term induced by tension loading has been addressed to improve the model accuracy for large displacements. An extended PRBM was used in [142-144] to model compliant joints using linear springs instead of rigid links to connect the torsion springs together. The PRBM was used in [145] to analyse a fixed-guided beam.

Another method commonly used is the compliance matrix method based on Hooke's law and consists of replacing each joint by an equivalent spring model (Figure 2.16). This

method has been reported to be accurate and efficient for small displacements [36, 108, 110, 131, 146-155] and is often used as it allows for a full analysis of deformation of all links. Simplification of the compliance matrix is usually achieved by reducing the number of DOFs of the flexures from 6 to 3 in the analysis. This method is efficient but has limitations when larger displacements are applied with reported errors of 7.4% in [98], 8.5% in [108], 10% in [36], 17.7% in [155] and 20% in [110].

Basic derivations based on elastic theory are limited to mechanisms with a simple structure, but is probably the simplest method and is sufficient in many cases [129, 156-160]. However, as for the compliant matrix method, this method is only efficient for small displacements. This has been documented in [129] and [156], where the displacement error reaches 30.9% and 9% respectively when compared to FEA.

Alternatively, [106, 109, 161-163] derived a nonlinear force-displacement relationship based on equations established in [164] for beam-based mechanisms using a Beam Constraint Model (BCM). The model is based on a free-body diagram (Figure 2.17) and takes into account the load stiffening phenomena with very large axial forces for a motion range of up to 10% of the beam's length. This model is regarded as an efficient analytical method but the introduction of tension in the beams could be simplified.

Using elliptic integrals to model large deflection of beams is considered the most accurate technique [165, 166]. However, this method is one of the most time-consuming and complex methods.

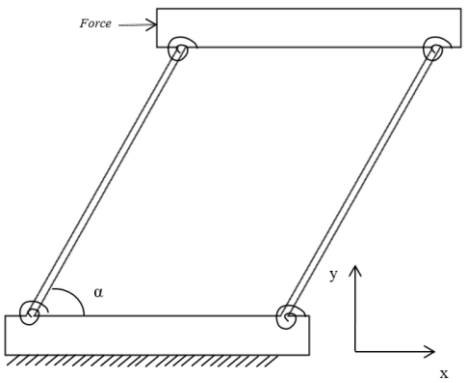

Figure 2.15 PRBM of a basic parallelogram

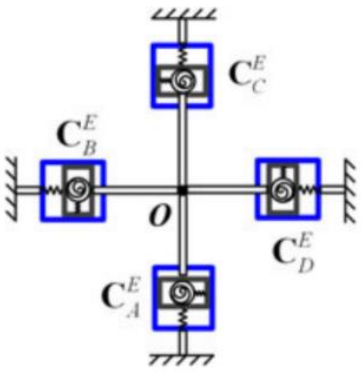

Figure 2.16 Spring equivalent model for the stiffness matrix from [108]

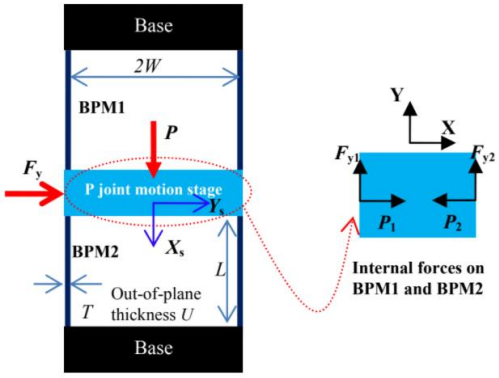

Figure 2.17 BCM from [109]

2.2.6.2 Dynamic analysis

The dynamic analysis of compliant mechanisms is an important step to analytically derive the system's resonant frequencies. The two major ways of obtaining the dynamic model of a system are Newton-Euler equations and Lagrange equation, the first one being based on force/torque balance and the second one being based on energy balance. The energy based method is found to be widely used for compliant mechanisms because it is simpler than other methods [102]. Alternatively, Kane's method, taking advantage of both above cited methods, has been used in [103] and [167] to derived the dynamic model.

2.2.6.3 Topology Optimisation

Topology optimisation is a mathematical procedure that involves defining the best geometric configuration in order to achieve a desired goal. It is often used to design new compliant structures but also to optimise existing ones. Most of the time, the goal is to obtain large displacement with reasonable stress distribution. According to a majority of

the literature, the design parameters of compliant mechanisms are the thickness and width of the flexures and the length of the beams.

There are various ways of designing through topology optimisation. A common way is to use optimisation algorithms such as Genetic Algorithms (GAs) [89, 120] or Particle Swarm Optimisation (PSO) algorithms [102, 110]. From these references, it has been concluded that PSO is the most efficient method to perform topology optimisation and is easier to implement than GAs but it requires very long computation time. Alternatively, the design from [4] was optimised by plotting the theoretical evolution of the natural frequency, the workspace and the output force of the mechanism as a function of the design parameters. Another interesting approach that is usually not fully investigated is to include fatigue life in the design of flexure hinges to define the geometrical parameters [100].

2.3 Dual-Range Motion Stages

Commercially available MMSs from manufacturers like H2W Technologies Inc., PI (Physik Intrumente) Ltd, ALIO Industries and Moticont offer a range of motion starting from less than 100μm up to several centimetres and a positioning accuracy from around 10μm down to a few nanometres. However, systems with a centimetre range workspace either have a low accuracy or are relatively expensive. The concept of dual-range manipulation is to use two sets of actuators and/or sensors within the same system to achieve higher accuracy within the same workspace, or increase the workspace without reducing accuracy. The first set allows for positioning in a large workspace but has a low positioning accuracy. The second set covers a smaller workspace, just enough to compensate the positioning error of the coarse mechanism and has a high positioning accuracy. The main advantage of dual-range manipulation is the cost reduction. It also avoids the need for complex calibration, tight manufacturing and assembly tolerances.

Most conventional dual-range MMSs simply consist of two stages serially connected, simplifying their design and assembly. Some MMSs can achieve a very high absolute positioning accuracy over a large range of motion by using ultra-high resolution/large range sensors such as laser interferometers. However, this implies a high cost and often a large footprint. For instance, the MMS designed in [137] consists of a PZT actuated MMS mounted on the top of a DC motor driven MMS, resulting in a $300\times300mm^2$ workspace and a positioning accuracy of ±10nm. However, the system is quite large and very

expensive because of the hardware used. A 3-DOF MMS was designed in [168] using linear motors for the coarse positioning and Voice-Coil Actuators (VCAs) for the fine positioning. The system has a workspace of $500\times500mm^2$ and can achieve nanometre scale accuracy with a repeatability of 50nm. However, the system is also large and expensive. The MMS developed in [169] combines a 2-DOF coarse positioning stage driven by linear motors and a 6-DOF fine positioning stage driven by VCAs and magnetic bearings (Figure 2.18). The coarse positioning stage has a $300\times300mm^2$ workspace and the position is measured using linear encoders. The fine positioning stage has a $1\times1\times1mm^3$ workspace and the position and orientation are measured using three laser interferometers and three capacitive sensors. The final accuracy achieved along the X- and Y-axes are 10nm and 15nm respectively. The system has a footprint of $1440\times1145\times1120mm^3$. The 3-DOF MMS from [170] combines two linear motors and four PZT actuators, giving it a working range of $200\times200mm^2$ and an accuracy of 13nm. The MMS designed in [171] also combines VCAs and PZT actuators. It can achieve an accuracy of ±20nm within a workspace of $25\times25mm^2$. The coarse stage is driven by VCAs and the fine stage is driven by PZT actuators. The same configuration was used in [86], achieving the same workspace with a 10nm motion resolution. [172] developed an MMS driven by linear motors using guiding rails and a similar decoupling mechanism. With the linear encoders used, the accuracy is 0.6μm for a workspace of $\pm25\times25mm^2$. A 1-DOF MMS was developed in [173] using a linear motor for the coarse motion and a VCA for the fine motion. The positioning accuracy achieved is 10nm within the working range of 300mm. Another hybrid 1-DOF MMS was developed in [173] using a linear motor and a VCA stacked on top of each other and uses a laser interferometer for absolute positioning. The workspace is 300mm for a positioning accuracy of 10nm. Finally, a 1-DOF MMS was developed in [174]. The coarse positioning is obtained by a linear motor and a linear encoder and the fine positioning is obtained by a Lorentz motor and a laser interferometer allowing for absolute positioning.

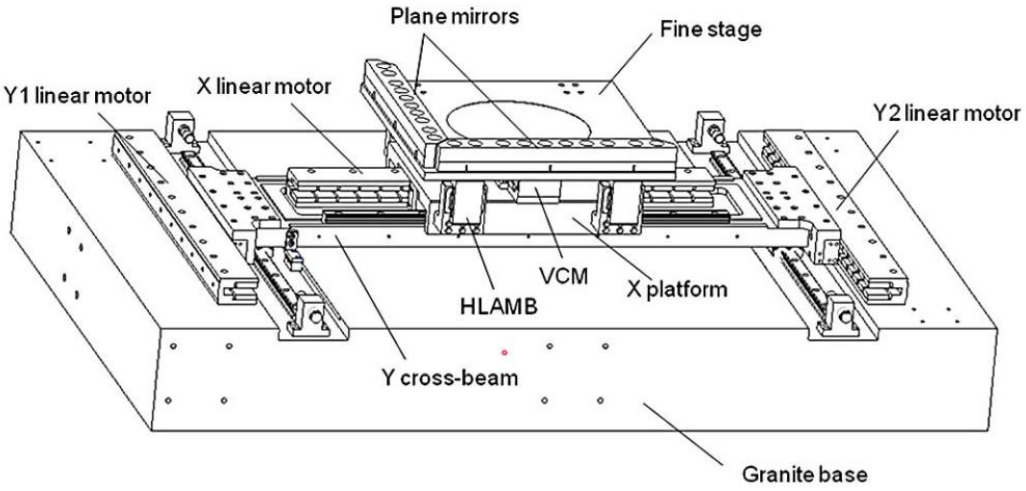

Figure 2.18 Dual-range MMS from [169]

The accuracy, workspace and therefore cost of these MMSs are not justified for miniaturised product assembly applications. In addition, stacking two MMSs on top of each other increases the moving mass and therefore slows the dynamic response. Alternatively, other dual-range motion MMSs use high resolution/short range sensors such as capacitive sensors for the fine positioning. This solution involves cheaper equipment but allows for the same positioning accuracy. However, the positioning is only relative to the current coarse position of the MMS. For instance, the 2-DOF MMS developed in [175] consists of a PZT actuated MMS mounted on top of a DC motor and a lead screw driven MMS. It can reach a sub-micrometre accuracy using capacitive sensors and has a workspace of $200\times100mm^2$. The 1-DOF MMS designed in [176] uses a VCA for the coarse positioning and a PZT actuator for the fine positioning (Figure 2.19). The high-resolution linear encoder used allows for a positioning accuracy of 20nm within a workspace of 80mm. The positioning error is below one micrometre with a tracking error of 2µm. A controller was designed to cope with coupling issues. The 1-DOF MMS developed in [177] uses only pneumatic actuators. A 100mm stroke air cylinder and a linear encoder is used for the coarse positioning. Pneumatic bellows and a second linear encoder are used for the fine positioning which has a 500µm stroke. The relative positioning accuracy achieved is 20nm. Finally, the 1-DOF MMS designed in [178] uses a VCA for the coarse positioning and a PZT actuator for the fine positioning. The working range is only 300µm and only a capacitive sensor is used for feedback. The accuracy is 10nm.

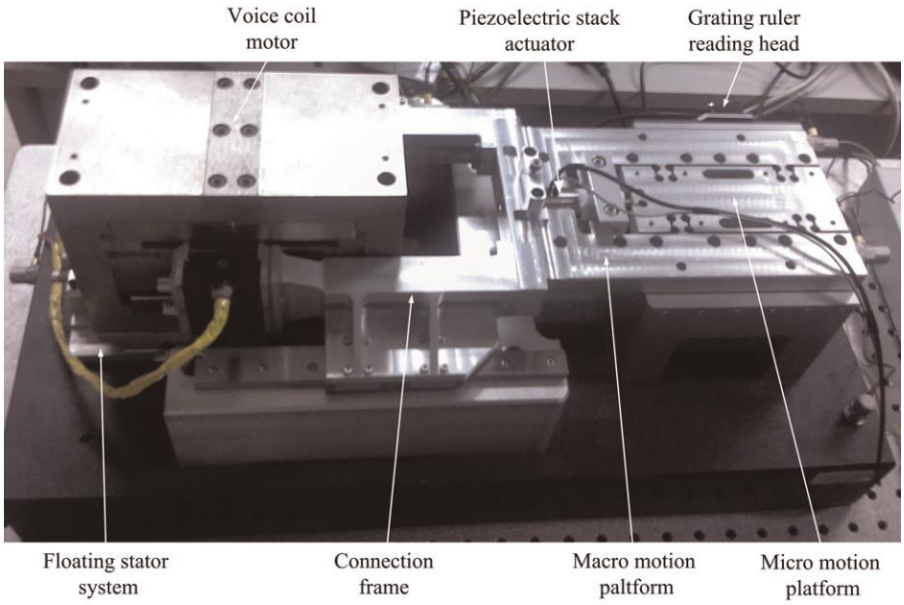

Figure 2.19 Dual-range MMS from [176]

The serial configuration of the MMSs presented in the previous paragraph can create interactions between the coarse and the fine actuator, making the system difficult to control. In some cases, the dual-range manipulation is carried out using a single CMMS in which two sets of actuators and/or sensors are integrated. For instance, a fully decoupled dual-range MMS was designed in [108]. For each direction of motion, one PZT actuator is coupled to the MMS with a lever mechanism to amplify the motion by a 4.2 ratio, thus resulting in a coarse motion and one other PZT actuator is directly coupled to the MMS, thus achieving fine motion. The MMS has an accuracy of 0.01μm but its workspace is only $119.7\times121.4\mu m^2$. Another MMS designed in [128] can reach a positioning accuracy of 4nm within a workspace of $10\times10mm^2$ by using linear encoders to measure the actuator's displacement and capacitive sensors to measure the change in distance between the moving platform and the intermediary MMS. This concept is very useful to compensate for the lost motion error but it ignores the potential coupling between the two axes of motion. It would therefore only be suitable for fully decoupled MMSs. The 1-DOF MMS developed in [179] consists of a PZT actuator directly mounted on a VCA with a positioning accuracy in the nanometre scale. The MMS designed in [156] uses only two VCAs and two sets of strain gauges, one for the coarse positioning and one for the fine positioning (Figure 2.20). The resolution of the coarse motion is 8.52μm for a range of -1.94mm to 2.47mm, while it is 1.63μm for the fine motion in the range of -0.22mm to 0.31mm. The advantage of this solution is that once the MMS has

been calibrated, both coarse and fine positioning are absolute. However, the fine positioning mode cannot be used for the whole workspace.

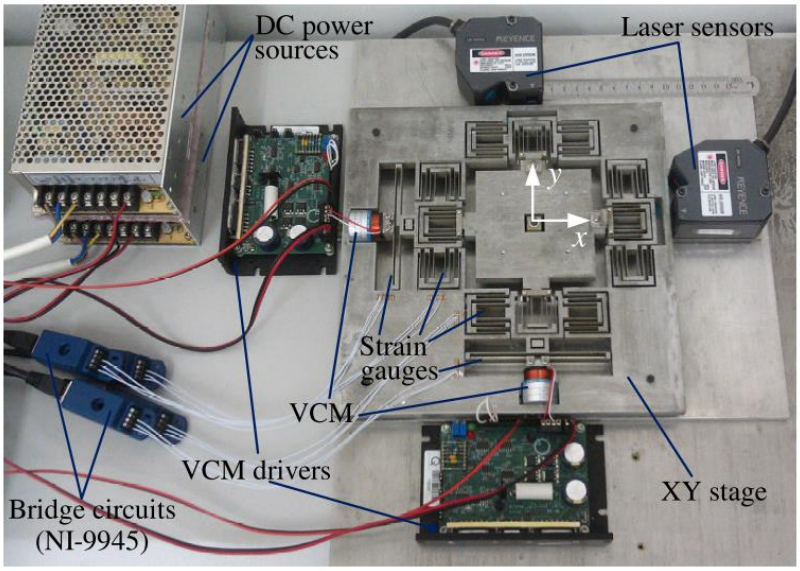

Figure 2.20 Dual-range MMS from [156]

2.4 Actuation and Sensing for Micro-Motion

As discussed earlier in this chapter, micro-positioning systems require a large range of motion, a high stiffness and a high positioning accuracy. Although selecting an appropriate mechanical structure, such as a compliant mechanism, can avoid backlash and reduce the effect of manufacturing and assembly errors, the positioning accuracy heavily relies on the selected actuators and sensors.

2.4.1 Actuators

From the reviewed literature, it is clearly outlined that PZT stack actuators are a first choice for micro-motion [4, 86, 119, 136, 139, 180]. For miniaturised assembly, they are less common and mainly used for some of the fine positioning mechanisms, as in [20], and are often off-the-shelf components from specialised manufacturers. For example, Physics Instruments (PI) and SmarAct supply a wide range of highly accurate linear PZT actuators and PZT actuated MMSs (i.e. Nanocube®) but the prices are high.

The magnetic linear actuators used in [11] allow for frictionless smooth and accurate linear motion. Miniature DC motors can now also offer high accuracy which can often be

sufficient for several applications, as in [23]. Linear motion guided by air bearings offers very smooth and frictionless translation [47] .

Actuators with a larger stroke but reduced accuracy are usually used for the coarse motion mechanism such as DC motors [118] or ultrasonic PZT motors [87, 103, 136]. Alternatively, [36, 155, 181] use electromagnetic actuators because of its non-contact characteristic of actuating force, thus achieving input decoupling of the MMS. For systems where compactness is not the main issue as in [86, 89, 128, 130, 132], VCAs present many advantages such as long stroke, no backlash and can be controlled by force, position or velocity.

Linear motors [182] can also be used to achieve a larger motion range as in [183] This is commonly used as the coarse positioning mechanism of large dual-range MMSs and is often combined with air bearings to obtain a smooth frictionless and accurate motion. However, these motors are costly.

2.4.2 Sensors

Whether they are used for closed-loop control of the system or to determine the accuracy and repeatability of the system, position sensors are essential. Laser sensors are mainly used [85, 89, 94, 102, 119, 120, 129, 132, 155]. They are capable of sub-nanometre resolution and can be placed at a longer distance from the target. Capacitive sensors are also frequently used [4, 40, 91, 101, 129] because they have a higher resolution and are cheaper than laser sensors, but they must be placed very close to the target and have a limited sensing range, usually below 1mm. Linear encoders are commonly used for conventional MMSs but are not optimal for CMMSs because they are not easy to integrate to the structure and the read head must remain close to the graduated scale. However, some recent work carried out in [184] shows a potential suitability of linear encoders for MMSs. Linear Variable Differential Transformers (LVDTs) are rarely used for micro-motion because their reading accuracy is not as good as for interferometers or capacitive sensors [185]. However, they are one of the most cost effective solutions and unlike linear encoders, they allow for cross-axis displacement. 3-axis accelerometers have been used by [136] and [181] as inertial sensors but are more suitable for spatial motion than laser sensors.

Because the position of the moving platform of a MMS is directly related to the input force of the CMMS, which is known, force sensors are rarely used. Moreover, due to the

compactness of the mechanisms, integrating force sensors within the mechanical structure is difficult. In the work from [186], strain gauges were symmetrically arranged on the elastic beams to measure its deflection and derive the force. According to [187], such a configuration is difficult to obtain because the gluing process can cause some misalignment and the amount of glue used for each sensor may vary. An alternative solution was proposed in [60, 159, 188], which consists of measuring the deflection of a cantilever beam.

2.5 Summary

An overview of existing micro-assembly and desktop-size assembly systems was presented, including hybrid manipulators and gripping techniques. The systems' characteristics and performance in terms of accuracy and workspace were evaluated and will be used for comparison with the system developed in this thesis. The cost of these micro-assembly systems is usually high, mainly because of the commercially available MMSs used and the vision systems.

A full description of compliant mechanisms was then given and existing compliant MMSs were reviewed. To continue, existing dual-range MMSs, which often integrate a CMMS, were critically evaluated. To conclude, the actuation and sensing methods used to achieve micro-motion in the covered literature were listed. Commonly used design, modelling and analysis technics were also investigated. It was clearly shown that compliant mechanisms are a viable solution for micro-motion and micromanipulation with many advantages allowing achieving high accuracy and repeatability. The available literature shows that compliant mechanisms are widely studied, well known and constantly evolving. However, many challenges have arisen from the review work. From the numerous critical system characteristics needed to be taken into account to the complexity induced by non-linear behaviours, these mechanisms need to be improved in order to achieve highly accurate and decoupled motions within a larger workspace while keeping the system's natural frequencies and stiffness ratio as high as possible. The concept of dual-range positioning shows a great potential in our effort to reduce the cost while maintaining a high positioning accuracy.

From this literature review, it is hoped that a dual-range MMS will be designed to be the fine motion mechanism of an affordable desktop size hybrid manipulator with a large workspace, a high positioning accuracy and a large manipulation capability.

Chapter 3 Linear Modelling and Characterisation of a Compliant Micro-Motion XY Stage

The wide range of recently developed CMMSs presented in Section 2.2.4 offers a multitude of design options, such as the type of structure, the modelling technique and the material and fabrication method. The advantages arising from these CMMSs could be considered as a disadvantage when different design constraints are applied. In this chapter, a CMMS with a simple structure is presented. The aim is to obtain a low-cost CMMS with a working range of a few millimetres. It is also desirable to have a high stiffness ratio between the axes of motion and the other directions, and minimal cross-coupling between the two axes of motion. A linear stiffness model is firstly derived using two different techniques, the Pseudo-Rigid Body Model (PRBM) and the well-known Euler-Bernoulli model. These models are then compared with FEA. The effect of the beams' dimensional parameters on the CMMS's characteristics are evaluated using FEA. Finally, two prototypes are fabricated and tested. The purpose of the first prototype is to study the feasibility of the design. The second prototype is used to investigate the use of polymer for CMMSs.

3.1 Linear Modelling of a Compliant XY Stage

The CMMS is designed with only basic compound parallelogram structures to be as simple as possible, therefore reducing the machining cost. Such a structure is compact and allows the resonant frequencies to be higher than with double parallelograms, but limits the working range. The CAD model of the designed CMMS is shown in Figure 3.1. The CMMS is designed to be actuated from two sides by linear actuators. As only basic compound parallelograms are used for the CMMS and the lengths of the beams are all equal, each leaf-spring flexure can be considered as a spring with a stiffness K linking the CMMS to the base. The springs are considered as being in a parallel configuration. Hence, the overall stiffness of the CMMS along one direction is twelve times the single beam stiffness K. This configuration allows the derivation of the theoretical force-displacement relationship using a single beam deflection model. For comparison, the force-displacement relationship of the CMMS will be determined using the PRBM and Euler-Bernoulli beam deflection theory.

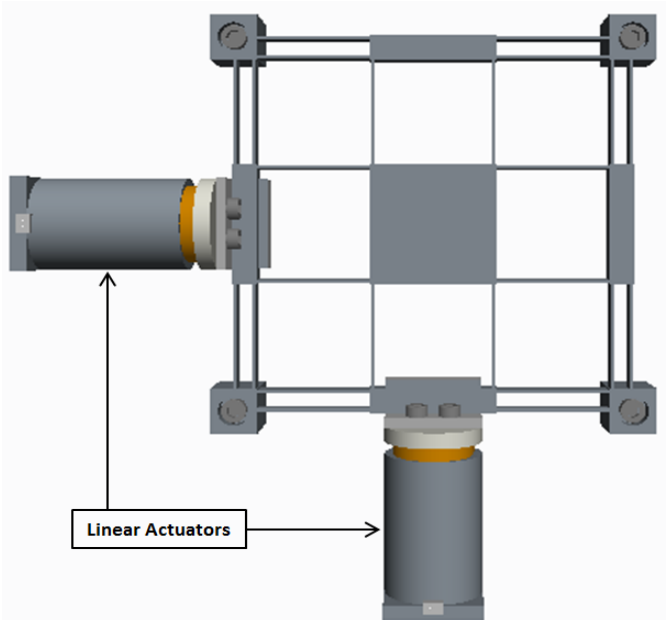

Figure 3.1 Conceptual design of the first CMMS

3.1.1 Pseudo-Rigid Body Model

The characterisation of the CMMS begins with the stiffness. Firstly, the PRBM is used to derive the linear stiffness of a single beam. Based on the work from [189], a fixed-guided beam is represented as three rigid links connected with torsional springs. The PRBM representation of a single beam is presented in Figure 3.2. The displacement of the end point of the beam is given by:

$$\delta = \gamma l \sin \varphi \tag{3.1}$$

where l is the total length of the beam, γ is the characteristic radius factor from [189] and φ is the angle between the rigid link and the origin. From Euler-Bernoulli beam deflection theory, the slope and moment at the midpoint of a fixed-guided beam is zero. The torque is therefore derived from the input force and beam's length at this midpoint:

$$T_T = \frac{\gamma l}{2} F_A \cos \varphi = K_T \varphi \tag{3.2}$$

where T_T is the torque applied at one of the pivots centre point, K_T is the torsional spring stiffness of this pivot and F_A is the external force applied at the end of the beam. The torsional spring stiffness is given by:

$$K_T = 2\gamma K_\varphi \frac{EI}{l} \tag{3.3}$$

where K_φ is the pseudo-rigid-body stiffness coefficient, E is the Young's modulus of the material and I is the second moment of area of the beam given by $I = bh^3/12$ where b

is the width of the beam and h is the thickness of the beam. As the force is applied vertically, γ = 0.8517 and K_φ = 2.67617 [189].

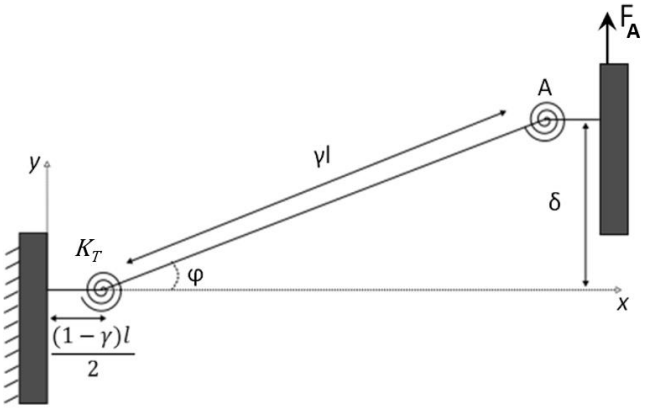

Figure 3.2 Pseudo-Rigid Body Model of a single beam

Assuming the angle φ is very small, the following approximation can be made:

$$\begin{cases} \sin\varphi \approx \varphi \\ \cos\varphi \approx 1 \end{cases} \tag{3.4}$$

Rearranging Eqs. (3.1) to (3.4), the relationship between force and displacement is therefore:

$$F_A = \frac{4K_\varphi EI\delta}{\gamma l^3} \tag{3.5}$$

3.1.2 Euler-Bernoulli Model

The Euler-Bernoulli beam bending theory is then used to derive the linear stiffness of a single beam. The only purpose of using two linear models is to evaluate their efficiency to model large beam deflections. The Euler-Bernoulli representation of a beam is presented in Figure 3.3.

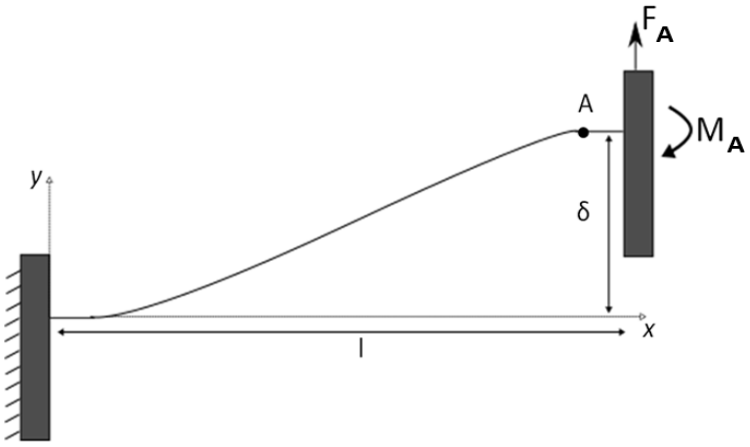

Figure 3.3 Euler-Bernoulli beam deflection model of a single beam

As the displacement at the end of the beam δ is assumed to be very small, the curvature of the beam is also assumed to be small, and can be described as [190]:

$$\frac{1}{\rho} = \frac{d^2y}{dx^2} = \frac{M}{EI} \tag{3.6}$$

where ρ is the radius of curvature of the beam; M is the moment applied to the beam; and d^2y/dx^2 is the curvature of the beam. For a fixed-guided beam, the expression of the bending moment M applied to the beam is:

$$EIy''(x) = M = F_A(l - x) - M_A \tag{3.7}$$

where F_A and M_A are the force and the moment respectively applied at point A. From Eqs. (3.6) and (3.7), the slope at any point x on the beam is:

$$EIy'(x) = \int M.dx = (F_A l - M_A)x - \frac{F_A}{2}x^2 + C_1 \tag{3.8}$$

The boundary conditions dictate that at $x = 0$, $y'(x) = 0$. Hence, the constant $C_1 = 0$. For $x = l$, the following relationship is determined:

$$\frac{F_A l^2}{2EI} - \frac{M_A l}{EI} = 0 \tag{3.9}$$

Therefore the force F_A can be expressed as a function of the moment M_A:

$$F_A = \frac{2M_A}{l} \tag{3.10}$$

The deflection at any point x on the beam is:

$$EIy(x) = \iint M.dx = \frac{(F_A l - M_A)x^2}{2} - \frac{F_A x^3}{3} + C_2 \tag{3.11}$$

Given the boundary condition, $C_2 = 0$. Substituting Eq. (3.10) into Eq. (3.11) the maximum deflection of the beam at $x = l$ can be expressed as:

$$\delta = \frac{F_A l^3}{12EI} \tag{3.12}$$

3.1.3 Travel Range Limitations

The second step of the characterisation of the CMMS is the working range. Most of the existing work on CMMSs only uses the yield strength as a travel range limitation. This is acceptable for short and thick beams as the force required to cause buckling is often much higher than the force required to reach a stress equal to the material yield strength. However, for longer and thinner beams, buckling can occur before the yield strength is reached and cannot be ignored. Therefore, the buckling point of the beams is integrated in the working range of the CMMS.

From [191], the critical point of a beam fixed at both ends is given by:

$$F_{crit} = \frac{4\pi^2 EI_z}{l^2} \tag{3.13}$$

Buckling should occur at one of the inner beams parallel to the loading direction and where the reaction force is the highest. Since there are only sets of two beams, it is assumed that the buckling force $F_{buckling}$ is twice F_{crit}. When a force $F_{applied}$ is applied at the bottom of the CMMS (Figure 3.4), the reaction force $F_{buckling}$ acting on the set of beams is obtained by subtracting the reaction force of the four beams constituting the bottom parallelogram structure from the reaction force of the whole CMMS along the same direction. Thus, the buckling force $F_{buckling}$ is approximately $2/3$ of the force applied at the bottom of the XY CMMS $F_{applied}$. The input force required to cause buckling is therefore given by:

$$F_{applied} = \frac{12\pi^2 EI}{l^2} \tag{3.14}$$

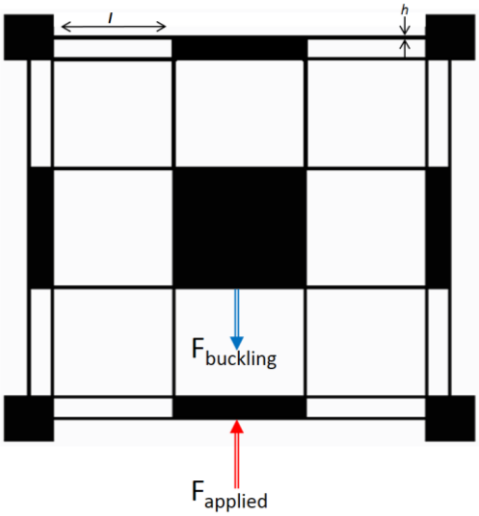

Figure 3.4 Buckling force diagram

The second travel range limitation is the yield strength of the material. A stress analysis is therefore included in the characterisation. The relationship between the maximum stress, occurring at the end of the beams on the cross-section's farthest edge from the neutral axis, and the maximum displacement is given by:

$$\delta_{max} = \frac{\sigma_{max} l^2}{3Eh} \tag{3.15}$$

where δ_{max} corresponds to the deflection of the beam when the maximum stress σ_{max} has been reached, h corresponds to the thickness of the beam and l corresponds to the length of the beam.

3.1.4 Evaluation of the Linear Model Using FEA

Nonlinear FEA is carried out using ABAQUS for comparison with the two analytical models and to further study the behaviour of the CMMS under large displacements. The dimensions of the beams are shown in Figure 3.5 and are chosen to be 35mm long (L), 6mm high (b) and 1mm thick (h). The impact of the length and width on the stiffness and travel range will be evaluated.

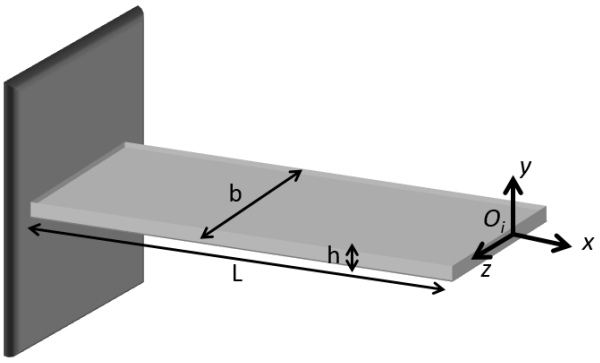

Figure 3.5 Beam dimensional parameters

The static analysis consists of applying a load on the CMMS to study the displacement and stress engendered. The material used for the analysis is Aluminium 7075-T6 because it is widely used in the literature [4, 36, 89, 102]. It has a Young's modulus (E) of 71.7GPa; a Poisson's ratio (v) of 0.33; a density (ρ) of 2810kg/m^3; and yield strength ($\sigma_{\max}$) of 505MPa. The material is described as hyperelastic and the model is based on the Neo-Hookean solid model. Force-displacement, buckling, stress kinematic coupling and modal analyses are further deliberated in the following sections.

3.1.4.1 Force-Displacement Analysis

To study the force-displacement relationship, a force of 700N is gradually applied and the displacement along the direction of motion is recorded. The results are then compared with the PRBM and Euler-Bernoulli analytical models in Figure 3.6a) and Figure 3.6b). It has been determined that in the range of 0 to 70N, the displacement error varies from 8.8% to -1.1% for the PRBM model and from 4.5% to -5.9% for the Euler-Bernoulli model, but increases significantly after 70N. These results clearly show that although some linear behaviour can be observed in the range of 0 to 0.55mm, as in [96], the linear models produce similar results but are not suitable for large displacements. This nonlinear

behaviour is attributed to the parallelogram structure which causes a load stiffening phenomena, resulting in a constantly increasing stiffness of the beams.

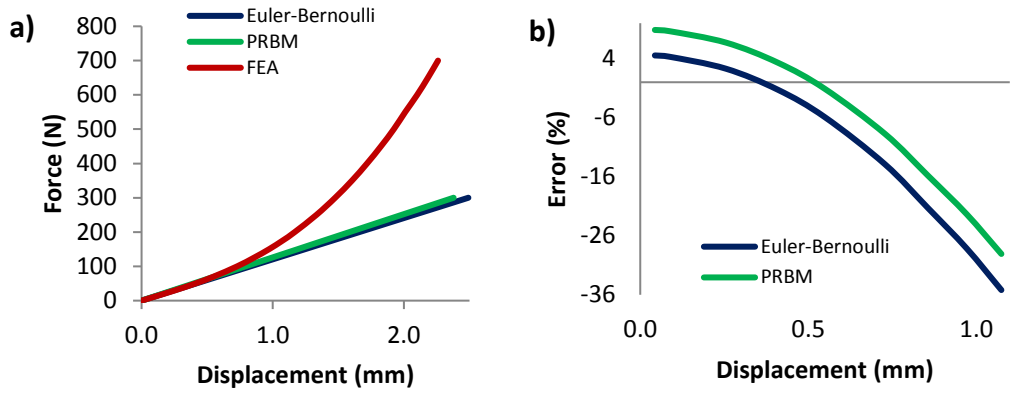

Figure 3.6 a) FEA of the force-displacement relationship compared with the analytical models, b) Error from comparison with analytical models

The length and width of the beams are varied to evaluate how these parameters affect the stiffness of the CMMS. From Figure 3.7a) and Figure 3.7b), it can be seen that the stiffness of the CMMS increases as the beam's length becomes smaller or as the beam's width becomes larger. These parameters will be taken into account for design optimisation of the prototypes.

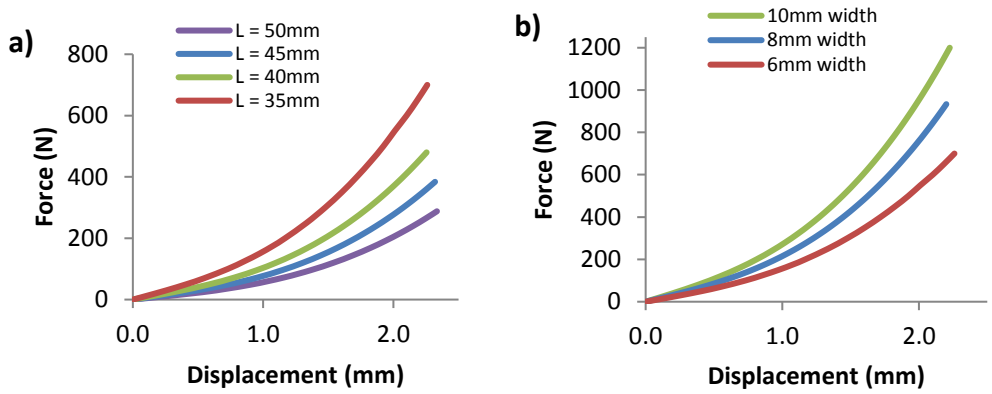

Figure 3.7 a) FEA with variable beam's length, b) FEA with variable beam's width.

3.1.4.2 Linear Buckling Analysis

A linear buckling analysis is then carried out. The results show buckling occurring with an input force of 3426N (Figure 3.8). The input force obtained using Eq. (3.14) is 3466N, corresponding to an error of 1.2%. This demonstrates that the linear buckling point can be accurately predicted in a linear analysis when compared with FEA. However,

the linear models are suitable for very a small deflection while buckling generally occurs under large forces and therefore displacements. Therefore, a linear buckling analysis may not be appropriate for the designed CMMS.

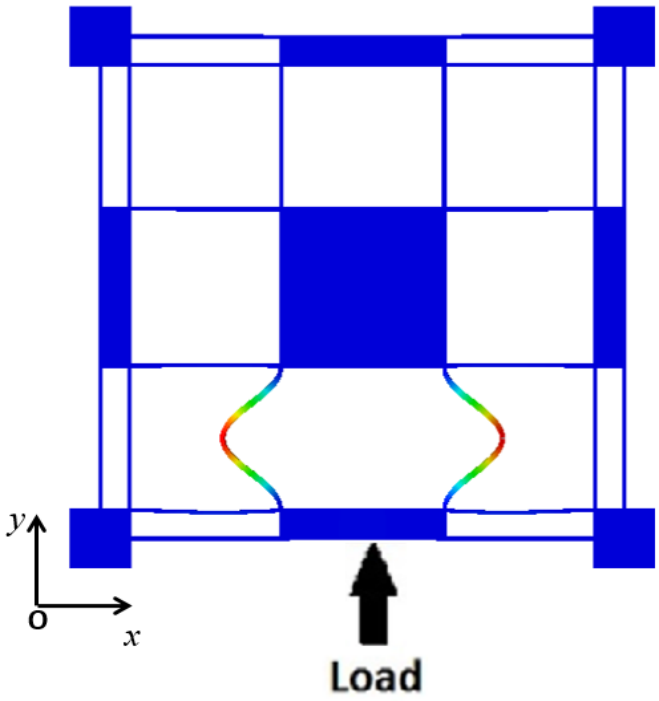

Figure 3.8 Buckling point when a load is applied along Y

3.1.4.3 Stress Analysis

A stress analysis is used to define the maximum allowable displacement which is limited by the yield strength of the material. The results of the stress analysis from the Euler-Bernoulli model and the nonlinear FEA model are shown in Figure 3.9a). As for the force-displacement analysis, it is clearly shown that the analytical linear model deviates from the nonlinear FEA model. The Euler-Bernoulli and FEA models indicate a maximum allowable displacement of 2.865mm and 1.975mm respectively, which corresponds to an error of 45%. This is due to the linear model in which tension loading is ignored. Observing Figure 3.9b) and Figure 3.9c), it can be seen that increasing the beam's length will increase the range of motion but the beam's width has almost no influence.

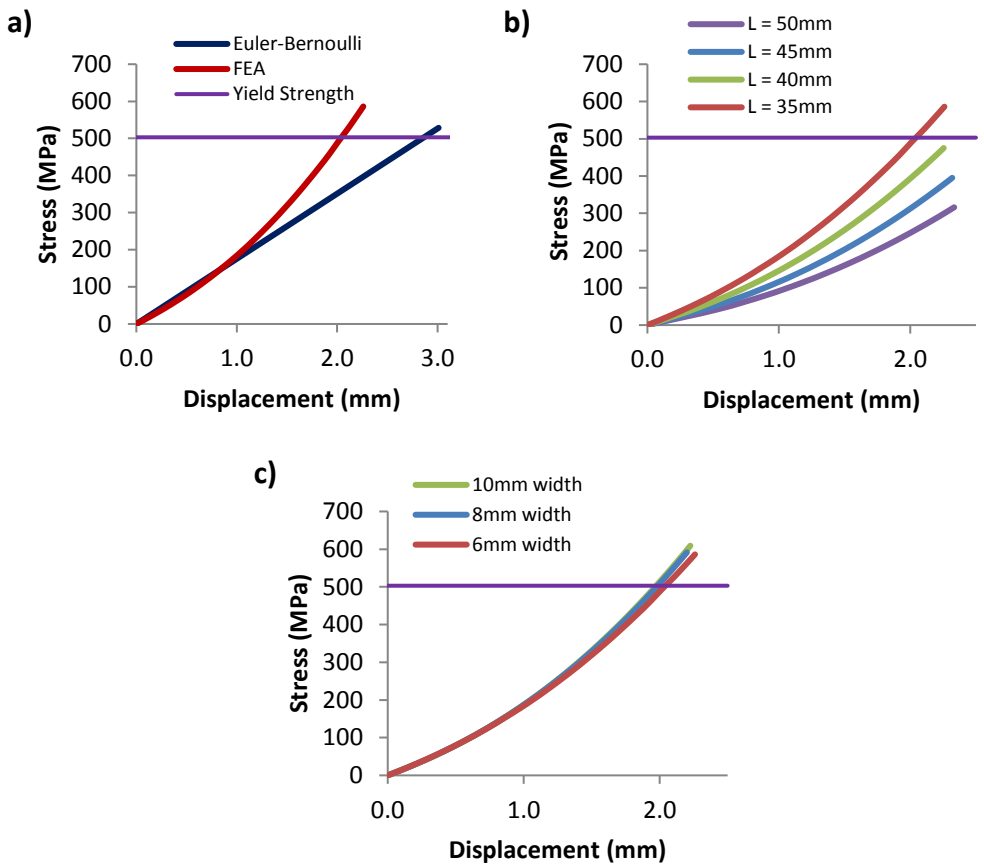

Figure 3.9 Stress analysis of the CMMS a) in comparison with analytical models b) with variable beam's length, c) with variable beam's width.

3.1.4.4 Kinematic coupling

As the CMMS is designed to have a low kinematic coupling, a coupling analysis is carried out by first applying a preload force of 500N along the Y direction, as presented in Figure 3.10, corresponding to the theoretical maximum displacement calculated in the previous section, and gradually applying a force from 0N to 500N along the X direction. From Figure 3.11a), the X-displacement error with preloading is 11.5% at 50N and reduces to 2.44% at 500N. This error is mainly due to the increase in stiffness because the applied preload is very large. When a preload of only 70N is applied, this error is lower than 1.9%. From Figure 3.11b), the cross-axis coupling, which means the parasitic displacement along the Y direction for every unit displacement along the X direction, is 0.28% at 50N and goes up to 2.36% at 500N, corresponding to a maximum coupling error of 44.8µm.

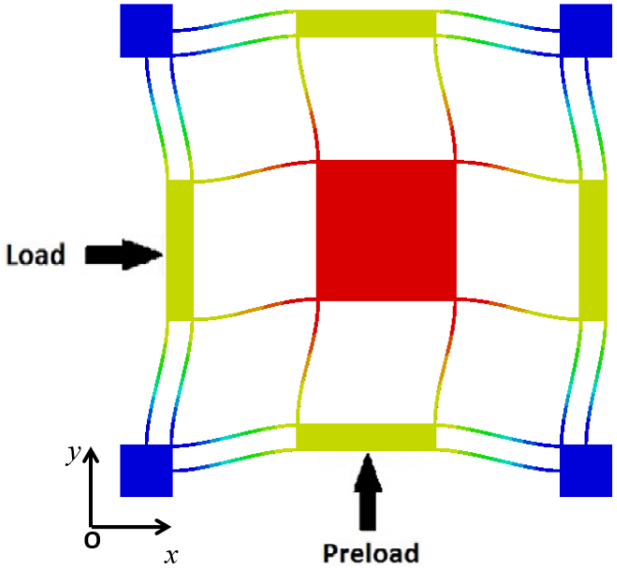

Figure 3.10 Deformed CMMS with input displacement applied along X and Y directions

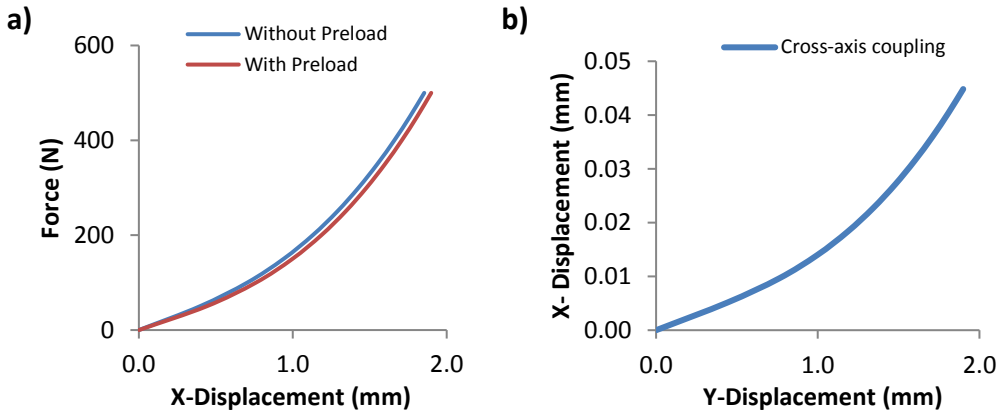

Figure 3.11 a) Y-Displacement with and without preload, b) Cross-axis coupling.

3.1.4.5 Modal Analysis

An analysis of the frequency response of the CMMS is carried out with ABAQUS using the Lanczos Eigen solver. The first two modes, corresponding to translational vibrations along the X and the Y directions respectively, occur at 262.7Hz and the third mode, corresponding to translational vibrations along the Z direction, has a frequency of 600.4Hz. This corresponds to a stiffness ratio of 1/2.3 between the X/Y-axes and the Z-axis. The frequency response of the CMMS is also evaluated as a function of the geometrical parameters. The results from Figure 3.12 show that the width of the beam

only has an impact on the frequency response along the Z direction while the length of the beam clearly modifies the stiffness along all the directions.

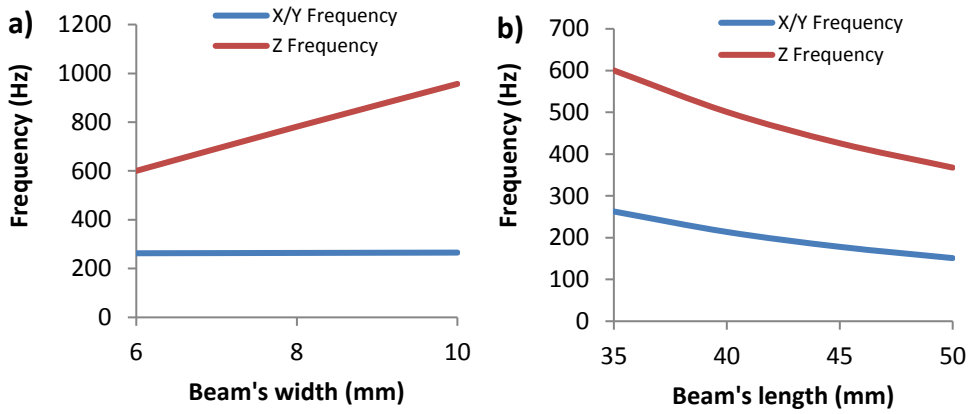

Figure 3.12 Frequency response of the CMMS for different a) beam's widths, b) beam's lengths.

3.2 Characterisation of a PLA Compliant Stage

As in [109], a 3D printed prototype made with Polylactic Acid (PLA) is fabricated. Although the material properties of 3D-printed polymers have many uncertainties [192, 193], this is the simplest, fastest and cheapest way to fabricate a prototype and study the force-displacement relationship and frequency response of the CMMS. The PLA used is the MakerBot PLA 1.75mm filament in true red. The prototype is fabricated with a Replicator® 2 from MakerBot which has a positioning precision o 0.011mm. The stage is printed with a 100% filling, a layer thickness of 0.1mm and the layers have a 0°/90° orientation. The beams of the fabricated CMMS have a length of 26.25mm, a width of 4.5mm and a thickness of 0.9mm. The density of the material once printed is 1150kg/m^3.

3.2.1 Frequency Response Analysis

In order to obtain the frequency response of the CMMS, a testing rig is set up with a shaker (LDS-V201) to generate guided vibrations along the X direction of motion and measure the amplitude with an accelerometer (ICP-T356A16) placed at the centre of the CMMS. A second accelerometer will be added later to characterise the coupling between the centre and edges of the CMMS. The sensitivity of the accelerometers is 100mV/G and their output signals are processed by a Dual Channel Accelerometer Amplifier (FE-376-IPF) and acquired by a Data Acquisition card (USB-6008) from National Instruments.

Labview is used to obtain the frequency domain response using the Fast Fourier Transform (FFT). The sampling rate is 10kHz.The testing rig setup with two accelerometers is presented in Figure 3.13.

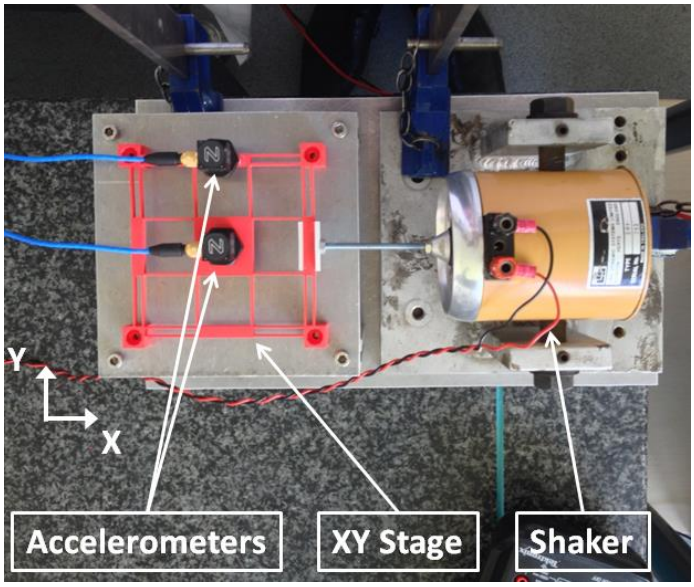

Figure 3.13 Vibration testing setup

Results from the literature [25, 26] show that the Young's modulus of PLA falls between 1.28GPa and 3.5GPa. The response of the CMMS is therefore modelled with FEA using both Young's moduli. For simplification, the material is considered as a linear elastic, isotropic material with hyperelastic properties. A mass of 17g is added at the centre of the model to emulate the mass of the accelerometer and the screw used for the frequency response test.

3.2.1.1 Test 1: single accelerometer

The results from the test with a single accelerometer placed at the centre of the CMMS are presented in Figure 3.14a). A peak in amplitude is observed when the vibrations generated by the shaker reach 75Hz. This peak is more obvious on the Y-axis as it represents free vibrations, while vibrations along the X-axis are guided by the shaker.

The FEA model indicates the first natural frequency occurs between 52.67Hz and 85.5Hz, when modelled with a Young's modulus of 1.28GPa and 3.5GPa respectively. Hence, the FEA model is in good agreement with the data acquired from the testing rig.

3.2.1.2 Test 2: dual accelerometer

The results from the test with two accelerometers are presented in Figure 3.14b). The peak in amplitude occurs at 70Hz. It is postulated that the 5Hz shift in occurrence of the peak amplitude is due to the addition of a second accelerometer. The output of the first and the second accelerometers are X1/Y1 and X2/Y2 respectively. The amplitude of X1 is in agreement with the value of X measured in Test 1.The large difference between X1 and X2 clearly shows that the CMMS has partial vibration isolation because, unless the resonant frequency has been reached, vibration from the shaker neither causes vibration along the Y direction nor on the edge of the CMMS.

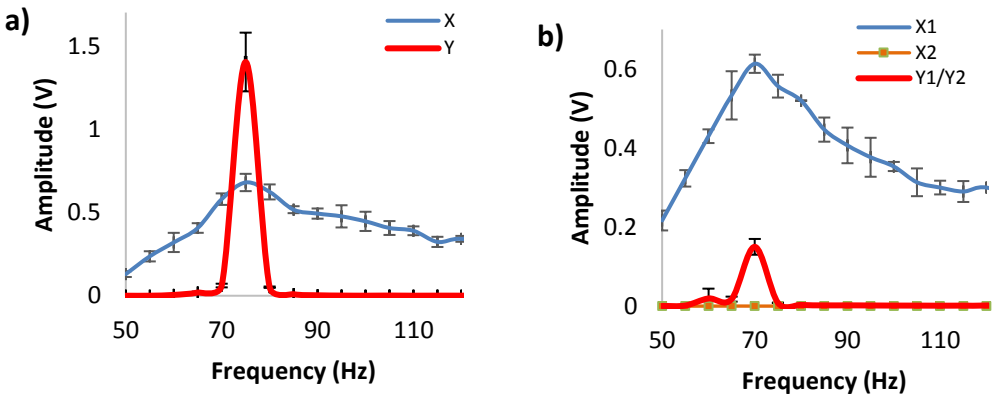

Figure 3.14 Frequency response of the 3-D printed CMMS with a) One accelerometer, b) Two accelerometers

3.2.2 Force-Displacement Test

The force-displacement relationship is studied by applying a load along one direction and measuring the displacement with a dial gauge of 0.0254mm resolution, as presented in Figure 3.15a). From Figure 3.15b), the experimental results show that the load stiffening phenomena is not obvious, which may be due to plastic behaviour of the material. Characterising 3D Printed PLA is proven here to be a complex task due to 3D printing attributes such as the orientation of the printed fibres, the layer thickness, density and effective Young's modulus of the material once 3D-printed. In addition, the study of a single beam will give different results than the study of the full structure because of the change in the fibre orientation results in anisotropy.

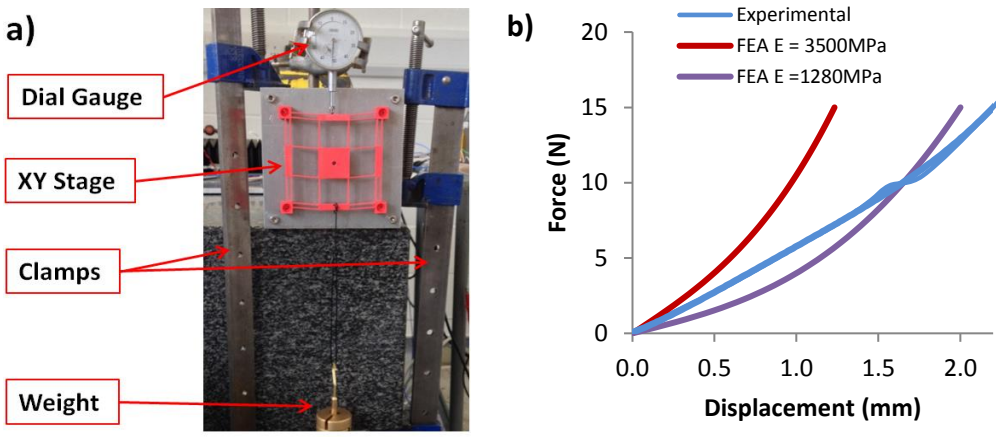

Figure 3.15 a) Loading Test Rig, b) Experimental results compared to FEA results of the 3d-printed CMMS loading test.

3.3 Characterisation of a Nylon-66 Compliant Stage

The structure of the compliant CMMS presented in this section is based upon the CMMS designed in Section 3.2 but the dimensions of the beams are chosen to be 45mm in length to increase the range of motion, 8 mm in height to maintain a high stiffness along Z and 1mm in thickness to ease the manufacturing process and to avoid buckling. The dimensions of the Nylon-66 CMMS are shown in Figure 3.16.

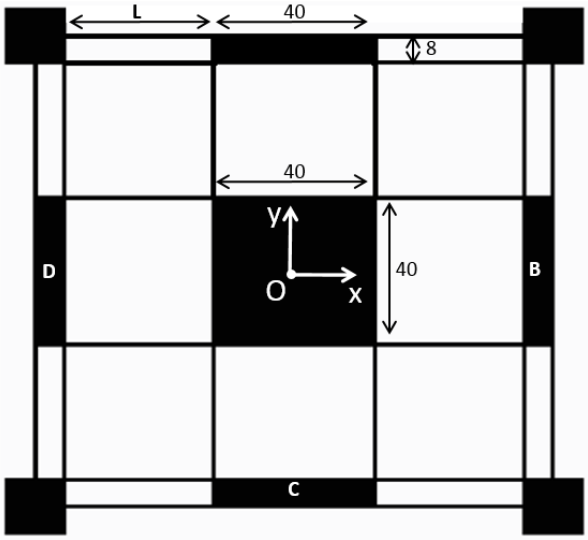

Figure 3.16 Dimensions of the Nylon-66 CMMS

Most of the CMMSs reported in the literature are made of Aluminium 7075-T6 because the mechanical properties of this material allow for a high reversible strain compared to other metals. In order to lower the input force requirement and investigate

the use of polymer rather than metal, the material selected for the final design is Nylon-66. This study will focus on the steady-state rather than the transient behaviour of the CMMS. Therefore, to simplify the analysis, the viscous properties of the materials are ignored and the CMMS is modelled as a linear elastic material with hyperplastic properties, using the parameters listed in Table 3.1.

Parameters	E (MPa)	σ_{max} (MPa)	P (kg/m^3)	ν
Values	3300	85	1150	0.4

Table 3.1 Initial geometrical parameters for the Nylon CMMS

Most of the CMMSs reported in the literature are fabricated using WEDM. The CMMS presented here is fabricated using abrasive jet machining. Unlike WEDM, this technique does not allow for tight tolerances and smooth surface finish. However, it is much cheaper and faster. Laser cutting and CNC machining are also considered but these processes are not suitable to cut 1mm thick beams. The first one would melt the beams and the second one would bend the beams because of the cutting force applied. The CMMS is fabricated by Strathclyde University in Glasgow, UK, and is presented in Figure 3.17.

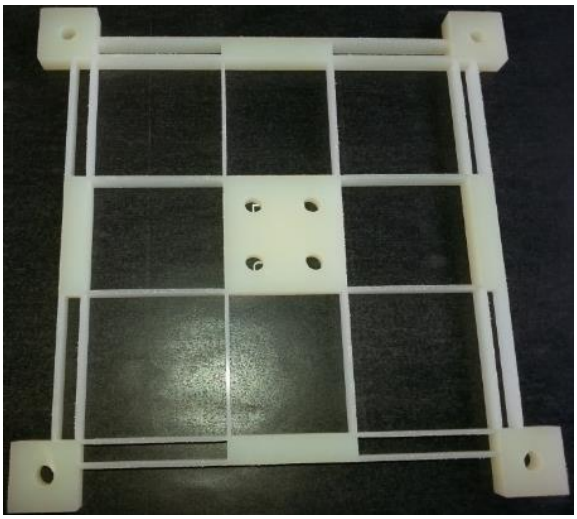

Figure 3.17 Fabricated Nylon-66 CMMS

3.3.1 Travel Range Limitation

Because the linear models are inaccurate for large displacements, FEA is carried out using ABAQUS in order to size the actuators and define the travel range of the CMMS. A nonlinear buckling analysis is first carried out. The buckling point is estimated from

the FEA results by analysing the output data for a large displacement. Buckling is occurring when the stress at the centre of the inner beams increases suddenly and the difference between the input and the output displacement of the CMMS increases significantly, as shown in Figure 3.18. For this stage, buckling occurs at the inner beams when an input force of approximately 173N is applied in the positive direction, corresponding to an input displacement of approximately 5.25mm.

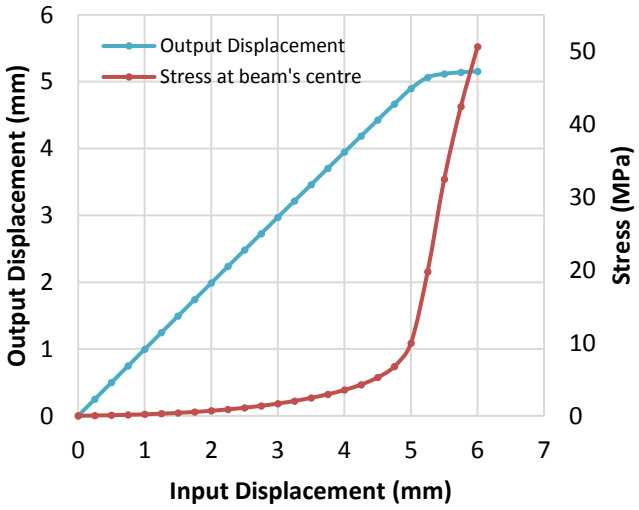

Figure 3.18 Stress and output displacement response to a large input displacement

A stress/strain analysis is then carried out. An input displacement is gradually applied on one side of the CMMS until the reaction force is equal to the critical point force obtained from the buckling analysis. The output displacement, the maximum stress and the reaction force are recorded. The input displacement of 5.25mm corresponds to a maximum stress of 69MPa. The yield strength of Nylon 66 (85MPa) is therefore not a limit to the travel range of the CMMS. To ensure a long fatigue life and reduce the actuation force, the travel range of the final design is limited to ±3mm. This corresponds to an input force of approximately 43.64N.

3.3.2 Motion Loss analysis

Because of the material used and the length of the beams, the axial deformation of the inner parallelogram beams causes the output displacement to be slightly different from the input displacement. The output displacement is therefore compared with the input displacement using FEA. Figure 3.19 shows the output displacement error at the centre of the CMMS when a load is applied from the side of the CMMS. The analysis is carried

out for positive loading, when the inner beams parallel to the direction of motion are in pure compression, and for negative loading, when these beams are in pure tension. The results show that for an input displacement between -3mm and 3mm, the output displacement error can reach 28µm when the beams are in compression. This error can therefore not be neglected.

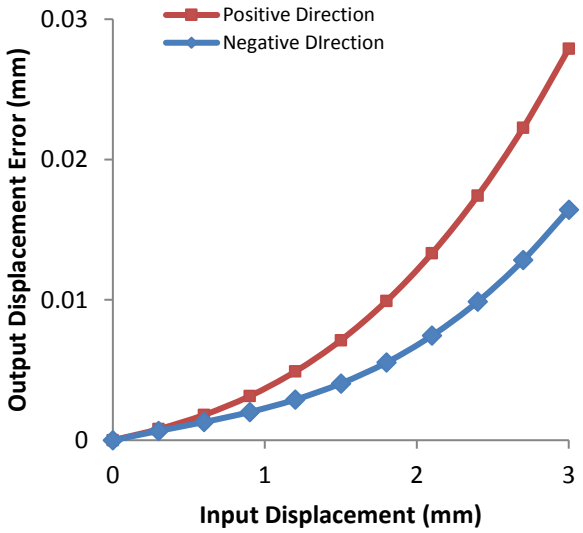

Figure 3.19 Output displacement error for single direction loading

3.3.3 Force-Displacement Analysis

The force-displacement relationship is estimated on the fabricated CMMS and compared with FEA. A load is applied along one direction and the displacement is measured with a dial gauge of 0.0254mm resolution, as it was done in Section 3.2 for the PLA CMMS. The material used has a water absorption coefficient of 2.8% and as the CMMS is submerged in water during its fabrication, it is assumed that the material properties are modified as a result of water absorption. Figure 3.20 shows the result of a series of three tests. First, the CMMS is tested immediately after fabrication (Test 1). Then, the CMMS is tested after being placed in a desiccator for one week at 10mbar pressure to remove all the moisture (Test 2). Finally, the CMMS is tested after three weeks of use at standard indoor temperature and humidity (Test 3).

The results of Test 1 show a large difference when compared with the theoretical results, with approximately 46% force error at 2mm. Test 2 clearly shows that removing the moisture increases the stiffness of the CMMS, with the error being reduced to 28%. Furthermore, the mass of the CMMS is reduced from 53.5g to 50.28g, showing the efficiency of the desiccating process. However, Test 3 shows that after a few weeks of

standard conditions use, the stiffness is drastically reduced, with a force error of 67% at 2mm.

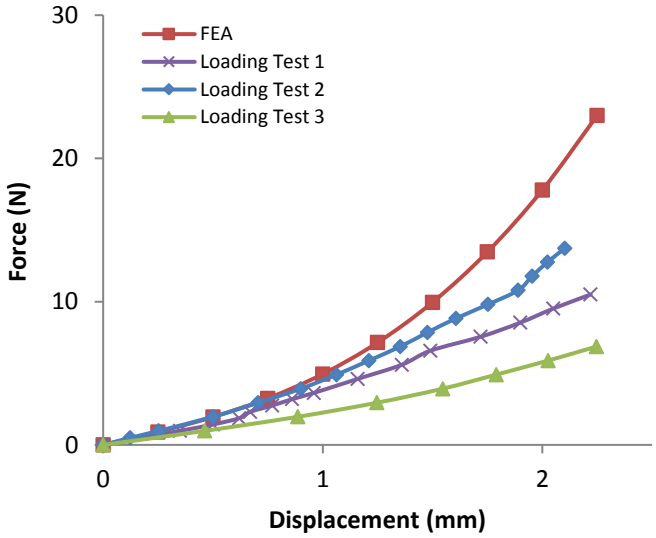

Figure 3.20 Loading test of the fabricated CMMS

3.3.4 Dynamic Analysis

A dynamic analysis of the CMMS is carried out with ABAQUS using the Lanczos Eigen solver. The first two modes, corresponding to simultaneous vibrations along both the X and Y axes , occurs at 60.75Hz.The third mode, corresponding to vibrations along the Z axis, occurs at a frequency of 187.98Hz, corresponding to a ratio of 1:3 between the X/Y-axes and the Z-axis.

In order to measure the frequency response of the fabricated CMMS, the testing rig from Section 3.2.1 is used. Labview is used to obtain the frequency domain response of each direction of motion using the FFT. The testing rig setup is presented in Figure 3.21. A peak in amplitude in each spectrum corresponds to the natural frequency along the corresponding direction of motion. The test is carried out after Test 3 from the previous section. The results are then compared with FEA, taking into account the mass of the accelerometer.

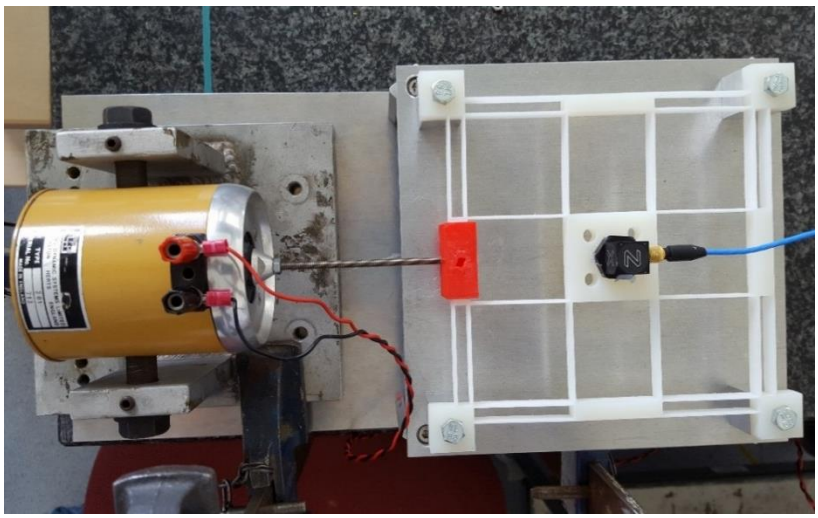

Figure 3.21 Vibration test rig

The natural frequencies are determined to occur at 37.33Hz, 38.33Hz and 120Hz for the X, Y and Z directions respectively. The FEA model including the weight of the screw and the accelerometer indicates the resonant frequencies of the first three modes occur at 49.75Hz, 49.75Hz and 149.83Hz respectively. The difference between FEA and the measured natural frequencies is postulated to be the result of lower than expected material stiffness as reported in the previous section.

3.4 Summary

In this chapter, a CMMS with a simple structure was proposed. Two linear models, the PRBM and the Euler-Bernoulli model, were used for comparison with FEA to evaluate their accuracy for large displacements. The conclusion drawn is that the linear models are only suitable for very small displacements which are around 70 times smaller than the beam's length for the initial design. The CMMS was characterised in terms of stiffness, working range, coupling and resonant frequencies and the impact of the beams' dimensions on these characteristics was evaluated. A first prototype was 3-D printed to evaluate the design. A full-scale Nylon-66 prototype was then fabricated using abrasive jet machining to investigate the use of polymer for CMMS rather than metal. The results show the unpredictability of the material properties as they are affected by environmental conditions, making it difficult to control. However, the material used combined with the machining technique and the low input force requirement make this CMMS suitable for low-cost applications.

Chapter 4 Nonlinear Modelling and Characterisation of a Compliant Micro-Motion XY Stage

It was demonstrated in Chapter 3 that the PRBM and the Euler-Bernoulli model are unsuitable for the design and optimisation of large displacement CMMSs. As discussed in Chapter 2, several nonlinear models have been developed in the past decade. Some of these models are proven to be efficient but are either complex or incomplete. The proposed model is an alternative to the PRBM and the BCM methods. It uses simple, well-established, beam bending equations and basic geometric properties to integrate the nonlinearities caused by large displacements, such as tension loading. The analytical model combines a 2-DOF nonlinear model to characterise the nonlinear stiffness and the workspace of the CMMS and a 6-DOF linear stiffness matrix to characterise the frequency response. The impact of dimensional parameters on the stiffness and travel range is evaluated and the model is implemented in MATLAB to perform design optimisation. A CMMS is then fabricated based on the optimisation results. Finally, FEA and experimental tests are compared to the analytical model for validation. While other models may accurately predict the nonlinear deformation of beams in parallelogram structures, this model allows for a full characterisation of the CMMS, including cross-coupling, motion loss and travel range with both nonlinear stress and buckling taken into account. This model can be used as a reliable design tool for any parallelogram structure but can also be included in the control system of a CMMS to compensate the displacement errors and allow for open-loop control.

4.1 Nonlinear Modelling of a Compliant Stage

The CMMS designed in this chapter is similar to the CMMS designed in Chapter 3 but the outer parallelogram structures are composed of two beams instead of four in order to lower the required actuation force. This design is similar to the design from [122].

4.1.1 Stiffness Modelling

The dimensional parameters of a beam are presented in Figure 3.5 and the dimensions of the CMMS are shown in Figure 4.1. The dimensions are given in meters and all the beams have the same dimensions.

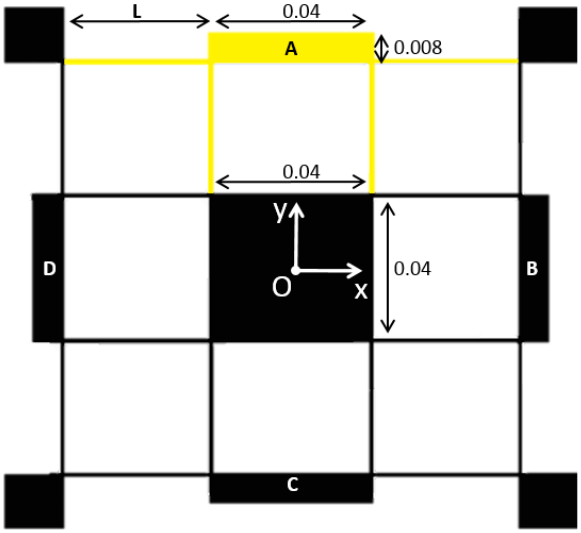

Figure 4.1 Schematic top view of the CMMS

Linear beam bending assumes an unchanged beam's length. However, this is not valid for large deflections. This is why a nonlinear model is derived by including the nonlinear term induced by tension loading of the beams. In deriving the nonlinear modelling of the CMMS shown in Figure 4.2, two types of compliant structure are analysed: the outer parallelogram structure (beams 1 to 8) and the inner parallelogram structure (beams 9 to 16).

All the beams are represented as linear-elastic elements connected to rigid bodies. In order to simplify the model, several assumptions have to be made. Firstly, parallelograms A and C can only translate along the Y-axis and parallelograms B and D can only translate along the X-axis. From these assumptions, the following boundary conditions can be established:

$$\begin{cases} \delta_{Ay} = \delta_{1y} = \delta_{2y} \\ \delta_{Cy} = \delta_{5y} = \delta_{6y} \\ \delta_{Bx} = \delta_{3x} = \delta_{4x} \\ \delta_{Dx} = \delta_{7x} = \delta_{8x} \end{cases} \tag{4.1}$$

where δ_{Ay} represents the displacement of point A along the Y-axis, δ_{1y} represents the displacement of beam 1 along the Y-axis and so on. Applying this assumption to the analysis is essential to obtain a simple model but it may introduce small errors in the results. However, since the axial stiffness of the beams is much greater than the bending stiffness, the transverse displacement of the outer parallelograms is very small and the error is minimal.

As a consequence of the previous assumption, the following is clear:

$$\begin{cases} F_{Ay} = F_{1y} + F_{2y} \\ F_{Cy} = F_{5y} + F_{6y} \\ F_{Bx} = F_{3x} + F_{4x} \\ F_{Dx} = F_{7x} + F_{8x} \end{cases} \tag{4.2}$$

where F_{Ay} represents the reaction force of the parallelogram A for an input displacement δ_{Ay}, F_{1y} represents the reaction force of the beam 1 for an input displacement δ_{1y} and so on.

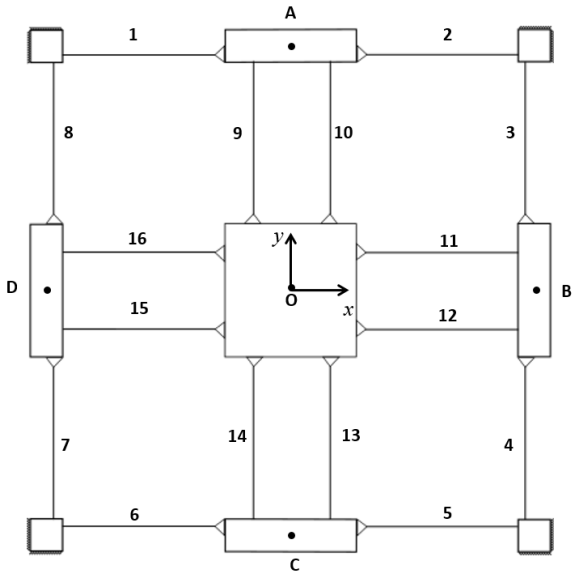

Figure 4.2 Nonlinear spring-equivalent model of the CMMS

a) Outer parallelogram

The total stiffness of one outer parallelogram structure can be obtained from the modelling of a single beam Figure 4.3. In this model, the stiffness due to bending is combined with the stiffness induced by tension.

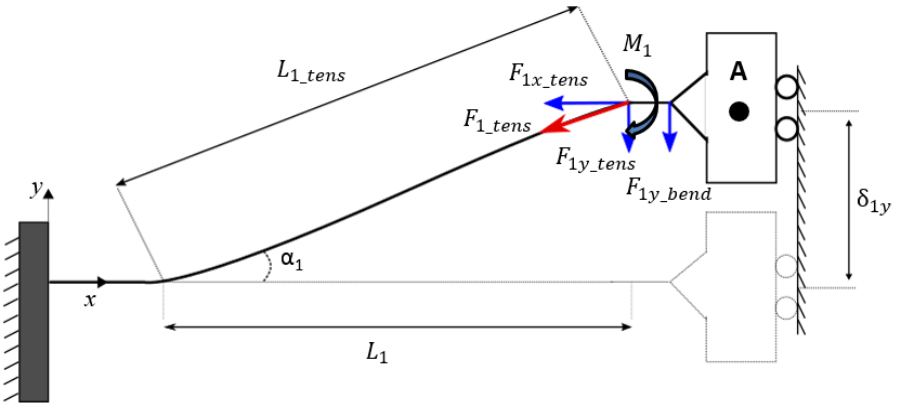

Figure 4.3 Spring-equivalent model of a beam

Effect of bending

As in Eq. (3.12) from Section 3.1.2, the force F_{1y_bend} acting downwards due to the bending of the beam can be expressed as :

$$F_{1y\_bend} = \frac{12EI_z\delta_{1y}}{L_1^3} \tag{4.3}$$

where I_z is the area moment of inertia and L_1 is the initial length of beam 1.

Effect of tension

In the tension analysis, bending is ignored and the beam is regarded as a linear spring connected at both ends by frictionless revolute joints. It is known that the stress induced by tension loading is given by:

$$\sigma_{1\_tens} = \varepsilon_1 E = \frac{F_{1\_tens}}{A} \tag{4.4}$$

where σ_{1_tens} is the stress generated by pure tension loading on beam 1, ε_1 is the strain on beam 1, A is the cross-sectional area of the beam and F_{1_tens} is the tension load applied to beam 1. The length of the beam after being stretched is approximated using Pythagoras theorem:

$$L_{1\_tens} = \sqrt{L_1^2 + \delta_{1y}^2} \tag{4.5}$$

where L_{1_tens} represents the elongated length of beam 1 and L_1 represents the initial length of beam 1. The value of the strain ε_1 is then:

$$\varepsilon_1 = \frac{\Delta L_1}{L_1} = \frac{L_{1\_tens} - L_1}{L_1} \tag{4.6}$$

The relationship between the tension force $\mathrm{F}_{1\_\mathrm{tens}}$ and the resulting force F_{1y_tens} acting downwards is given by:

$$F_{1y\_tens} = F_{1\_tens} \sin\alpha_1 \tag{4.7}$$

with:

$$\alpha_1 = \tan^{-1}\left(\frac{\delta_{1y}}{L_1}\right) \tag{4.8}$$

Rearranging Eqs. (4.4) to (4.8), the force due to tension is:

$$F_{1y\_tens} = EA\varepsilon_1 \sin\alpha_1 \tag{4.9}$$

From Eqs. (4.3) and (4.9), the total force applied by beam 1 acting along the Y-axis is therefore:

$$F_{1y} = F_{1y\_bend} + F_{1y\_tens} \tag{4.10}$$

b) Inner parallelogram

Because of the symmetrical boundary conditions, the total stiffness of one inner parallelogram structure (for instance beams 15 and 16) can be derived from a single beam coupled to one half of the outer parallelogram structure linked to it (Figure 4.4).

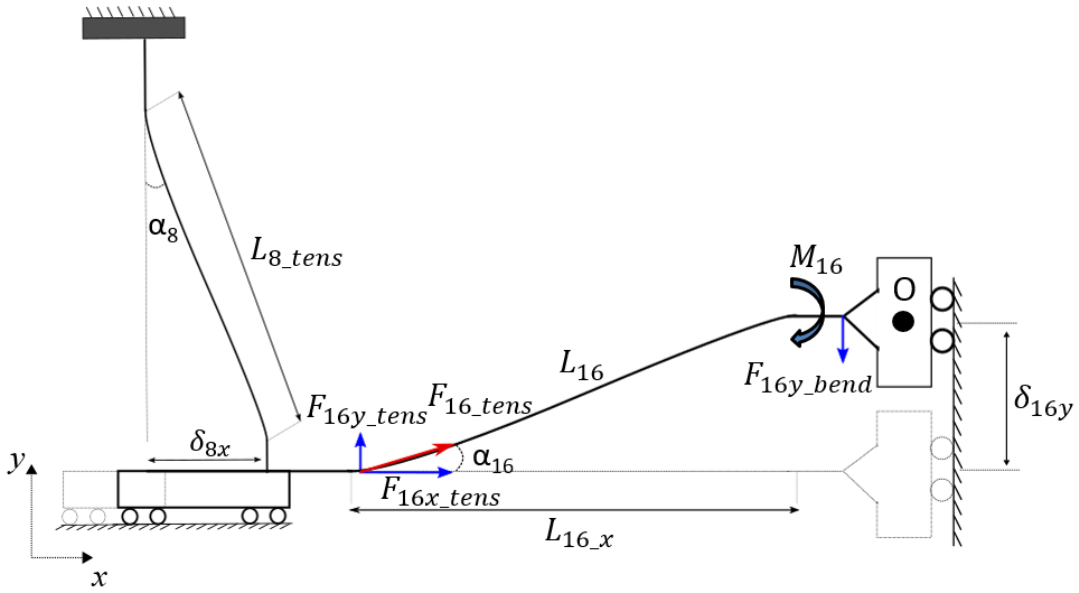

Figure 4.4 Spring-equivalent model of orthogonal beam configuration

The stiffness K_{16x} of the beam 16 along the X-axis is given by:

$$K_{16x} = \frac{EA}{L_{16}} \cos \alpha_{16} \tag{4.11}$$

For small angles, the following approximation can be made:

$$K_{16x} \approx \frac{EA}{L_{16}} \tag{4.12}$$

The stiffness of beam 8 along the X-axis K_{8x} is derived as follows:

Firstly, the stiffness due to bending is:

$$K_{8x\_bend} = \frac{12EI_z}{L_8^3} \tag{4.13}$$

Then, the stiffness due to tension is:

$$K_{8x\_tens} = \frac{EA}{L_8} \sin \alpha_8 \tag{4.14}$$

Therefore, the total resulting stiffness of beam 8 along the X-axis is:

$$K_{8x} = K_{8x\_bend} + K_{8x\_tens} \tag{4.15}$$

For a small displacement δ_{16} and therefore a very small displacement δ_8 and angle α_8, it is observed that:

$$K_{8x} \ll K_{16x} \tag{4.16}$$

From this observation and to simplify the model, the change in axial deformation of the beams of the inner parallelogram is neglected here. It will be included later for motion loss compensation. The projection of beam 16 along the X-axis is:

$$L_{16\_x} = \sqrt{L_{16}^2 - \delta_{16}^2} \tag{4.17}$$

The deflection of beam 8 can be obtained as follows:

$$\delta_{8x} = L_{16} - L_{16\_x} \tag{4.18}$$

Taking all these simplifications into account, the calculation of the relationship between δ_{8x} and F_{16y} can be determined.

Based on Eq. (4.10), the force acting along the X-axis is:

$$F_{16x\_tens} = \frac{12EI_z}{L_8^3}\delta_{8x} + \frac{EA}{L_8}\Delta L_8 \sin\alpha_8 \tag{4.19}$$

The force acting along the Y-axis is therefore a combination of the forces applied by beams 8 and 16:

$$F_{16y} = \frac{F_{16x\_tens}\delta_{16y}}{L_{16\_x}} + \frac{12EI_z\delta_{16y}}{L_{16}^3} \tag{4.20}$$

c) Force-displacement model of the CMMS

From the preliminary assumptions, the boundary conditions and the above derivations, the position of each outer parallelogram can be related to the position of the centre O as follows:

$$\delta_{Ay} = \delta_{Oy} - \left(L - \sqrt{L^2 - \delta_{Ox}^2}\right) \tag{4.21}$$

$$\delta_{Cy} = \delta_{Oy} + \left(L - \sqrt{L^2 - \delta_{Ox}^2}\right) \tag{4.22}$$

$$\delta_{Bx} = \delta_{Ox} - \left(L - \sqrt{L^2 - \delta_{Oy}^2}\right) \tag{4.23}$$

$$\delta_{Dx} = \delta_{Ox} + \left(L - \sqrt{L^2 - \delta_{Oy}^2}\right) \tag{4.24}$$

Using Eqs. (4.10) and (4.20), the reaction forces at point O along the X- and the Y-axes required to move the CMMS by δ_{Ox} and δ_{Oy} are:

$$\begin{cases} F_{Ox} = F_{Bx} + F_{Dx} + F_{9x} + F_{10x} + F_{13x} + F_{14x} \\ F_{Oy} = F_{Ay} + F_{Cy} + F_{11y} + F_{12y} + F_{15y} + F_{16y} \end{cases} \tag{4.25}$$

It is assumed that the sum of the reaction forces along the X-axis is unchanged when represented at points B, D or O, and the sum of the forces along the Y-axis is unchanged when represented at points A, C or O.

d) Motion loss compensation

The simplified nonlinear model presented in this section assumes that the input displacements are applied at the centre of the CMMS (i.e. point O). This means that the desired output displacements are simply equal to the input displacements. In reality, the input displacements are applied by two actuators at point D along the X-axis and at point C along Y-axis, causing the output displacements at point O to be different.

The first element causing a difference between the input and the output displacements is the compression of the inner beams. Based on the work from [140] and using Eq. (4.4), the positioning error at point O along the X-axis error caused by the compression of beams 15 and 16 can be approximated as follows:

$$\delta_{Ox\_com} = \frac{L(F_{Bx}+F_{9x}+F_{10x}+F_{13x}+F_{14x})}{2EA} \tag{4.26}$$

Similarly, the positioning error at point O along the Y-axis caused by the compression of beams 13 and 14 is:

$$\delta_{Oy\_com} = \frac{L(F_{Ay}+F_{11y}+F_{12y}+F_{15y}+F_{16y})}{2EA} \tag{4.27}$$

The second source of error is the parasitic displacement caused by the constrained positions of parallelograms C and D, also called cross-coupling. The parasitic displacement along the X-axis can be estimated by calculating the difference between the desired output displacement δ_{Ox} and the resulting displacement δ_{Dx} of parallelogram D:

$$\delta_{Ox\_par} = \delta_{Ox} - \delta_{Dx} \tag{4.28}$$

Similarly, the parasitic displacement along the Y-axis can be estimated by calculating the difference between the input displacement δ_{Oy} and the resulting displacement δ_{Cy} of parallelogram C:

$$\delta_{Oy\_par} = \delta_{Oy} - \delta_{Cx} \tag{4.29}$$

Therefore, the corrected output displacement at point O along the X-axis is:

$$\delta_{Ox\_corrected} = \delta_{Ox} - \delta_{Ox_{com}} + \delta_{Ox_{par}} \tag{4.30}$$

and the corrected output displacement at point O along the Y-axis is:

$$\delta_{Oy\_corrected} = \delta_{Oy} - \delta_{Oy\_com} + \delta_{Oy\_par} \tag{4.31}$$

4.1.2 Travel Range Limitations

A nonlinear stress analysis is carried out to define the maximum allowable displacement of the CMMS, which is directly linked to the yield strength of the material. The maximum stress due to bending occurs at one end of the outer parallelogram beams at the farthest edge from the neutral axis of the cross-section. It is given by:

$$\sigma_{1\_bend} = \frac{M_1 c}{I} \tag{4.32}$$

where c is the distance from the neutral axis, or half of the beam's thickness h in this case, and $M_1 = F_{1y\_bend} \times 0.5 \times L_1$.

Combining Eqs. (4.3) and (4.32), the maximum stress due to bending is:

$$\sigma_{1\_\mathrm{bend}} = \frac{3Eh\delta_{1\mathrm{y}}}{L_1^2} \tag{4.33}$$

Adding the stress induced by tension loading from Eq.(4.4), the maximum stress is given by:

$$\sigma_1 = K1 \cdot \sigma_{1\_\mathrm{bend}} + K2 \cdot \sigma_{1\_\mathrm{tens}} \tag{4.34}$$

where $K1$ and $K2$ denote the stress concentration factors for the stress due to bending and the stress due to tension respectively. These coefficients will be defined later in this thesis.

Buckling should occur at one of the inner beams parallel to the loading direction and where the reaction force is the highest. Since there are only sets of two beams, it is assumed that the buckling force is twice F_{crit}. When a force $F_{applied}$ is applied at the bottom of the CMMS (Figure 4.5a)), the reaction force $F_{buckling}$ acting on the set of beams 13 and 14 is obtained by subtracting the reaction force of parallelogram C from the reaction force of the whole CMMS along the same direction. It is assumed that buckling occurs for a large input displacement, when the nonlinear term induced by tension loading becomes much higher than the linear term. Comparing Eqs. (4.10) and (4.20), if an input displacement is applied at point C along Y direction, the larger the displacement, the more insignificant becomes the reaction forces caused by the inner beams compared to the reaction forces from parallelograms A and C. Thus, the buckling force $F_{buckling}$ is approximately $1/2$ of the force applied at the bottom of the CMMS $F_{applied}$. The input force required to cause buckling is therefore given by:

$$F_{applied} = \frac{16\pi^2 EI}{L^2} \tag{4.35}$$

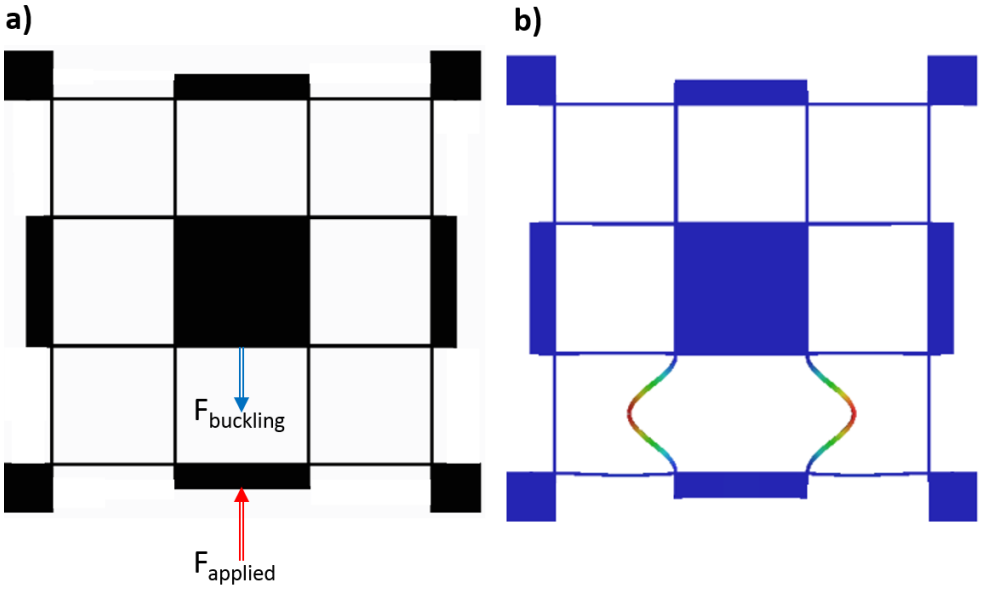

Figure 4.5 Buckling: a) Force diagram, b) FEA result

4.2 Dynamic Model of a Compliant XY Stage

4.2.1 Stiffness Matrix

Firstly, a stiffness matrix is derived to create a dynamic model of the CMMS. A 6-DOF representation allows the model to be used for a wide range of applications. The main purpose of the stiffness matrix is to calculate the resonant frequencies of the CMMS. It will also be used for comparison with the nonlinear model, FEA and experimental test results.

4.2.1.1 General Beam Modelling and Transformation

The static equation of the beam presented in Figure 3.5 can be written as in [149, 194]:

$$\underline{F} = K_{fix\_g}.\underline{X} \tag{4.36}$$

where $\underline{F}$ is a vector representing the forces and moments applied at the end of the beam, K_{fix_g} is the stiffness matrix of the beam with fixed-guided boundary conditions and $\underline{X}$ is a vector representing the translations and rotations at the end of the beam. The static equation can therefore be written as follows:

$$\begin{pmatrix} F_x \\ F_y \\ F_z \\ M_x \\ M_y \\ M_z \end{pmatrix} = \begin{bmatrix} \frac{EA}{L} & 0 & 0 & 0 & 0 & 0 \\ 0 & \frac{12EI_z}{L^3} & 0 & 0 & 0 & \frac{6EI_z}{L^2} \\ 0 & 0 & \frac{12EI_y}{L^3} & 0 & -\frac{6EI_y}{L^2} & 0 \\ 0 & 0 & 0 & \frac{GJ}{L} & 0 & 0 \\ 0 & 0 & -\frac{6EI_y}{L^2} & 0 & \frac{4EI_y}{L} & 0 \\ 0 & \frac{6EI_z}{L^2} & 0 & 0 & 0 & \frac{4EI_z}{L} \end{bmatrix} \begin{pmatrix} \delta_x \\ \delta_y \\ \delta_z \\ \theta_x \\ \theta_y \\ \theta_z \end{pmatrix} \tag{4.37}$$

where F_n and δ_n are the force and translation along the n axis, M_n and θ_n are the moment and rotation around the n axis, G is the shear modulus, A is the area of the beam's cross section, J is the torsion constant and I_y and I_z are the area moments.

The stiffness of a beam can be shifted from its local coordinate system to a general coordinate system by using the shifting law from screw theory and the work reported in [110, 146, 194-196]. This process involves pre-multiplying the stiffness matrix in coordinate system O_i by the inverse transpose of the adjoint transformation matrix and then multiplying it by the inverse of the adjoint transformation matrix, as shown below:

$$K_i^j = {T_i^j}^{-T} \cdot K_i \cdot {T_i^j}^{-1} \tag{4.38}$$

where i represents the local coordinate system of the beam and j represents the coordinate system in which the beam's stiffness is shifted. Figure 4.6 shows an example of the stiffness of a compliant beam at its end being shifted from O_i to O_j using Eq. (4.38).

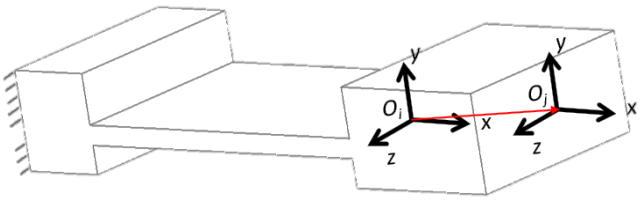

Figure 4.6 Coordinate transformation

The adjoint transformation matrix T_i^j is:

$$T_i^j = \begin{bmatrix} R_i^j & S(p_i^j).R_i^j \\ 0 & R_i^j \end{bmatrix} \tag{4.39}$$

where R_i^j represents the rotation matrix of O_i relative to O_j and $S(p_i^j)$ represents the skew symmetric operator for the vector $p_i^j = |p_x, p_y, p_z|$, denoted as:

$$S(p_i^j) = \begin{bmatrix} 0 & -p_z & p_y \\ p_z & 0 & -p_x \\ -p_y & p_x & 0 \end{bmatrix} \tag{4.40}$$

The rotation matrix R_i^j is obtained by multiplying the rotation matrices around each axis:

$$R_i^j = Rx_i^j . Ry_i^j . Rz_i^j \tag{4.41}$$

where Rx_i^j represents the rotation matrices around the X-axis by the angle ϕ,

$$Rx_i^j = \begin{bmatrix} 1 & 0 & 0 \\ 0 & \cos\phi & -\sin\phi \\ 0 & \sin\phi & \cos\phi \end{bmatrix} \tag{4.42}$$

Ry_i^j represents the rotation matrices around the Y-axis by the angle Ψ,

$$Ry_i^j = \begin{bmatrix} \cos\Psi & 0 & \sin\Psi \\ 0 & 1 & 0 \\ -\sin\Psi & 0 & \cos\Psi \end{bmatrix} \tag{4.43}$$

and Rz_i^j represent the rotation matrices around the Z-axis by the angle θ.

$$Rz_i^j = \begin{bmatrix} \cos\theta & 0 & \sin\theta \\ 0 & 1 & 0 \\ -\sin\theta & 0 & \cos\theta \end{bmatrix} \tag{4.44}$$

4.2.1.2 Individual Parallelogram Modules Stiffness

Due to the symmetry of the design, the overall stiffness can be obtained by only deriving the stiffness of the top quarter composed of beams 1, 2, 9 and 10 (Figure 4.1).

Firstly, the stiffness of the parallelogram A, composed of the beams 1 and 2, is represented at the centre of the CMMS, at point O. The stiffness of beam 1 at point O is obtained by translating the beam's stiffness matrix K_1 along the X- and Y-axes using Eq. (4.38), giving:

$$K_1^O = {T_1^O}^{-T} \cdot K_1 \cdot {T_1^O}^{-1} \tag{4.45}$$

with $K_1 = K_{fix\_g}$ and $p_1^O = |0.02, -(L + 0.02), 0|$. Since beams 1 and 2 are symmetric about the Y-axis, the stiffness of beam 2 at point O is found by rotating the stiffness matrix of beam 1 at point O around the Y-axis by π radians:

$$K_2^O = Ry(\pi)_2^{O\,-T} \cdot K_1^O \cdot {Ry(\pi)_2^O}^{-1} \tag{4.46}$$

The stiffness of beam 9 at point O is obtained by rotating the initial beam stiffness matrix by $-\pi\ /\ 2$ around the Z-axis and translating by $p_9^O = |0.02, -0.02, 0|$:

$$K_9^O = {T_9^O}^{-T} \cdot K_{fix\_g} \cdot {T_9^O}^{-1} \tag{4.47}$$

Since beams 9 and 10 are symmetric about the Y-axis, the stiffness of beam 10 at point O is obtained by rotating beam 9 around the Y-axis by π radians:

$$K_{10}^{O} = Ry(\pi)_{2}^{O^{-T}} \cdot K_{9}^{O} \cdot Ry(\pi)_{2}^{O^{-1}} \tag{4.48}$$

The beams 1 and 2 are in a parallel configuration with the parallelogram A and the beams 9 and 10 are in a parallel configuration with the centre of the CMMS O. The pairs of beams 1-2 and 9-10 are in a serial configuration with the centre of the CMMS O. Therefore, the stiffness of the top quarter of the CMMS at point O is:

$$K_{O1} = \frac{1}{\left(K_{1}^{O}+K_{2}^{O}\right)^{-1}+\left(K_{9}^{O}+K_{10}^{O}\right)^{-1}} \tag{4.49}$$

4.2.1.3 Stiffness of the CMMS

The stiffness of the remaining three quarters is obtained by successively rotating K_{O1} three times by $-\pi\ /\ 2$ around the Z-axis as follows:

$$K_{O2} = Rz(-\frac{\pi}{2})_{O}^{\ -T} \cdot K_{O1} \cdot Rz(-\frac{\pi}{2})_{O}^{\ -1} \tag{4.50}$$

$$K_{O3} = Rz(-\frac{\pi}{2})_{O}^{\ -T} \cdot K_{O2} \cdot Rz(-\frac{\pi}{2})_{O}^{\ -1} \tag{4.51}$$

$$K_{O4} = Rz(-\frac{\pi}{2})_{O}^{\ -T} \cdot K_{O3} \cdot Rz(-\frac{\pi}{2})_{O}^{\ -1} \tag{4.52}$$

with K_{O2}, K_{O3} and K_{O4} representing the stiffness of the groups of beams 3-4-11-12, 5-6-13-14 and 7-8-15-16 at point O respectively. The stiffness matrix K of the whole CMMS is therefore:

$$K = K_{O1} + K_{O2} + K_{O3} + K_{O4} \tag{4.53}$$

4.2.2 Dynamic Model

A dynamic analysis is carried out to calculate the resonant frequencies of the six mode shapes. Applying Newton's second law, the system's undamped equation of motion can be expressed as:

$$M\underline{\ddot{x}} + K\underline{x} = 0 \tag{4.54}$$

where M and K correspond to the system's mass matrix and stiffness matrix respectively and $\underline{x}$ is a vector representing the motion in the Cartesian coordinate system. The mass matrix is defined as:

$$M = \begin{bmatrix} M_{xx} & 0 & 0 & 0 & 0 & 0 \\ 0 & M_{yy} & 0 & 0 & 0 & 0 \\ 0 & 0 & M_{zz} & 0 & 0 & 0 \\ 0 & 0 & 0 & I_{xx} & 0 & 0 \\ 0 & 0 & 0 & 0 & I_{yy} & 0 \\ 0 & 0 & 0 & 0 & 0 & I_{zz} \end{bmatrix} \quad (4.55)$$

where M_{xx}, M_{yy} and M_{zz} represent the moving mass of the CMMS along the X-, Y- and Z-axes respectively and I_{xx}, I_{yy} and I_{zz} represent the moment of inertia of the CMMS around the X-, Y- and Z-axes respectively:

$$M_{xx} = M_{yy} = m_O + 2m_p + \left(8 \times \frac{33}{140} m_{beam}\right) + (4 \times m_{beam}) \quad (4.56)$$

$$M_{zz} = m_O + \left(8 \times \frac{33}{140} m_{beam}\right) \quad (4.57)$$

$$I_{xx} = I_{yy} = \frac{m_o(0.04^2+b^2)}{12} + 2m_p\left(\frac{0.008^2+b^2}{12} + (L+0.02)^2 + \frac{(0.04^2+b^2)}{12}\right) \quad (4.58)$$

$$I_{zz} = 4m_p\left(\frac{0.04^2+0.008^2}{12}\right) + m_o\left(\frac{0.04^2+0.04^2}{12}\right) \quad (4.59)$$

Based on vibration theory [197, 198], the mode equation can be written as:

$$(M^{-1}K - \omega^2 I)X = 0 \quad (4.60)$$

where X is a matrix representing the mode shapes, ω is a vector representing the corresponding angular natural frequencies and I is the identity matrix. The natural frequencies are then given by:

$$f_i = \frac{1}{2\pi}\omega_i \quad (4.61)$$

where f_i represents the natural frequency of the i^{th}mode.

The masses used in the mass matrix are listed in Table 4.1. m_{beam} is the mass of a single beam. According to [199], the lumped mass equivalent of a bending beam can be represented as a massless beam with a mass located at its free end with the value of $33/140 \times m_{beam}$. m_o represents the mass of parallelogram O and m_p represents the mass of each outer parallelograms (i.e. A, B, C and D).

Parameters	m_O	m_p	m_{beam}
Mass (10^{-3} kg)	$0.04^2 \times b \times \rho$	$0.04 \times 0.008 \times b \times \rho$	$b \times h \times L \times \rho$

Table 4.1 Masses of a beam, inner, and outer parallelogram

4.3 Design Optimisation

Using the analytical model presented in Sections 4.1 and 4.2 rather than FEA enables quick design synthesis and an insight on the importance of geometrical parameters due to

its high flexibility. The optimisation is focused on four properties of the CMMS: the resonant frequencies of the first two modes, these should occur equally along the *X*- and the *Y*-axes; the third resonant frequency; the maximum allowable displacement and the corresponding force input requirement. The maximum displacement is defined using the yield strength of the material and the buckling point of the beams. Coupling and motion loss are ignored in this section because their impact on the beam dimensions is negligible.

In the first instance, the beam thickness (h), height (b) and length (L) are varied from 0.5mm to 1mm, 5mm to 10mm and 20mm to 50mm, respectively. This allows for an overview of the effect of dimensional parameters on the CMMS's behaviour. The equations resulting from the analytical model are therefore implemented in MATLAB and the results are shown in Figure 4.7. Aluminium 7075-T6 is selected as it has a large reversible strain and is widely used for this application. The material properties are listed in Table 4.2. Observations similar to Chapter 3 can be made. First of all, increasing the length of the beams will increase the maximum allowable displacement. However, this will also reduce the resonant frequencies. Increasing the height of the beams results in an increased third resonant frequency without affecting the range of motion.

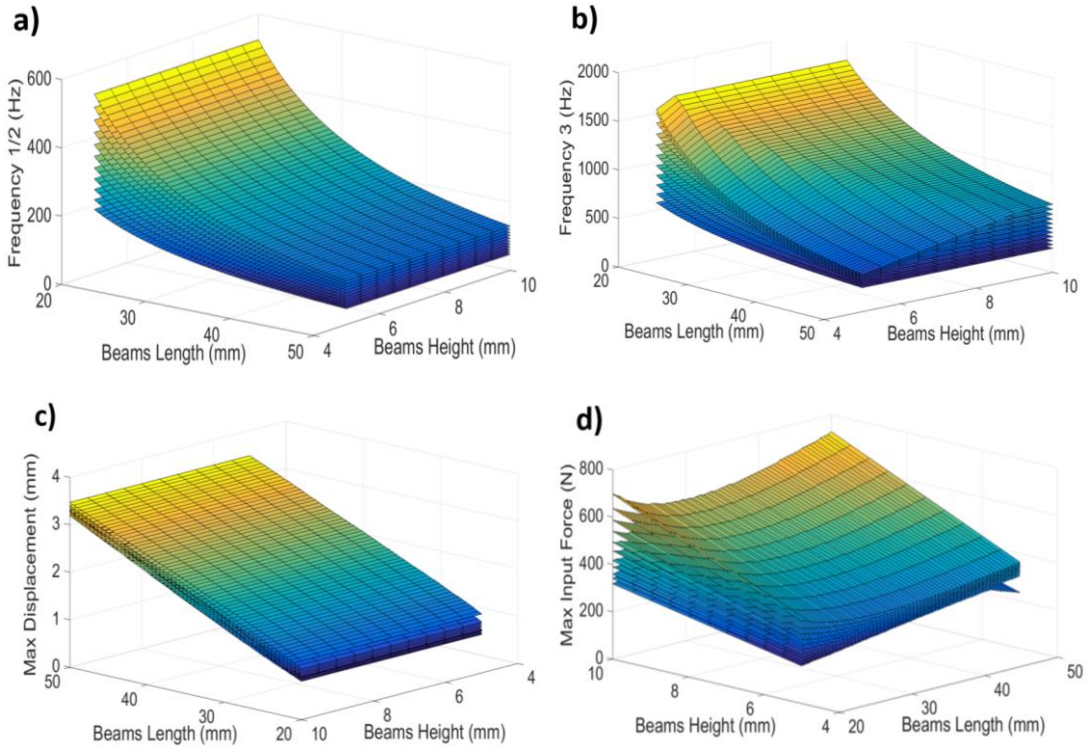

Figure 4.7 Properties of the CMMS as a function of the height, length and thickness of the beams. a) first and second resonant frequencies, b) third resonant frequency, c) maximum displacement, d) input force. (NB: each layer corresponds to a different beam thickness between 0.5mm and 1mm)

However, the force input requirement is also increased. Finally, increasing the thickness of the beams will increase the resonant frequencies along the three axes but will reduce the range of motion and increases the force input requirement. These observations comply with the results found in the literature for similar structures.

Optimisation of PRBM parameters was proposed in [144] and allows the user to find which model is the most suitable for a given design. However, it does not optimise the beams' dimensions to achieve a specific goal. Design optimisation using genetic algorithms (GAs) [89, 120, 153, 200, 201] or other techniques such as particle swarm optimisation (PSO) [102, 110, 202] are commonly used for CMMSs but the presented models do not include the nonlinearities induced by tension, making them only suitable for small displacements.

The design optimisation is performed using a multi-objective GA [203] to obtain a Pareto optimal solution set in MATLAB. The design objectives are to maximise the range of motion and minimize the required input force while keeping the resonant frequencies as high as possible. The design constraints applied are:

- Resonant frequencies f_1 and $f_2 > 50Hz$.
- Minimum frequency ratio $f_1/f_3 > 1/3$.
- Maximum stress $\sigma_{max} < 505MPa$.
- Maximum input $F_{Ox} < F_{applied}$, corresponding to the buckling point.

The parameters ranges are:

- $b = 6mm$ (manufacturing constraint)
- $0.5mm < h < 1mm$
- $20mm < L < 50$mm

The Pareto optimal set is presented in Figure 4.8. For each point on the Pareto front corresponds a set of beam parameters. The rounded dimensions selected for the final design of the CMMS are shown in Table 4.2. Applying a safety factor of 1.5 on the maximum stress and limiting the required input force to 68N, these dimensions allow for an input displacement of up to ±2.3mm along both directions.

Parameters	**b (m)**	**h (m)**	**L (m)**	**E (Pa)**	**G (Pa)**	**ρ (kg/m3)**
Values	0.006	0.0005	0.045	$71{,}7e^{9}$	$26{,}9e^{9}$	2810

Table 4.2 Parameters of the CMMS

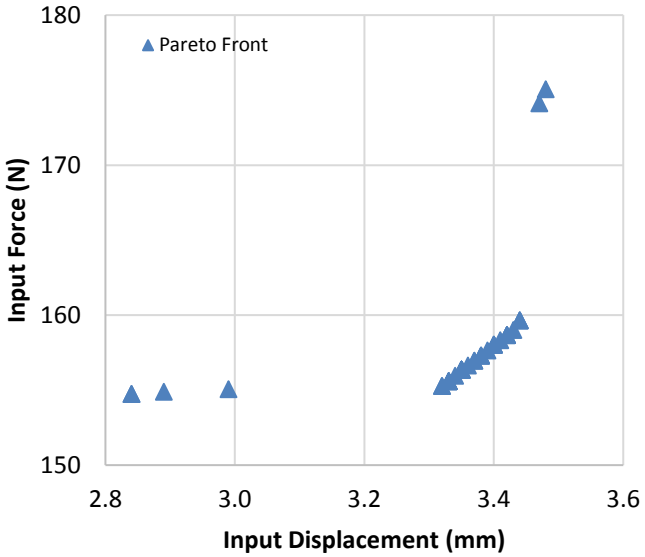

Figure 4.8 Pareto front

The average computation time for the MATLAB program to run on a standard computer (Intel® i5 3.2GHz processor, 4GB RAM) is less than 140 seconds to cover more than 26000 combinations. This algorithm is therefore proven to be significantly more efficient than FEA for the design and evaluation of the appropriate dimensional parameters of the CMMS. This tool can be used to characterise the CMMS in terms of working area and stiffness and can be used to select the appropriate dimensional parameters of the beams and actuators.

4.4 Evaluation of the Nonlinear Model Using FEA

In order to validate the analytical model, nonlinear FEA is carried out using ABAQUS with the dimensions and properties listed in Table 4.2. In order to reduce the stress concentration, corners of 0.5mm radius have been added at both ends of the beams.

4.4.1 Force-Displacement Analysis

To study the force-displacement relationship, an input displacement of 2mm is gradually applied along the X-axis (i.e. point D on Figure 4.1) and the reaction force is recorded.

The results (Figure 4.9) are then compared with the analytical linear (Eq. (4.53)) and nonlinear (Eq. (4.25)) models. The experimental results will be discussed in Section 4.5. These results clearly show that although some linear behaviour can be observed between

0 and 0.5mm, the load stiffening phenomena induces significant nonlinearities for large displacements. The accuracy of the stiffness matrix method is therefore limited to very small range. However, the maximum error of the nonlinear model is 16.2% at 1.3mm, corresponding to only 3.2N. The efficiency of the nonlinear terms added to the analytical model to define the stiffness is therefore validated.

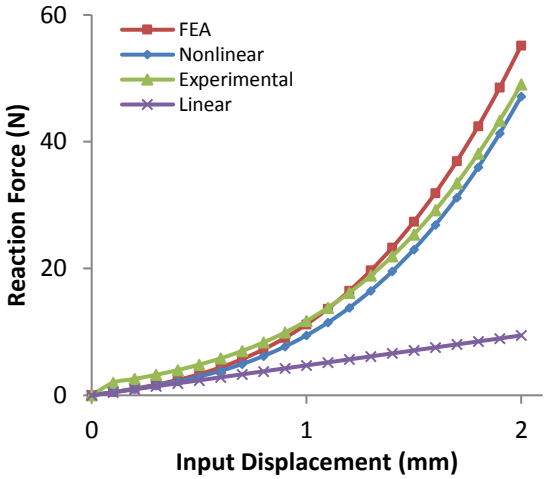

Figure 4.9 Stiffness along a single direction

4.4.2 Stress Analysis

In order to define the stress concentration factors K1 and K2 for Eq. (4.34), an FEA analysis is carried out on beams of lengths between 20mm and 50mm and thickness between 0.5mm and 1mm, with a constant corner radius of 0.5mm. For each combination, the resulting stress is plotted against the input displacement and MATLAB is used to fit the curve to Eq. (4.34) using the nonlinear least squares method. The results of this analysis are shown in Figure 4.10. Because K1 and K2 cannot be lower than 1, the coefficient K2 is constantly 1 and K1 varies between 1 and 2.10. The stress concentration factor K1 of the designed CMMS, obtained by linear interpolation, is 2. The FEA results show that the yield strength is reached for an input displacement of 3.24mm (Figure 4.11). The yield strength is reached at 3.1mm for the nonlinear model and at 9.51mm for the linear model. The maximum input displacement given by the analytical model is therefore 4.3% smaller than FEA. As for the force-displacement analysis, it is clearly shown that the nonlinear model can also efficiently integrate nonlinear stress as a travel range limitation.

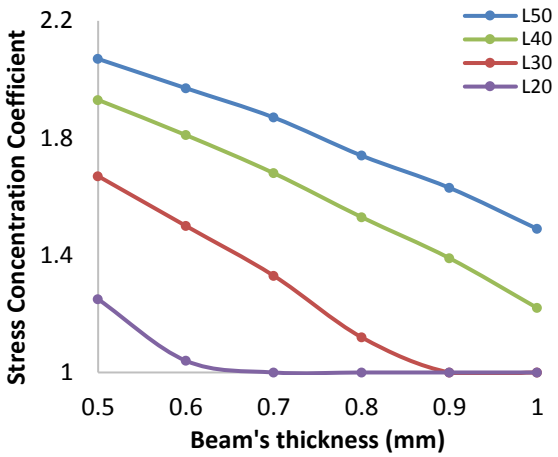

Figure 4.10 Stress concentration coefficients in function of the beam's thickness and length

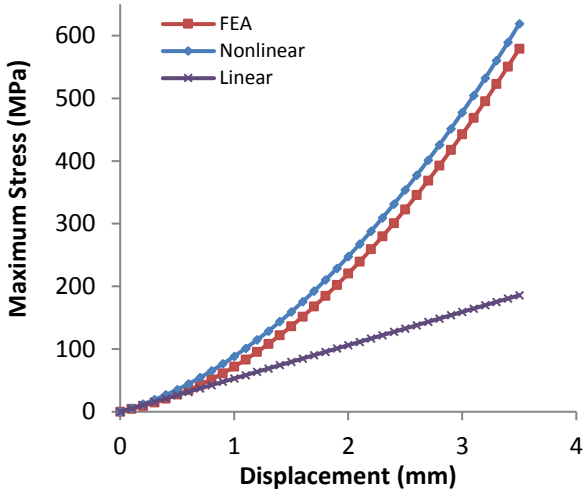

Figure 4.11 Stress analysis: linear and nonlinear models compared with FEA

4.4.3 Buckling Analysis

The buckling point is estimated from the FEA results by analysing the output data for a large displacement. Buckling is occurring when the stress at the centre of the inner beams increases suddenly and the difference between the input and the output displacement of the CMMS increases significantly. From Figure 4.12, the buckling point is estimated to occur when the input displacement is around 4.05mm, corresponding to an input force of 351.3N. The buckling point obtained from the nonlinear model (Eq. (4.35)) gives an input force of 349.5N, corresponding to an input displacement of 4.13mm. The error between FEA and the nonlinear model is therefore 0.5%. The deformed shape of the CMMS after buckling is shown in Figure 4.5b).

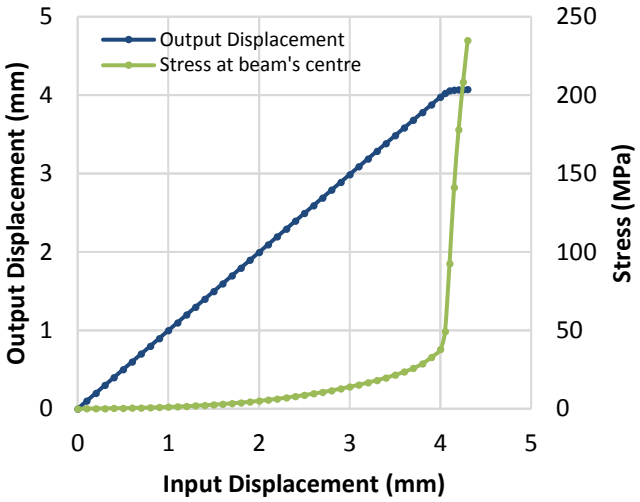

Figure 4.12 Stress and output displacement response to a large input displacement

4.4.4 Coupling Analysis

A coupling analysis is carried out to estimate the maximum positioning error and to evaluate the capability of the analytical model to predict this error. The maximum error is assumed to occur when the maximum input displacements are applied simultaneously along the X- and the Y-axes.

First, an input displacement of 2.2mm is applied at point C along the Y-axis, as presented in Figure 4.13. The parasitic output displacement along the X-axis is shown in Figure 4.14. The maximum parasitic displacement from the analytical model is 54µm while it is 65µm from FEA, corresponding to an error of 17%.

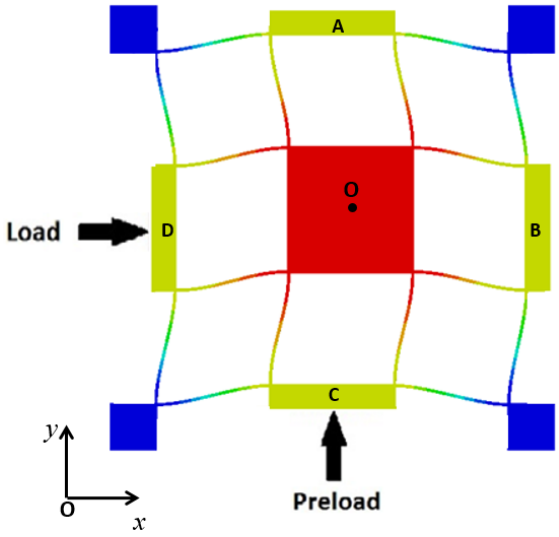

Figure 4.13 Deformed CMMS with input displacement applied along X and Y directions

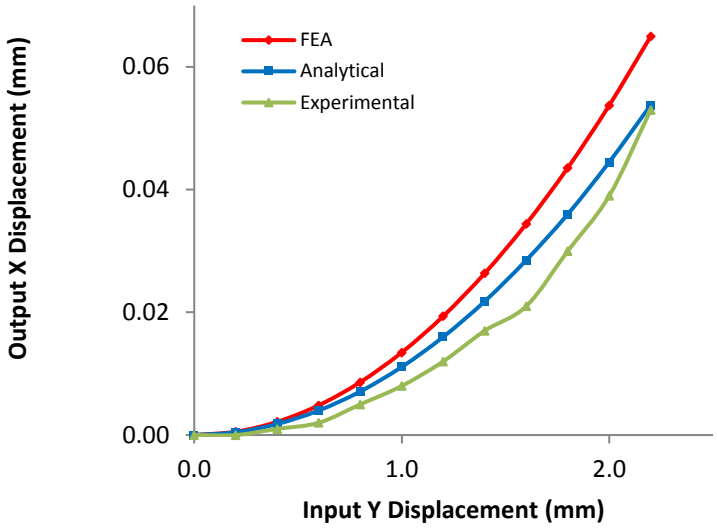

Figure 4.14 Parasitic displacement for single direction loading

Then, while keeping the input displacement along the Y-axis at 2.2mm, an input displacement of 2.2mm is gradually applied at point D along the X-axis. The difference between the input and output displacements along both directions are shown in Figure 4.15. The first observation made is that the parasitic displacement along the X-axis caused by the preload is almost constant for both FEA and the analytical model. The second observation is that the input/output displacement difference along both directions is the same for FEA and the analytical model, with less than 0.5% error. The nonlinear model can therefore accurately predict cross-coupling and lost motion and can therefore be included in the control system for error compensation.

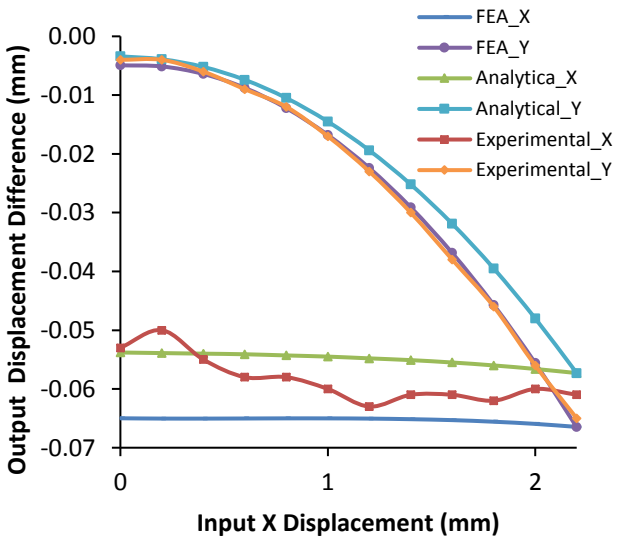

Figure 4.15 Input/output displacement difference after applying a preload along the Y-axis

4.4.5 Modal Analysis

A dynamic analysis of the CMMS is carried out with ABAQUS. The mass of the accelerometer (8g) is added to the model. The results are shown in Figure 4.16 and Table 4.3. The first two modes correspond to simultaneous vibrations along both the X- and Y-axes, which occurs at 55.8Hz. The third mode, corresponding to a rotation around the Z-axis occurs at 249.5Hz. Finally, the fourth mode, corresponding to vibrations along the Z-axis, occurs at a frequency of 313.3Hz. Comparing the results from the analytical model (Eq. (4.61)) with the FEA results, the error for the first two modes is 1.9%, 8.1% for the third mode and 12.9% fourth mode.

The reason why the dynamic model shows larger errors for higher modes is that it represents the CMMS as a single 6-DOF element. One solution to this issue could be to model the CMMS a multi-DOF system, with each link (i.e. parallelograms A, B, C, D and O) free to undergo 6-DOF motion. In addition, the boundary conditions of a fixed-guided beam are accurate for bending but introduce some error when the beams are twisting. However, this model is sufficient for an accurate estimate of the first three modes, which is sufficient for the design of CMMSs.

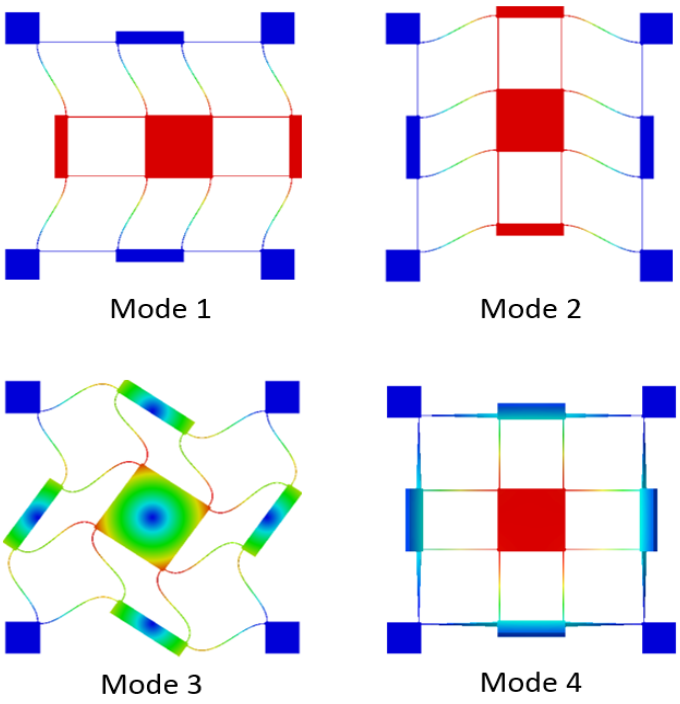

Figure 4.16 Modal analysis results from FEA

	Natural Frequencies (Hz)			
	Mode 1 (X)	**Mode 2 (Y)**	**Mode 3 (θ)**	**Mode 4 (Z)**
FEA	55.8	55.9	249.5	313.3
Analytical	54.7	54.9	269.7	353.8
Experimental	47	47	-	267

Table 4.3 Resulting resonant frequencies

4.5 Fabrication and Characterisation of an Aluminium-7075 T6 Compliant XY Stage

In order to verify the theoretical characteristics of the CMMS, a prototype is fabricated by Beihang University in Beijing, China, using WEDM and includes corners of 0.5mm radius. The dimensions and properties of the fabricated CMMS are the same than the one used in Section 4.4 and are listed in Table 4.2. To ensure a long fatigue life and reduce the actuation force, the travel range of the final design is limited to ±2.2mm. The fabricated CMMS is shown in Figure 4.17. The dimensions of the CMMS are measured using a micrometre. The dimension errors are all less than 10µm.

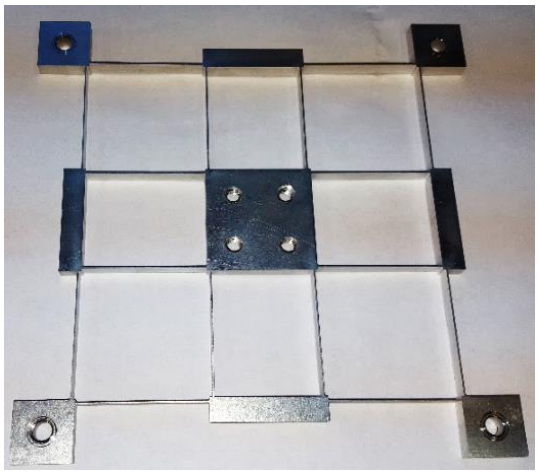

Figure 4.17 Fabricated Aluminium-7075 T6 CMMS

The MMS is driven by two VCAs from Moticont (LVCM-051-064-02) with a 12.7mm stroke, 68.2N continuous force and a force constant of 21.6N/A. They are controlled by two Ingenia Pluto Drives, allowing for a position command resolution of 1.12µm over ±2.3mm along both directions. The input displacement of the MMS is measured using two linear encoders from Renishaw (ATOM4T0-150) with a resolution of 100nm. The output displacement is measured with two capacitive sensor heads (CS1) from Micro-Epsilon with DT6110 controllers, giving a resolution of 100nm and an accuracy of

reading of 0.5µm over a range of 1mm. These sensors are mounted on a carrier and are moved along a guiding rail using two Firgelli L12-P micro linear actuators with a 10mm stroke and ±0.1mm repeatability. The assembled MMS is presented in Figure 4.18.

4.5.1 Force-Displacement Test

In order to validate the analytical model a test is carried out to establish the relationship between the input displacement and the actuation force. The input displacement along the X-axis it maintained at 0mm while it is varied from 0mm to 2mm along the Y-axis. The linear encoders are used to measure the position. As the servo drives include a built-in current sensor, the force is derived from the current using the VCA's force constant. The results are shown in Figure 4.9. The force error of the first few readings is due to the internal friction in the bearings and can be neglected.

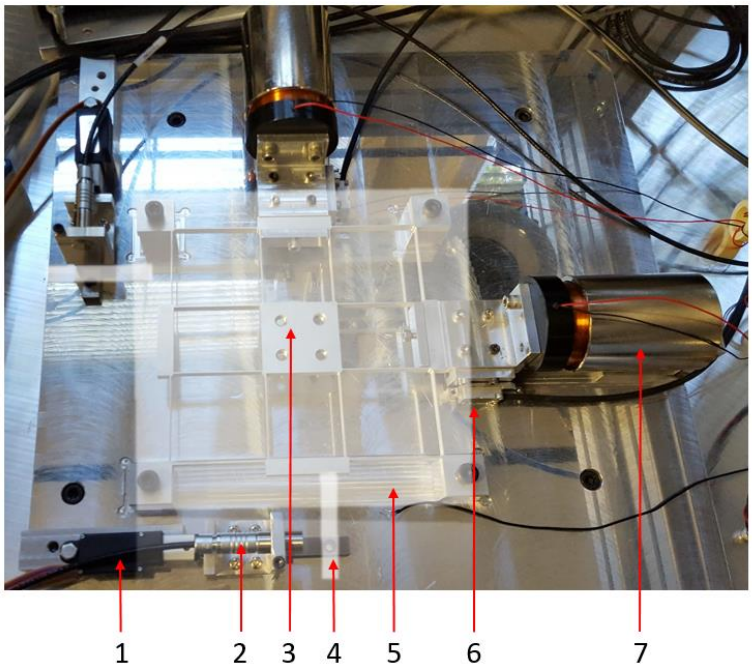

Figure 4.18 Fabricated MMS. 1) Linear actuator, 2) Capacitive sensor head, 3) CMMS, 4) Target, 5) Moving Platform 6) Linear encoder, 7) VCA

The maximum force error, occurring at 2mm, is 11.1% when compared with FEA and 3.9% when compared with the analytical model. FEA is assumed to be the most accurate prediction for an ideal system while the fabricated CMMS behaves in a slightly different way, giving the impression that the analytical model is more accurate than FEA. This can be explained by the simplifications made in the nonlinear model and by the manufacturing

and assembly tolerances affecting the fabricated CMMS meaning that both deviate from FEA.

4.5.2 Coupling Test

A coupling analysis is carried out by first applying an input displacement of 2.2mm along the Y-axis and recording the parasitic displacement along the X-axis. Following this, an input displacement of 2.2mm is applied along the X-axis and the output displacements are recorded. The maximum recorded parasitic displacement for a single direction loading (Figure 4.14) is 53μm, corresponding to an error of 18.5% when compared to FEA and 1.9% when compared to the analytical model. When loading along both directions, the difference between the input and the output displacements is 61μm along the X-axis and 65μm along the Y-axis (Figure 4.15). This corresponds to a maximum positioning error of 0.3% when compared with FEA and 0.4% when compared with the analytical model. This confirms the FEA results proving that the nonlinear model can accurately predict the displacement error caused by cross-coupling and motion loss.

The output displacement error along the X-axis caused by the cross-coupling is 53μm and the maximum lost motion recorded along the X-axis is estimated by subtracting the cross-coupling error from the total displacement error, giving a motion loss of approximately 8μm. This corresponds to a cross-coupling of less than 2.5% and a lost motion of less than 0.4%. As discussed in [106] and [155], these errors can be significantly reduced by connecting the parallelograms A and C and the parallelograms B and D together. However, this would make the design bulkier and also make the assembly of a platform to the centre of the CMMS complicated. Alternatively, the control system of the MMS will integrate the presented nonlinear model to compensate the positioning error.

4.5.3 Frequency Response

In order to obtain the frequency response of the CMMS, a testing rig is set up to generate vibrations with a hammer and measure the frequency response with a 3-axis accelerometer (ICP-T356A16) placed at the centre of the CMMS. The sensitivity of the accelerometer is 100mV/G and its output signal is processed by a Dual Channel Accelerometer Amplifier (FE-376-IPF) and acquired by a Data Acquisition card (USB-

6008) from National Instruments. Labview is used to obtain the frequency domain response using the FFT. The sampling rate is 10kHz. The testing rig setup is presented in Figure 4.19. The recorded resonant frequencies are 47Hz along the X- and Y-axes and 267Hz along the Z-axis (Table 4.3). When compared with FEA, the corresponding differences are 15.8% and 14.8% along the X- and Y-axes and the Z-axis respectively. The third mode could not be measured with the accelerometer used as it corresponds to a rotational vibration.

When comparing with the analytical model, the errors are 14.4% for the X- and Y-axes and 24.5% for the Z-axis. This error can be due to the mounts applying a small preload in the beams when being screwed. One limitation of the analytical dynamic model is its ability to predict accurately high order resonant frequencies. However, this has a limited impact on the design optimisation results and on the performances of the fabricated CMMS.

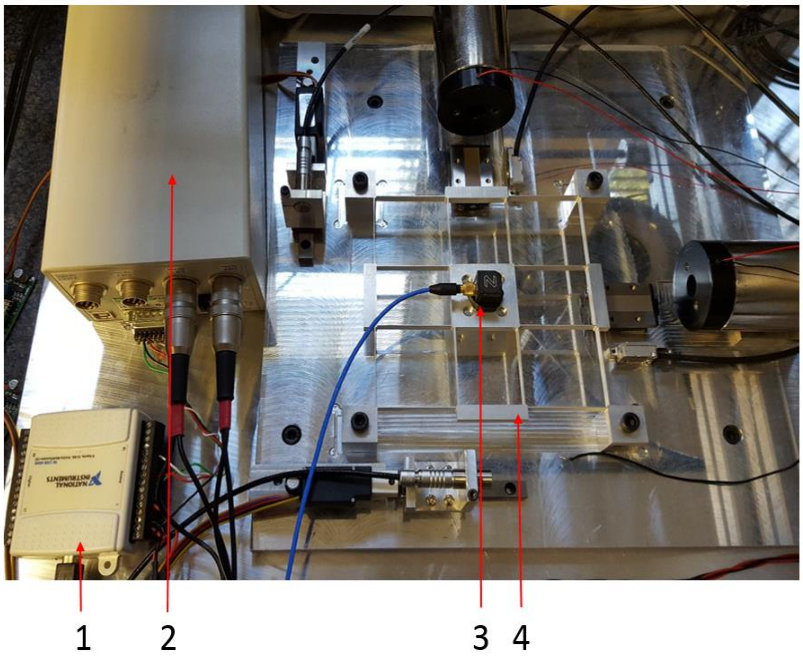

Figure 4.19 Experimental vibration test setup. 1) Data acquisition card, 2) Amplifier, 3) 3D accelerometer, 4) CMMS

4.6 Summary

In this chapter, the final design of a CMMS with a simple structure was proposed. An analytical model combining a linear and a simplified nonlinear model was presented. The combination of these two models was implemented in MATLAB to fully characterise and

optimise CMMSs. From this model, a CMMS was developed. The results from FEA and experimental testing clearly show that the analytical model is an accurate characterisation of the behaviour of the CMMS in terms of stiffness and working range, taking into account limitations such as nonlinear buckling and stress. Furthermore, its ability to accurately predict the output displacement as a function of the input displacement makes it suitable for position control without necessarily needing a feedback loop. This model can be easily adapted to any CMMS composed of basic compound parallelogram structures symmetrically arranged and using leaf-spring flexures. The computation time required to perform design optimisation was within 140 seconds. The designed CMMS has a cross-coupling of less than 2.5% for a travel range of $\pm 2.2 mm^2$ and a theoretical ratio between the first two and the third resonant frequency larger than 1:4.

Chapter 5 Implementation and Testing of a Dual-Range Manipulator Using the Fabricated Compliant Micro-Motion XY Stage

In this chapter, the CMMSs fabricated in Chapter 3 and Chapter 4 are assembled with actuation and sensing systems, thus resulting in an operational MMS. Combining high accuracy and large workspace implies expensive metrology such as ultra-high resolution/large range sensors and actuators. The aim of this work is to use the concept of dual-range manipulation to achieve a positioning accuracy of a few micrometres within a workspace of a few millimetres while keeping the cost as low as possible. The concept of dual-range manipulation is to use two sets of actuators and/or sensors within the same system. The first set allows for positioning in a large workspace but has a low positioning accuracy. The second set covers a smaller workspace, just enough to compensate the positioning error of the coarse mechanism and has a high positioning accuracy. The main advantage of dual-range manipulation is the cost reduction. It also avoids the need for complex calibration, tight manufacturing and assembly tolerances.

5.1 First Prototype Using the Initial Design of the Compliant Stage

Firstly, the Nylon-66 CMMS is used for a prototype. The MMS includes CNC machined parts for assembly of the CMMS, sensors and actuators. Because of the low stiffness of Nylon-66, guiding rails are used to allow for a decoupled motion along X and Y while avoiding a Z translation and unwanted rotation. The MMS is driven by two VCAs from Moticont (LVCM-051-064-02) with a 12.7mm stroke and 68.2N maximum continuous force. They are controlled by two Ingenia Pluto Drives, allowing for a position command resolution of 1.46µm over ±3mm along both directions. The input displacement of the MMS is measured using two linear encoders from Renishaw (ATOM4T0-150) with a resolution of 100nm and an accuracy of reading of ±5µm. The first fabricated MMS is presented in Figure 5.1.

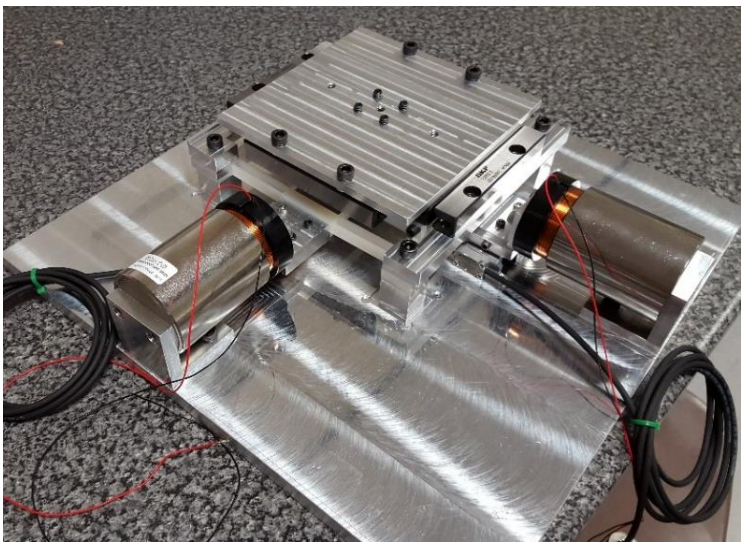

Figure 5.1 First prototype of the MMS

5.1.1 Open-Loop Behaviour

The open-loop behaviour of the MMS is measured using a coordinate measurement machine (CMM) (C.E. Johansson Cordimet 701) with a Renishaw probe (PH10T PLUS) which has a measured repeatability of 0.1µm. The input displacements along the X and the Y directions are controlled with LABVIEW 2014 through a Labjack U6 Pro data acquisition card. The output displacements are recorded using the CMM. The test rig is shown in Figure 5.2.

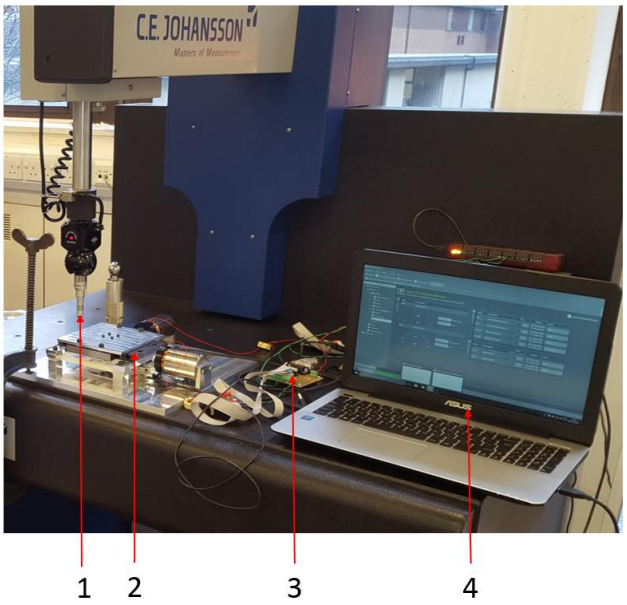

Figure 5.2 CMM test rig with 1) Probe, 2) MMS, 3) Control electronics, 4) Control software

To begin with, a single direction displacement test is carried out in a range of -2.5mm to 2.5mm along X for both positive and negative directions. The results are shown in Figure 5.3, Test 1. The maximum error between the position command and the actual position of the platform is 39µm. Since the error appears to be proportional to the input displacement, a correction factor is applied to the control program. The results from Figure 5.3, Test 2 show that the maximum error is reduced to 13µm. However, it is observed that when this correction factor is applied to the Y direction, the error increases. Hence, the CMMS presents some anisotropic behaviour.

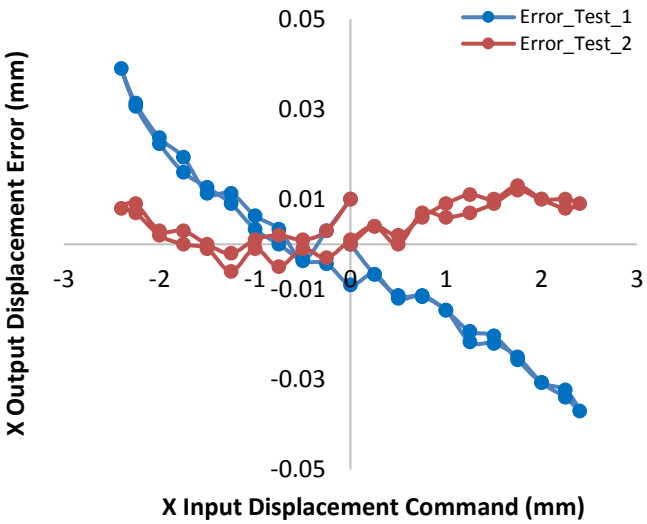

Figure 5.3 CMM measurements for a single direction loading

A coupling analysis is then carried out. An input displacement of 2mm is first applied along the Y direction and is then gradually applied along the X direction. The results are presented in Figure 5.4. The first observation made is that the results are in accordance with FEA, where the error is less than 3µm for 2mm input displacement. The second observation is that the maximum recorded parasitic displacement is 50µm.

To finish with, a bidirectional test is carried out. It consists in moving the MMS randomly along both directions to cover a square of $5\times5mm^2$ within the $6\times6mm^2$ workspace. The input displacement values are between -2.5mm and 2.5mm. The maximum recorded positioning error is 109µm.

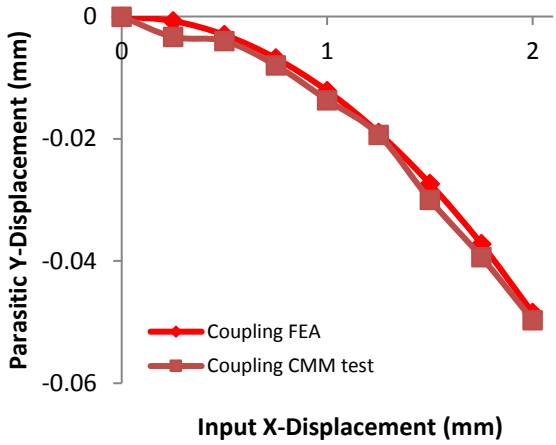

Figure 5.4 CMM measurements of the parasitic displacement compared with FEA

5.1.2 Dual-Range Positioning

The observations made from the open-loop tests show that there is a coupling between the two axes of motion that cannot be predicted when moving the MMS along both directions simultaneously. In addition, for the same input displacement, the positioning error is not the same along the two directions. Finally, since the mechanical properties of the MMS are affected by the environmental conditions, the positioning error varies with time.

To compensate for this positioning error, a set of high resolution sensors is added to the system in order to directly measure the output displacement of the MMS. These sensors are mounted on a carrier and are moved along a guiding rail using two Firgelli L12-P micro linear Actuators with a 10mm stroke and ±0.1mm repeatability. The hybrid positioning procedure for each direction of motion is as follows:

i. The MMS is moved to its desired position in open-loop mode (coarse positioning)
ii. The positioning error is measured using an external system (CMM)
iii. The high resolution sensors are moved close to the moving platform and the relative position is recorded and used as the initial position for the next step
iv. The MMS is moved by the positioning error measured in closed-loop mode using the feedback from the high resolution sensors (fine positioning)

5.1.2.1 Sensor Selection

The choice of high resolution sensor is critical and involves a trade-off between the cost of the system and the measuring accuracy. Table 5.1 presents a qualitative analysis of the four types of sensors considered for this application based on quotations from RENISHAW®, KEYENCE Ltd. and MICRO-EPSILON Ltd. The most suitable solution in terms of this trade-off is the capacitive sensor. Therefore, the sensors used to measure the open-loop behaviour of the MMS in Chapter 4 are reused for the closed-loop control of the fine positioning, along with the linear actuators. Figure 5.5 shows an exploded view of the MMS. The control electronics diagram is shown in Figure 5.6.

Sensor	Accuracy	Sensing Range	Cost	Environmental Sensitivity
Capacitive	++	-	+	+
Interferometer	++	+	--	-
Eddy current	+	--	-	++
LVDT	-	++	++	++

Table 5.1 Sensors rating

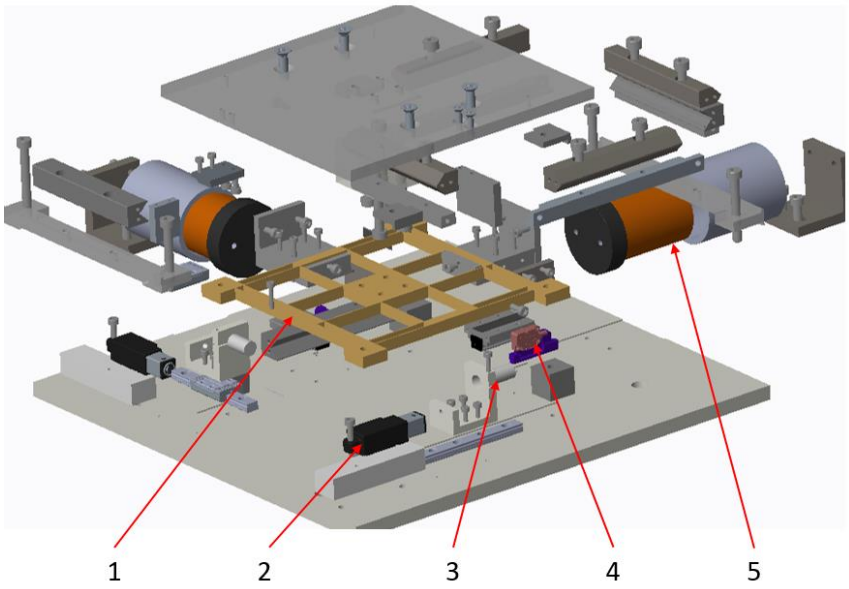

Figure 5.5 Exploded view of the dual-range MMS with 1) CMMS, 2) Linear actuator, 3) Capacitive sensor head, 4) Linear encoder, 5) VCA

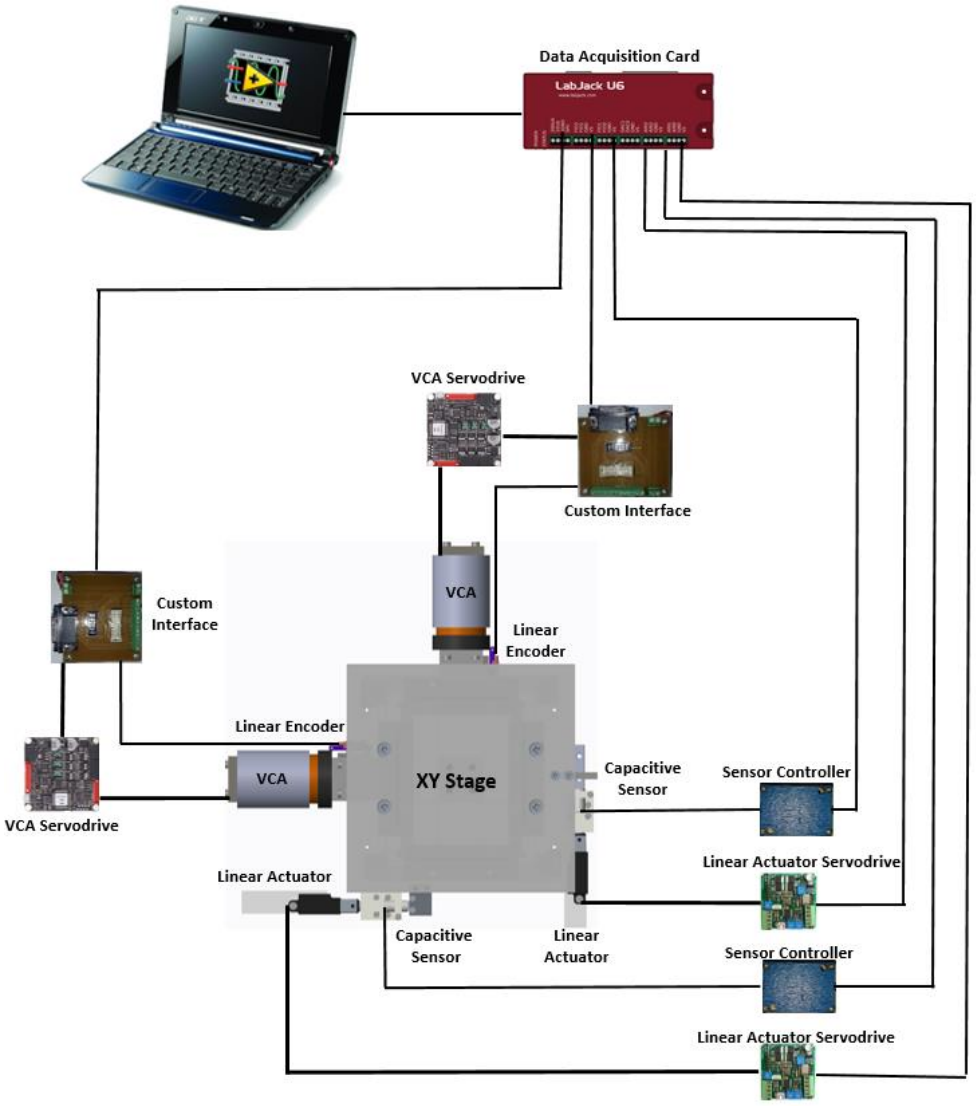

Figure 5.6 Control system of the dual-range MMS

5.1.2.2 Testing

The positioning accuracy test is inspired by the ISO standard 9283:1998, and the CMM is used to measure both coarse and fine positioning errors. The MMS is driven between four points, each located at the corner of a $5\times5mm^2$ square within the workspace of the MMS (Figure 5.7). The hybrid positioning procedure previously presented is applied to move the MMS between each point, starting from point P1, followed by P2, P3 and finally P4. This sequence is carried out 10 times and the position of the MMS is recorded at each pose.

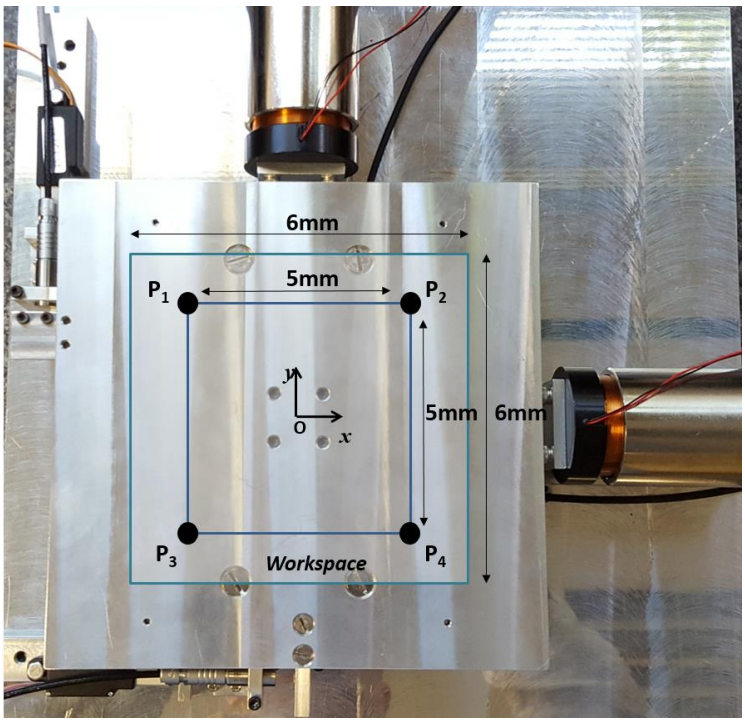

Figure 5.7 Measuring points of the MMS within the workspace (scaled up)

The accuracy measured for point P1 is given by:

$$AC\_P_1 = \sqrt{(\bar{x}_1 - x_{1c})^2 + (\bar{y}_1 - y_{1c})^2} \tag{5.1}$$

where x_{1c} and y_{1c} are the position commands along the X- and Y-axes respectively, $\bar{x}_1$ is the coordinate along X of the barycentre of the cluster of 10 points located at P1:

$$\bar{x}_1 = \frac{1}{10}\sum_{i=1}^{10} x_{1i} \tag{5.2}$$

and $\bar{y}_1$ is the coordinate along Y of the barycentre of the cluster of 10 points located at P1:

$$\bar{y}_1 = \frac{1}{10}\sum_{i=1}^{10} y_{1i} \tag{5.3}$$

The pose accuracy at points P2, P3 and P4 are calculated the same way as P1, using Eq. (5.1) and the results are shown in Table 5.2.

The repeatability measured for point P1 is given by :

$$R\_P_1 = \bar{l}_1 + 3\sigma_1 \tag{5.4}$$

where $\bar{l}_1$ is the average error of the cluster of poses attained for point P1:

$$\bar{l}_1 = \frac{1}{10}\sum_{i=1}^{10} l_{1i}$$

with:

$$l_{1i} = \sqrt{(x_{1i} - \overline{x}_1)^2 + \left(y_{1i} - \overline{y}_1\right)^2} \tag{5.5}$$

and σ_1 is the standard deviation of the cluster of poses attained for point P1:

$$\sigma_1 = \sqrt{\frac{\sum_{i=1}^{10}(l_{1i} - \bar{l}_1)^2}{9}} \tag{5.6}$$

The repeatability at points P2, P3 and P4 are calculated the same way as P1, using Eq. (5.4) and the results are shown in Table 5.2.

	Point P1		**Point P2**		**Point P3**		**Point P4**	
	X (μm)	**Y (μm)**	**X (μm)**	**Y (μm)**	**X (μm)**	**Y (μm)**	**X (μm)**	**Y (μm)**
Mean Error (mm)	**1.9**	**3.5**	**1**	**2.3**	**2.7**	**2.1**	**1.7**	**2.7**
Absolute mean Error (mm)	**4**		**2.5**		**3.4**		**3.2**	
Repeatability at 3σ (mm)	**3.1**		**3**		**3.6**		**2.7**	

Table 5.2 Accuracy and repeatability of the Nylon-66 MMS

The overall accuracy is calculated by using the positioning error of all the attained poses, regardless of the position command, using Eq (5.4). The overall accuracy is therefore 5.1μm. Several sources of error can be identified. Firstly, the resolution of the motor controllers is this configuration is only 1.46μm. Also, the points measured are located at ±2.5mm along each axis, where then nonlinear characteristics of the CMMS become significantly high and cause some small oscillations in the system's steady-state response. Finally, the measuring uncertainties of the CMM can become significant at such a small scale.

5.2 Second Prototype Using the Final Design of the Compliant Stage

Following the promising results from the prototype shown in Section 5.1, a dual-range MMS is fabricated using the Aluminium-7075 T6 CMMS from Chapter 4. The assembled MMS is presented in Figure 5.8. It consists of a platform directly fixed to the centre of the CMMS. Two small plates are mounted on the platform and are used as a target to measure the output displacement of the MMS. The total moving mass is approximately 1kg.

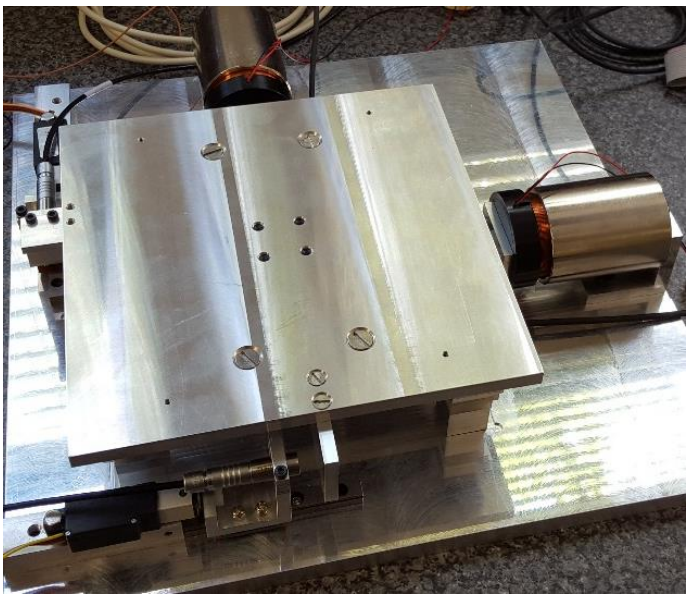

Figure 5.8 Fabricated dual-range MMS

5.2.1 Input Position Control

The input position control of the MMS controls the linear displacement of the VCAs with a Proportion-Integral-Derivative (PID) loop using the two linear encoders as feedback.

The input displacements along the X and the Y directions are controlled with LABVIEW 2014 through the analogue outputs of a Labjack U6 Pro data acquisition card. To begin with, a single direction displacement test is carried out over a range of 0mm to 2.2mm along Y. The results show that the maximum difference between the input and the output displacement is 4µm and that the parasitic translation along the transverse direction is 53µm (Figure 4.14), corresponding to a coupling of 2.4%.

A bi-directional loading test is then carried out. The input displacement of 2.2mm previously applied along the Y direction is maintained and an input displacement of 2.2mm is gradually applied along the X direction. The results are presented in Figure 4.15. The first observation made is that the results are in accordance with FEA, where the maximum error is less than 3µm for 2.2mm input displacement. The second observation is that the maximum recorded parasitic displacement is 53µm.

5.2.2 Dual-Range Positioning

The observations made from the input position control test show that there is a coupling between the two axes of motion that cannot be predicted when moving the MMS along both directions simultaneously. There is also a difference between the input and the output displacement of up to 4µm. To compensate for this positioning error, a set of high resolution sensors is added to the system in order to directly measure the output displacement of the MMS.

A second PID loop is added to control the output displacement of the MMS using the readings from the high resolution sensors. The simplified plant model is presented in Figure 5.9. The gains are automatically tuned by the controllers and will not be detailed.

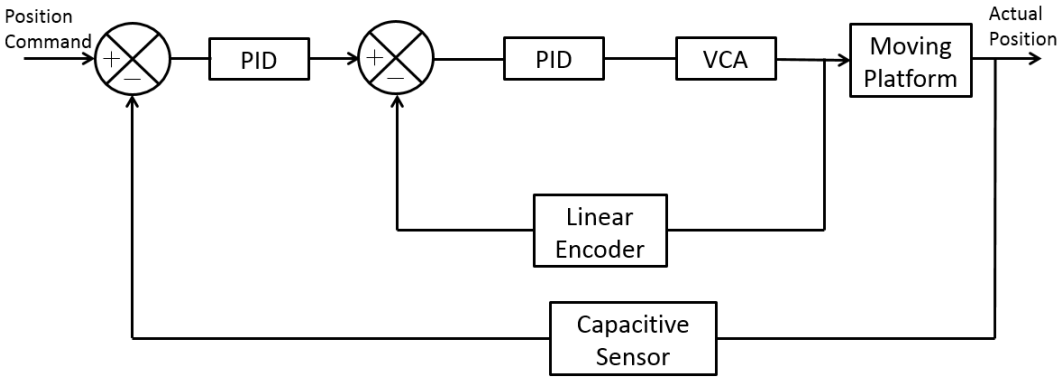

Figure 5.9 Fine positioning control loop for the MMS

The external system used to measure the positioning error depends on the system in which the MMS is integrated. This choice is up to the user. For instance, a high resolution vision system can be used to measure the position of the moving platform on which a calibration grid is placed. A CMM was used for the first prototype but this solution is only suitable for testing purposes.

Since the capacitive sensors directly measure the position of the MMS, they are used to estimate the relative positioning accuracy. It is assumed that due to the nonlinear stiffness of the CMMS, the force disturbance is higher for large displacements. Therefore, a test is carried out for an input displacement of 0mm along both directions and then for 2.2mm along both directions. The sensors' readings are recorded for a period of 20 seconds in fine positioning mode and the accuracy is estimated from the maximum amplitude of oscillation once the steady-state is reached. Figure 5.10a) and b) show the steady-state response along both directions for 0mm loading. It can be clearly seen that

the maximum amplitude of oscillation is smaller than ±0.5µm which is beyond the reading accuracy of the capacitive sensors. Figure 5.10c) and d) show the steady-state response for 2.2mm bidirectional loading. The amplitude of oscillation increases and reaches ±2µm. This oscillation is due to the nonlinearities arising from the CMMS. Additionally, the resolution of the analogue to digital converter (ADC) used to read the position command sent by the data acquisition card is only 12-bits. This corresponds to an incremental position resolution of 1.12µm. Controllers with a higher resolution would allow for a higher positioning accuracy.

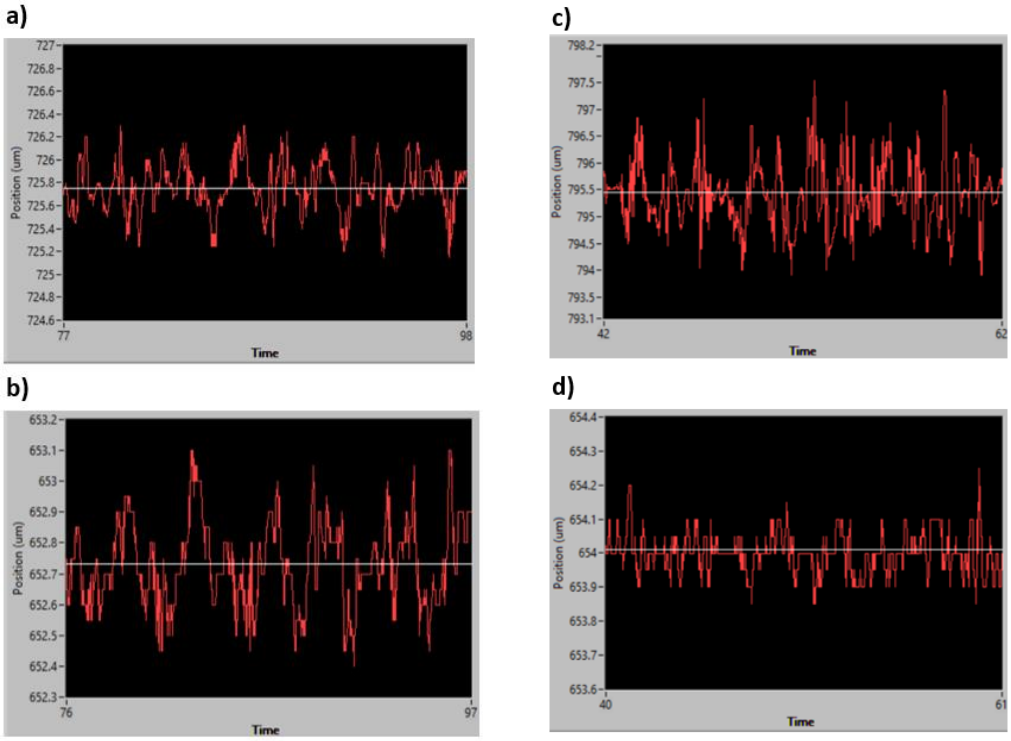

Figure 5.10 Capacitive sensors readings in fine positioning mode along a) the X-axis at position 0mm, b) the Y-axis at position 0mm, c) the X-axis at position 2.2mm, d) the Y-axis at position 2.2mm

5.3 Summary

A first prototype of a dual-range MMS was fabricated using a Nylon-66 CMMS. The high sensitivity to temperature and humidity of the CMMS and the coupling between the two axes of motion engendered positioning errors of up to 109µm in coarse positioning mode. The concept of dual-range manipulation was therefore introduced using capacitive sensors for the fine positioning. A series of pose accuracy tests were carried out using a CMM and the average positioning accuracy was 5.1µm.

A second MMS was made including an Aluminium 7075-T6 CMMS, with a travel range of $\pm 2.2 \times 2.2 mm^2$ and a coupling of 2.4%. The maximum displacement error of the MMS measured in coarse positioning mode was 67μm. The relative positioning accuracy was reduced to less than ±2μm in the worst-case scenario due to the dual-range positioning method. This error can be further reduced by using higher resolution motor controllers and sensors. Therefore, there is a great potential for compact, low-cost and high accuracy micro-motion using dual-range positioning.

Chapter 6Hybrid Manipulator

Assembly systems assembling parts at the meso scale with a micro scale accuracy are widely available for small batch to mass production applications. However, the systems dedicated to prototyping applications are costly and not always compact. The concept of hybrid manipulation is therefore introduced to design an assembly system, combining a conventional pick-and-place manipulator, the dual-range MMS designed in Chapter 5 and a high resolution vision system. It is designed to be integrated with a micro factory for prototyping of mobile phone cameras and sensors. The hybrid manipulator is first presented, starting with the pick-and-place manipulator, continuing with the MMS and finishing with the vision system and the image processing functions programmed to allow for a fully automated assembly. The calibration of the hardware and the vision system is then presented. Finally, the assembly procedure is detailed and the performances of the system are evaluated. This includes an estimate of the measuring uncertainty of the vision system and the overall positioning accuracy of the assembly system. The introduction of hybrid manipulation within the assembly system and within the MMS is proven to be a reliable way to achieve compact, low-cost high accuracy. Unlike most of the other systems presented in the literature, this system combines micro-assembly systems technologies with existing micro-factory solutions. The resulting system performances are very promising considering the cost. Additionally, the vision system uses a single camera for both part detection and visual servoing.

6.1 Pick-and-Place Manipulator

A robot manipulator is used as the coarse mechanism of the hybrid system to pick and place the miniaturised parts. Such a system is characterised by its mobility, working range, speed, accuracy and stiffness. The assembly process of small devices usually requires four DOFs, three translations and one rotation. In this application, the orientation is not critical as the maximum error tolerance is ±1° about the Z-axis (θ). Since the parts are stacked on top of each other, the accuracy required along the Z-axis is not critical either. However, some compliance of the end-effector will be used to avoid damaging the parts. Future work will include force measurement.

The manipulator used is a custom Gantry system from Igus driven by stepper motors from Nanotec (Figure 6.1). The X- and Y-axes are belt driven to allow for fast and large

motion while the Z-axis is screw driven to allow for slow, smooth and more precise motion. The rotation about the Z-axis (θ) is driven by a stepper motor. The resulting workspace of the manipulator is 290×240×20mm^3. The characteristics of each of the four axes of motion are listed in Table 6.1. From this table, the positioning error of the X- and Y-axes is estimated to be less than ±1mm, which will be used as a design constraint for the fine positioning mechanism.

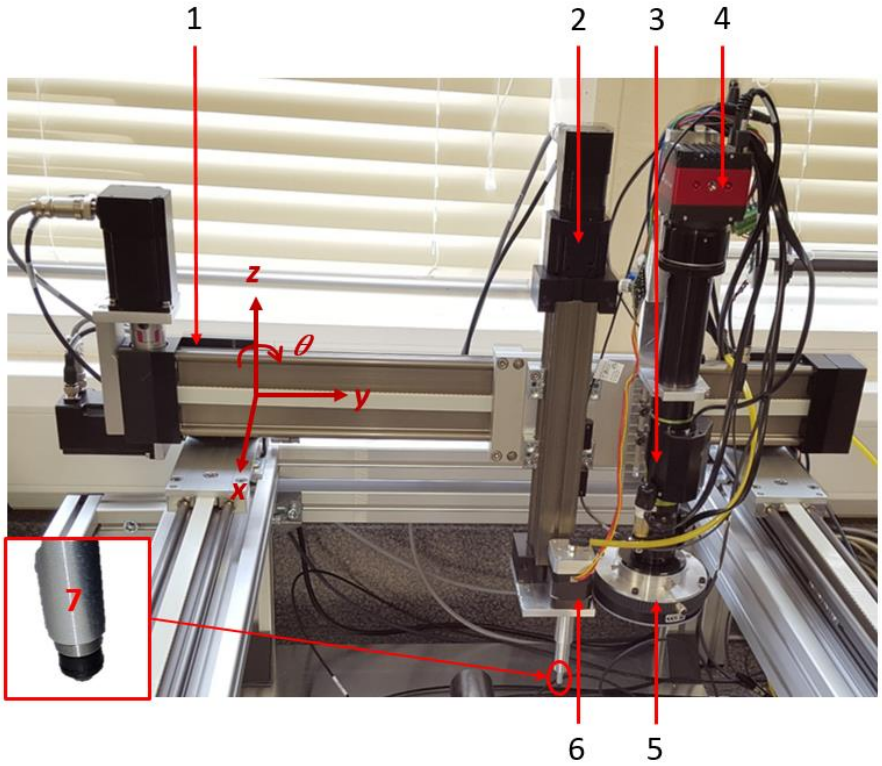

Figure 6.1 Pick-and-place manipulator: 1-X and Y belt drives, 2-Z screw drive, 3-Motorised lens/focus system, 4-Camera, 5-Ring light, 6-θ drive, 7-Picker head

To ease the manipulation, a vacuum gripper is chosen over a mechanical gripper. It consists of a hollow cylinder coupled to the θ-axis hollow motor shaft on the top end. A rubber tip holder from Micro-Mechanics is attached to the bottom end. The rubber tip can easily be exchanged with tips of sizes between 0.5mm and 2mm and with round or square shapes. Vacuum is generated by a mini rotary vane pump from Gardner Denver Thomas GmbH (G12/04512). The compliance of the rubber tip allows for a compression greater than 1mm while the position error of the Z drive is approximately ±0.1mm. The full hybrid manipulator is presented in Figure 6.2.

Axis	Drive Type	Drive Repeatability (Manufacturer)	Motor Type	Drive Position Resolution	Controllers	Position Command Resolution
X	Belt	±0.3mm	Nanotec NEMA23	0.14mm	Nanotec C5-E	0.57mm
Y	Belt	±0.3mm	Nanotec NEMA23	0.14mm	Nanotec C5-E	0.47mm
Z	Screw	±0.1mm	Nanotec NEMA17	0.004mm	Ingenia Hydra	0.053mm
θ	Motor	-	Nanotec NEMA17	0.225°	Nanotec SMC11	0.225°

Table 6.1 Gantry drives specifications

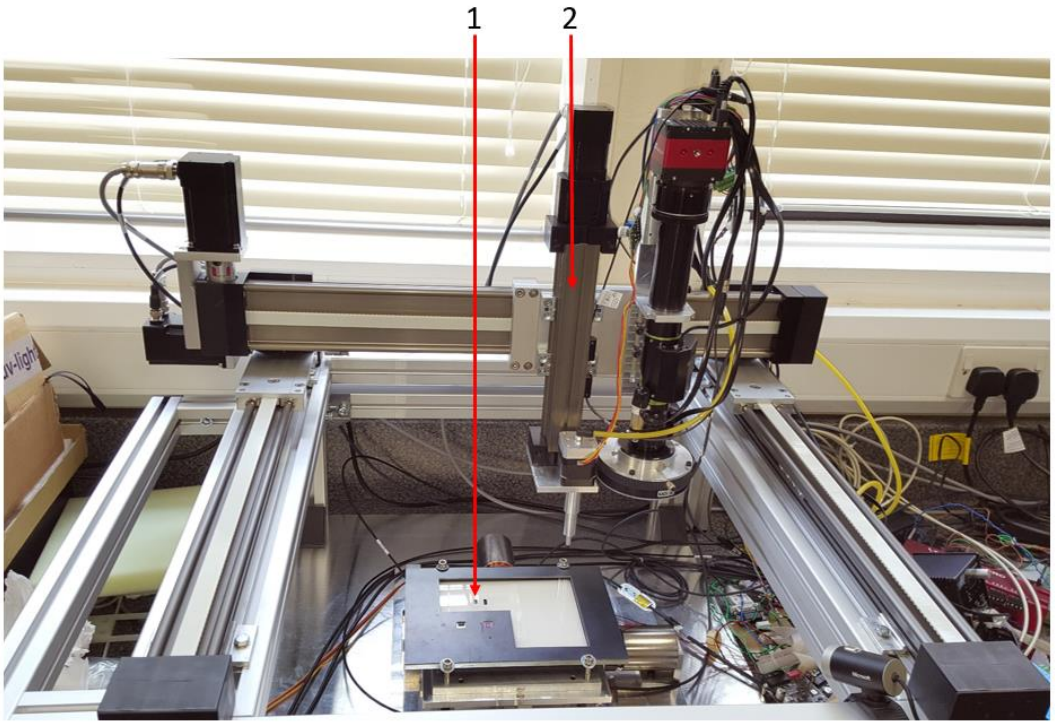

Figure 6.2 Hybrid miniaturised products assembly system: 1-Fine positioning mechanism, 2-Coarse positioning mechanism

6.2 Vision System

6.2.1 Strategy

In the majority of existing assembly systems, a vision system is used to either measure the position and orientation of the parts or for visual servoing. In some cases, the parts are placed randomly on the substrate and the vision system is only used to locate the parts prior to the assembly. The manipulator then picks the parts and places them to the desired location. This implies using a single manipulator with a high positioning accuracy. In other cases, the vision system is used to monitor the position of the parts in real time as

in [204, 205]. This solution is not optimal for the current configuration of the hybrid manipulator as the camera must be placed over the gripper or at least two cameras should be used.

Recent work on micro-manipulation investigated the use of a vision system to measure the position of a moving substrate in one or two dimensions. For instance, [206] implemented a vision-based measurement system which can measure the position of a moving platform using an organic light emitting diode (OLED) substrate, achieving a measuring accuracy of 1.2µm. [207] implemented a similar method but used a micrometre calibration slide, achieving a positioning resolution of 0.04µm. Another vision-based measurement system was developed in [208, 209] to measure the position of a MMS, using a pseudo-periodic encoded pattern. The accuracy achieved is 3.5µm. Other pattern-based visual servoing systems were implemented in [210] and [211]. The system from [212] was used to track a pattern on a moving substrate to calibrate the MMS and verify the positioning accuracy.

Although, in this application, the vision system cannot directly measure the relative position between the part and the target location, it is possible to achieve an accurate positioning by dividing the process in two steps. First, the camera is used to locate the part on the substrate. Then the camera is used to locate the gripper above the substrate.

The camera is attached to the Y-axis carriage of the pick-and-place manipulator and is used to locate the parts on the substrate. The vision system is composed of a 28.8MPixel camera (Figure 6.1) from Allied Vision (Prosilica GT6600), a lens with motorised 7:1 zoom and focus from Qioptiq and a ring light from CCS (PD3-5024-3-ET). This configuration allows for an image resolution from 4.11µm/pixel for a field of view (FOV) of $18\times27mm^2$ down to 0.61µm/pixel for a FOV of $2.6\times4mm^2$. The image acquisition and processing is carried out by Sherlock© and runs on a GEVA1000 controller from Teledyne Dalsa.

A calibration grid (Figure 6.3) from PYSER-SGI (PGR200) is used as the assembly substrate on which the parts are placed prior to assembly. The grid is a glass plate on which $10\times10mm^2$ squares have been marked.

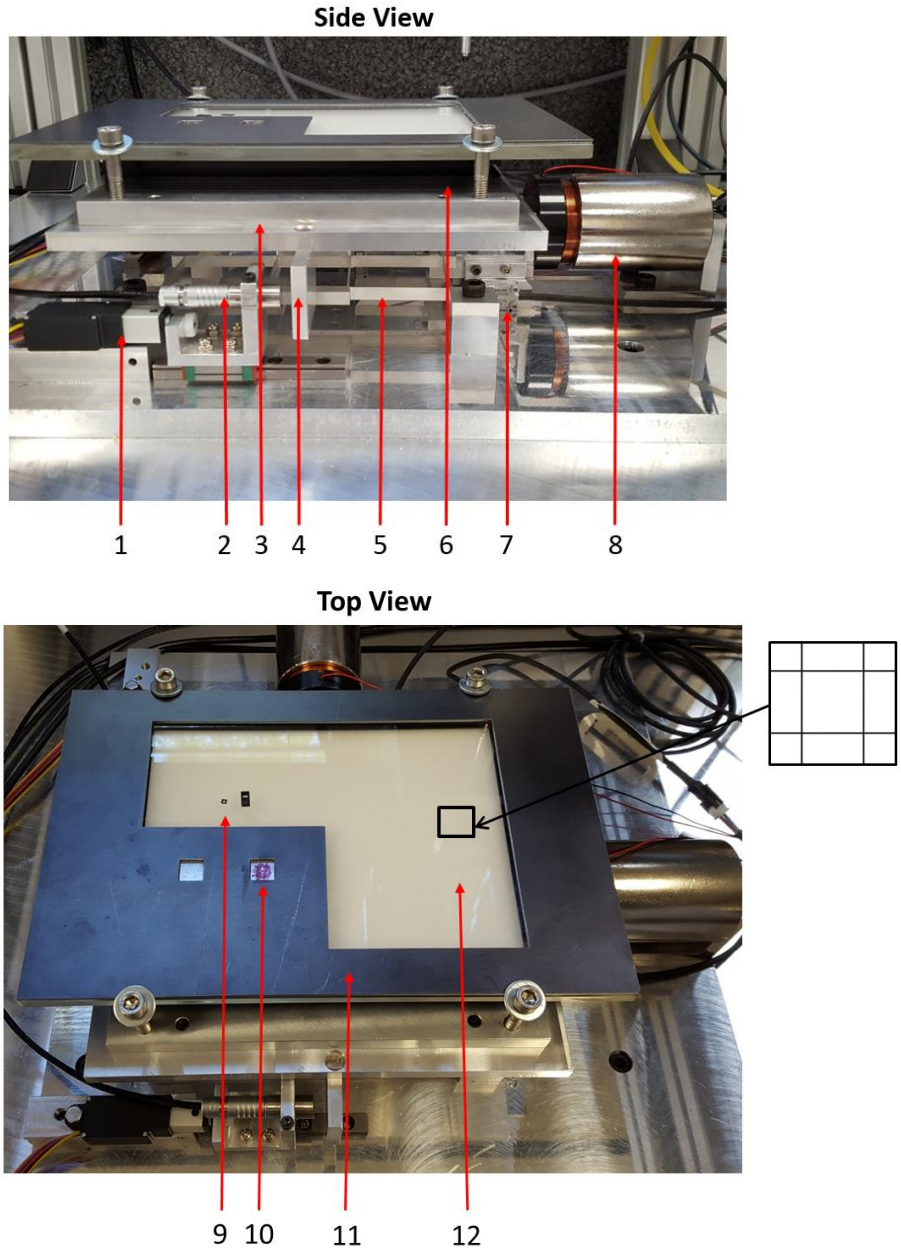

Figure 6.3 Fabricated MMS with assembly substrate: 1-Linear actuator, 2-Capacitive sensor head, 3-Moving Platform, 4-Target, 5-CMMS, 6-Backlight, 7-Linear encoder, 8-VCA, 9-Parts to assemble, 10-Assembly area with tape, 11-Mask, 12-Grid

The lines have a thickness of 8µm, a straightness of 2µm and the distance between each line is known with an accuracy of 1.5µm which is compliant with the United Kingdom Accreditation Service (UKAS) certification. The grid is used as a reference to locate the position and orientation of the parts on the substrate and to locate the position of the manipulator above the substrate. It is placed on the top of a backlight from CCS (TH2-160/120-SW-PM) for optimal illumination.

To hold the first assembled parts in position, plastic paraffin film is stuck underneath a laser-cut steel mask, which is placed on the top of the substrate (Figure 6.3). Taking into account the offset between the nozzle and the camera and the 10mm clearance required between the grid lines and the edges of the mask, the resulting workspace of the whole system is $20\times50mm^2$, which corresponds to 10 squares in which a part can be placed.

The vision system is programmed to execute two functions: measure the location of the camera relative to the grid and measure the location and orientation of a part inside a grid square.

6.2.2 Camera Location

The first function of the vision system is to measure the position of the coarse manipulator relative to the MMS. This is achieved by measuring the distance between the centre of the image and the bottom and left lines of the grid square which are used as origins for the X- and Y-axes respectively (Figure 6.4). The line detection is achieved by detecting two points on each of the X and Y grid lines and by drawing a line between these two points on the image. The points are detected using a dark-to-light edge detection algorithm.

6.2.3 Part Location

The second function of the vision system is to measure the position and orientation of the part relative to the grid square. The location of the part on the image is obtained using a pattern recognition algorithm available with Sherlock©. The lines are then detected in the same way than for the camera location function. Finally, the relative distance between the centre of the part and the two reference lines is measured.

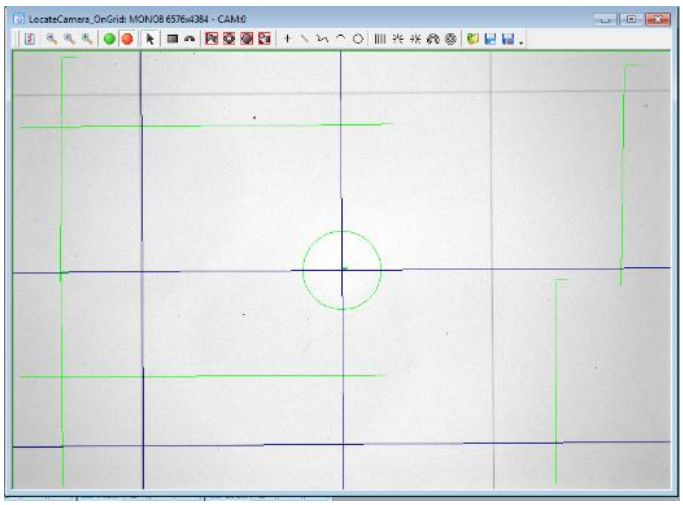

Figure 6.4 Vision system's line detection function

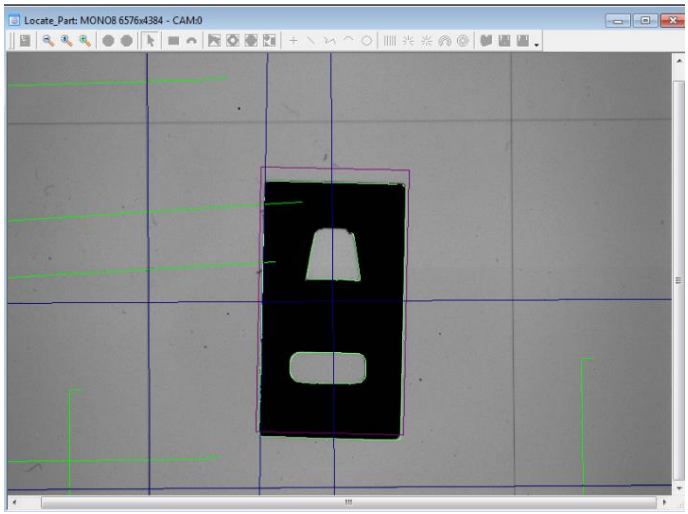

Figure 6.5 Vision system's part location function

6.3 Control System

The control system of the hybrid manipulator is organised in several modules which are programmed independently and synchronised under the supervision of a master program. Figure 6.6 shows a high-level diagram of the setup. The grey area at the centre represents the main program with the independent modules. This is the "brain" of the system and it is used to coordinate the automatic assembly sequence. It also includes the graphical user interface. The control of the entire system is realised using LabView. Seven Virtual Instrument (VI) libraries are created to control and communicate with the subsystems via two Labjack U6-Pro data acquisition cards and through two RS232 ports. The red area represents the controllers for the actuators and sensors. All the controllers

run a standalone program which is used to move the actuators based on the command sent by the Labview program. Finally, the blue layer represents the actuators and sensors. A power supply is used to supply either 12V or 24V to all the elements in the red zone.

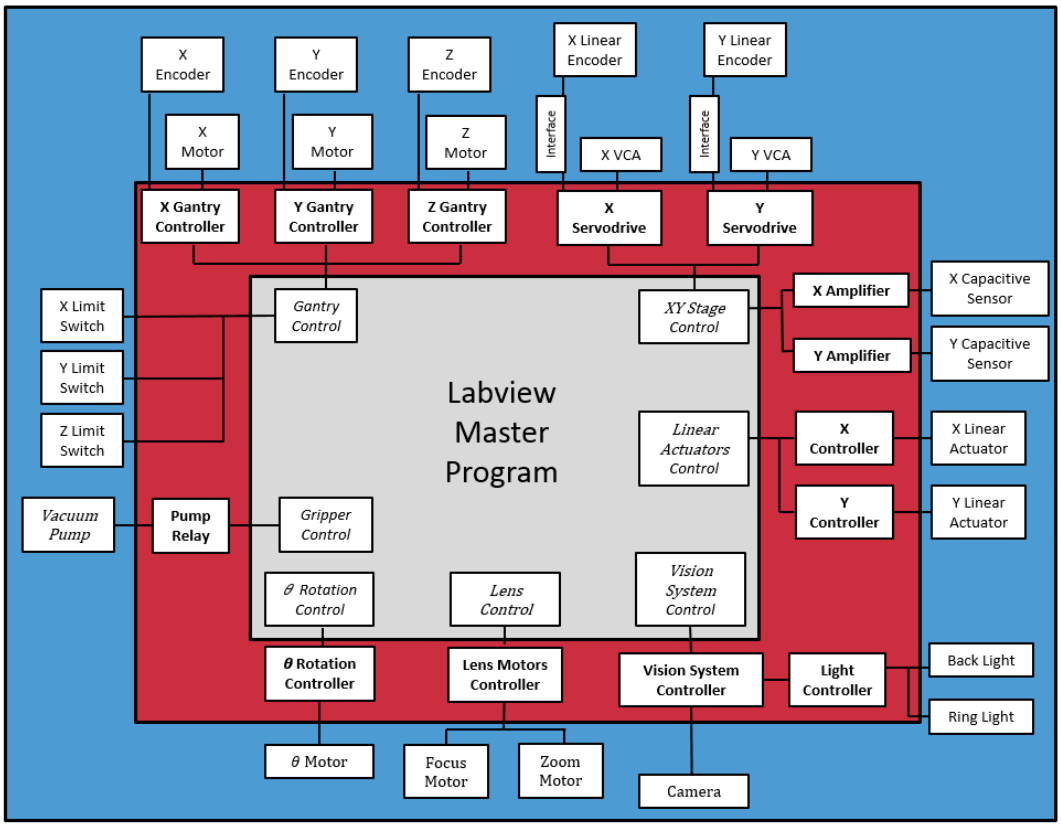

Figure 6.6 Control System of the hybrid manipulator

6.4 Calibration

Although the MMS can allow for a positioning accuracy better than ±2μm along the X- and Y-axes, the overall accuracy mainly relies on an appropriate calibration. This section presents the calibration of the vision system followed by the calibration of the gripper position offset.

6.4.1 Vision System Calibration

Firstly, the vision system is calibrated to obtain the true image resolution using the substrate as a calibration grid. The zoom is kept constant at approximately 27% (i.e. 1.9×) so that the image can fit a $10\times10mm^2$ square (Figure 6.7(a)). The focus is adjusted using a focus quality check algorithm available with Sherlock©. The calibration routine

programmed detects the lines and creates a point at each of the four line intersections. Because the camera and the calibration grid are not perfectly parallel to each other, the line angle measured on the image must be included in the calibration, so that only absolute distances are used (Figure 6.7(b)).

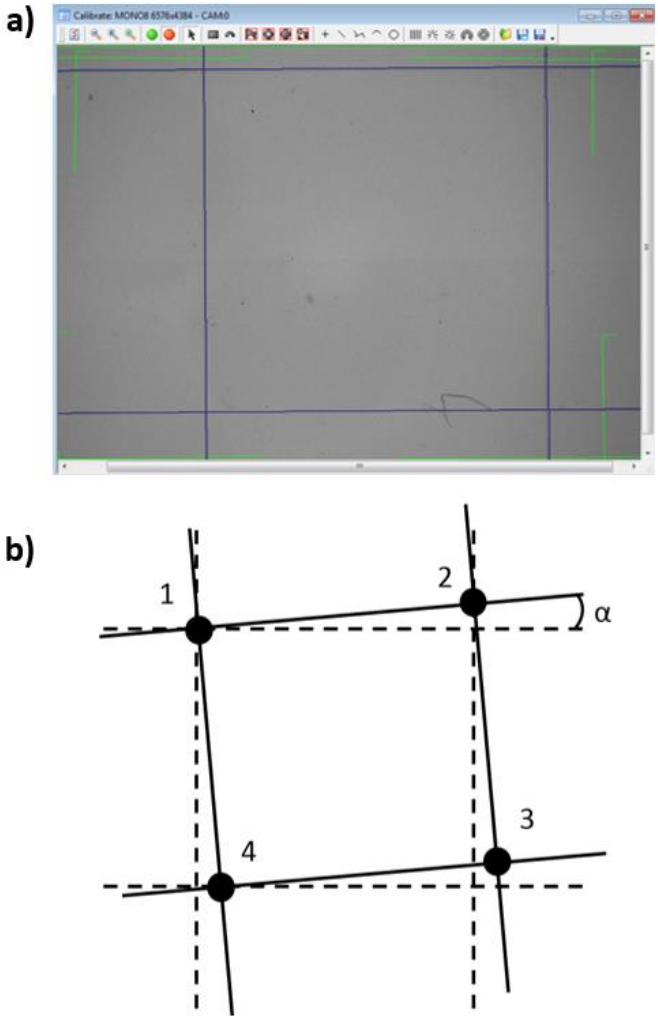

Figure 6.7 Calibration of the vision system: a) Line detection of one square on the grid and b) Coordinates determination of the points

The coordinates of these intersection points are then converted from pixels to millimetres using the following equation:

$$\begin{cases} Point\ 1: (0, 0) \\ Point\ 2: \left(10\cos\alpha\ ,\ 10\sin\alpha\right) \\ Point\ 3: \left(10\left(\cos\alpha + \sin\alpha\right)\ ,\ 10\left(\sin\alpha - \cos\alpha\right)\right) \\ Point\ 4: \left(10\sin\alpha\ ,\ -10\cos\alpha\right) \end{cases} \tag{6.1}$$

The angle measured between the substrate and the camera is around 0.4°. Ignoring this angle could create a reading error of 70μm over 10mm, corresponding to a change in resolution of 0.02μm/pixel.

To verify the reliability of the vision system calibration, a calibration grid made of $1\times1mm^2$ squares is used to measure two distances (Figure 6.8). The error is 4μm over 1mm and 4μm over 5mm. These errors are due the reading uncertainties of the vision system and will be discussed in Section 4.1. However, the calibration is proven to be accurate as the error is not proportional to the measured distance. The gains and gamma corrections used to process the image are adjusted manually and will not be discussed in the thesis.

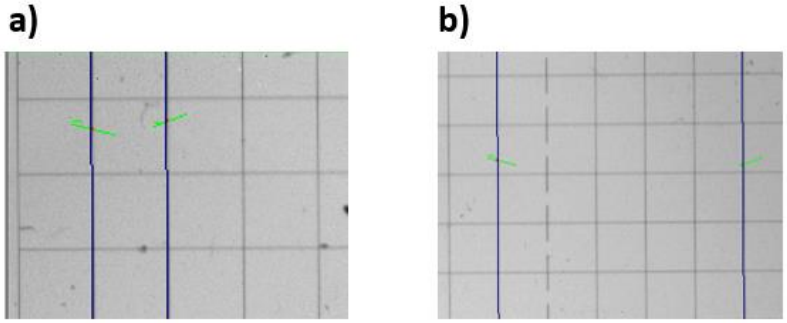

Figure 6.8 Calibration verification: a) 1mm distance and b) 5mm distance

6.4.2 Gripper Offset

The theoretical distance between the gripper tip and the camera is 20mm and 90mm along the X- and Y-axes respectively. However, because of the error induced by manufacturing and assembly tolerances, the exact offset needs to be measured. The process for the offset measurement is shown in Figure 6.9.

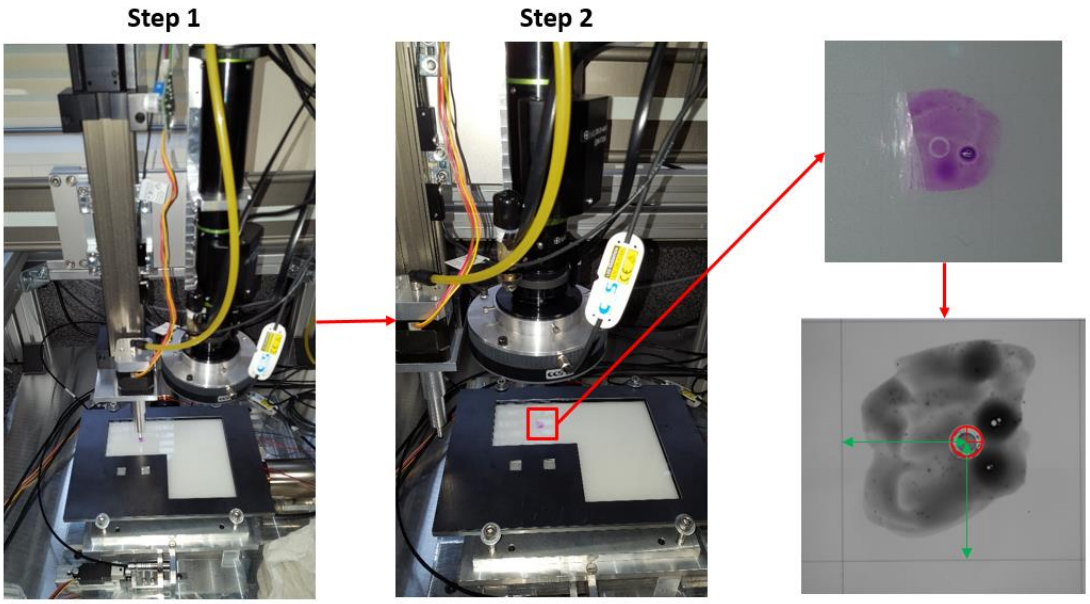

Figure 6.9 Offset measurement between the gripper tip and the camera

- Step 1: To begin with, the camera is placed above one of the grid squares so that the distance between the centre of the camera and the reference grid lines is 5mm along both directions. The MMS is used for precise alignment. Some ink is then spread on the grid square under the gripper tip and the gripper is moved down until the tip is pressed against the substrate, leaving a circle mark in the ink.
- Step 2: For a second time, the camera is moved above the ink mark and the distance between the centre of the circle left by the tip and the reference lines is measured. Based on the measured distances, the real distance between the gripper tip and the camera is 19.75mm along the X-axis and 89.85mm along the Y-axis.

6.5 Design for Automated Assembly

This section presents the assembly procedure used to automatically assemble two parts and the test carried out to quantify the overall positioning accuracy of the system. The measurement uncertainty of the vision system is first estimated, followed by a description of the assembly procedure, finishing with a positional accuracy test.

The system can carry out one assembly of 2 to 10 parts. A reference image of each part is uploaded to the vision system controller. The initial location and the target location and orientation of each part are written into a configuration file. The parts are then manually placed on the substrate using tweezers before running the application.

The sequence of the assembly is shown in Figure 6.10. To start with, the camera is moved above each part and snaps an image to locate their position and orientation within the substrate. The parts are then picked up and assembled in the assembly area, where the tape will hold the first part in place. At this stage of the project, a syringe is used to manually dispense UV curing glue before the assembly and a UV light is used at the end to bond the parts together.

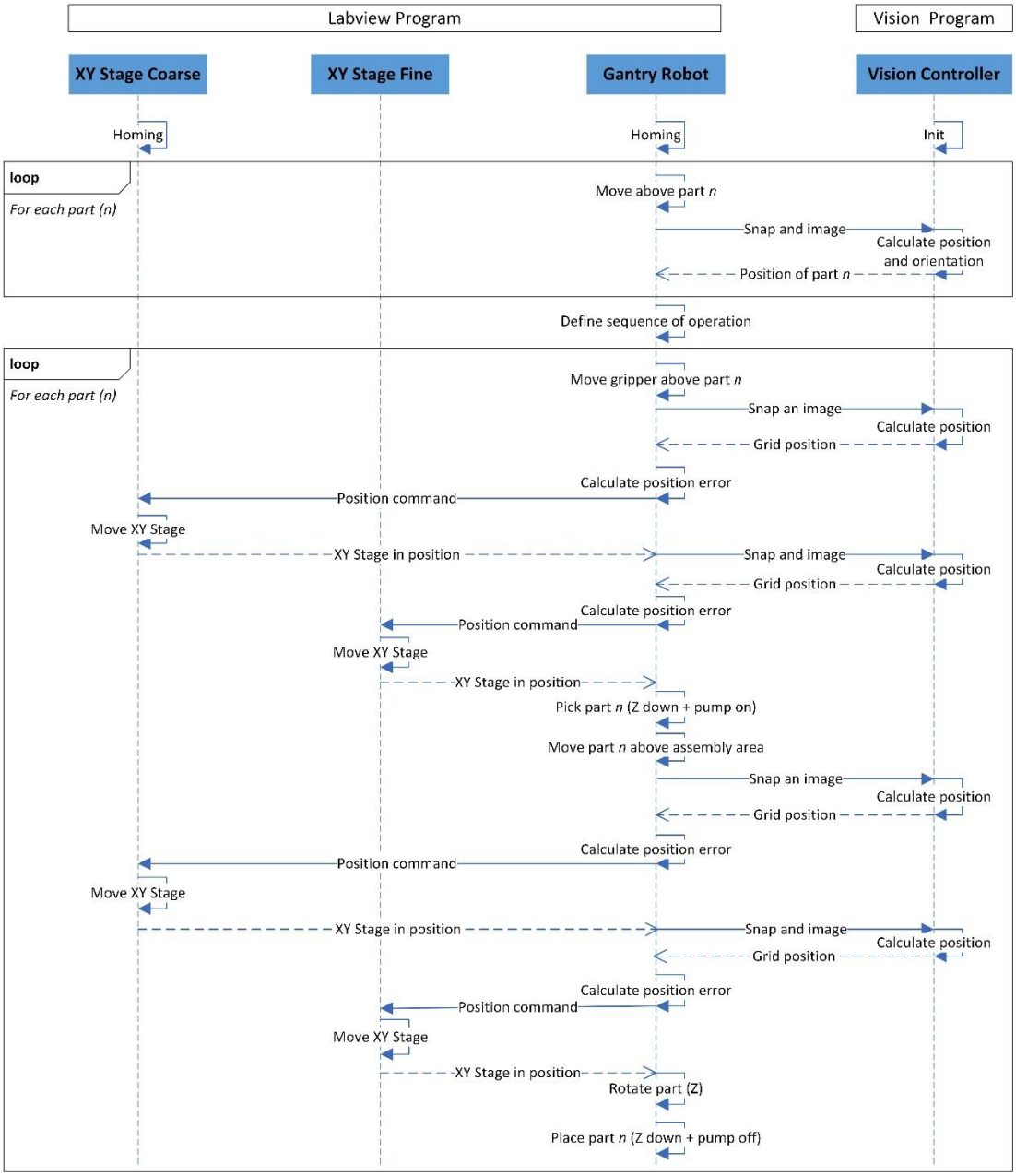

Figure 6.10 Sequence diagram of the assembly program

Every time a part is picked or placed, three successive operations are completed. Firstly, the pick-and-place manipulator is moved to its desired location. Secondly, an image is taken so that the manipulator is located above the substrate and the position error is sent to the MMS. Finally, after the position error is compensated with the MMS in coarse mode, a second image is taken and the position error is sent to the MMS for fine positioning compensation.

6.6 Position Accuracy and Assembly Test

6.6.1 Measurement Accuracy of the Vision System

Unlike the positioning errors of the manipulator and the MMS, the estimation of the measurement accuracy of the vision system is not straightforward because the camera is mounted on the manipulator and the datum is not fixed. Two tests are therefore setup to estimate the reading uncertainty of the parts and the lines.

6.6.1.1 Line Reading Accuracy

Firstly, the reading error of the substrate gridlines is estimated by placing the camera above one grid square and then moving the MMS along the X and Y directions. The MMS is successively moved in fine mode between 4 points following a square pattern of 200μm side length (Figure 6.11). The position of the X and Y reference lines is measured by the vision system at each of the four positions and the test is repeated ten times. The first recorded position of these two lines is used as the reference. The reading uncertainty is obtained for both directions by calculating the mean error of the 40 positions and adding three times the standard deviation. The resulting reading accuracy at 3σ is 5.5μm along the X-axis and 6.8μm along the Y-axis. Since this analysis relies on the MMS to generate the motion and the position command is used as a reference, the only uncertainty of this analysis is the positioning accuracy of the MMS, which is estimated to be smaller than 1μm.

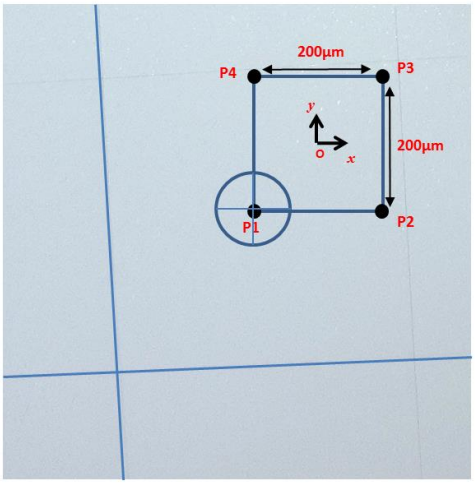

Figure 6.11 Line reading accuracy path

6.6.1.2 Part Reading Accuracy

The second test consists in estimating the reading error of the part detection algorithm for locating the part. This test follows exactly the same procedure as the first test (Figure 6.12). Unlike the part detection function created for the assembly sequence, the position of the part measured in this test is relative to the image itself, not the substrate gridlines. Otherwise, this test would integrate the errors from the line detection. The first recorded position of the part is used as the reference. The estimated reading accuracy at 3σ is 2.1µm along the X-axis and 1µm along the Y-axis. The reason for the part detection being more reliable than the line detection is due to the sharpness of the edges. The grid lines are only 8µm wide for a pixel size of 2.84µm and small distortions affecting the image quality are observed.

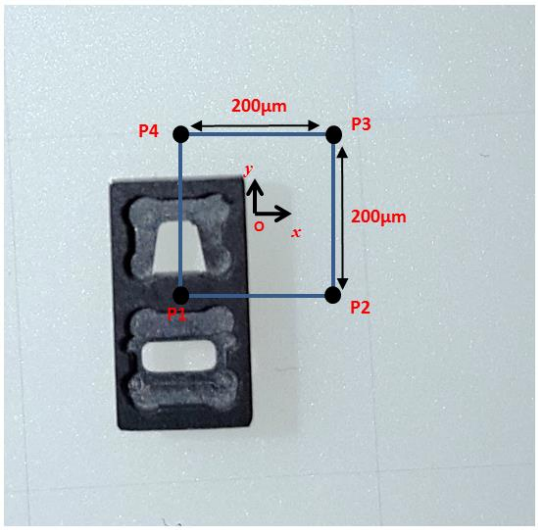

Figure 6.12 Part reading accuracy path

6.6.1.3 Total Reading Uncertainty

The results from these two independent tests must be combined in order to estimate the overall reading uncertainty. This is done using Monte Carlo statistical methods [213, 214]. The aim is to randomly add one sample of the line detection error data set and one sample of the part detection error data set. This routine is repeated N times, with N being a large number, for the X- and the Y-axis error.

The pseudocode used for the X-axis error is:

```
For N between 1 and 1,000,000 do

  i = rand()*40; // Generate a random integer i between 1 and 40, 40 corresponds to the
  sample size of each data set

  X1= Line_Position_Error_Along_X(i);
  // Extract the i^th sample from the line position error data set
  X2= Part_Position_Error_Along_X (i);
  // Extract the i^th sample from the part position error data set
  MonteCarloError(N) = X1 + X2;
  // Add these two samples and store them in the Monte Carlo data set

End
```

The same routine is used for the Y-axis error. The histograms of the reading errors are shown in Figure 6.13(a) for the X-axis and in Figure 6.13(b) for the Y-axis. The mean and standard deviation can finally be extracted from the Monte Carlo solution histograms. The total uncertainty of reading at 3σ of the vision system is therefore 5.8µm along the X-axis and 6µm along the Y-axis.

6.6.2 Assembly Tests

This assembly procedure is used to assemble a lens into a holder (Figure 6.14). The diameter of the hole in the holder is $7.000^{\pm 0.004}$mm and the diameter of the lens is also 7.000±0.004mm. This test is carried out to verify the ability of the system to automatically assemble two parts, but the tight fittings of the assembled parts does not allow for any measurement of the positioning error. However, because of the tight tolerances, a misalignment of the lens above the holder would be noticeable as the holder would be pushed sideways or the lens would tilt when inserted into the holder. This test can

therefore validate the efficiency of the program and verify the high positioning accuracy of the system.

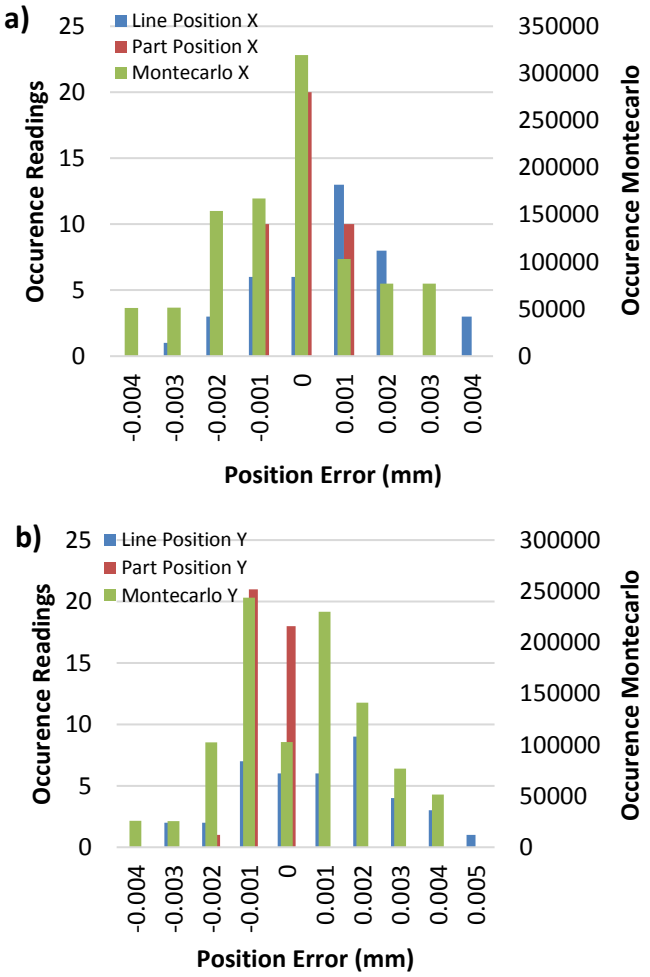

Figure 6.13 Histogram of the reading error for: a) the position error along X, b) the position error along Y

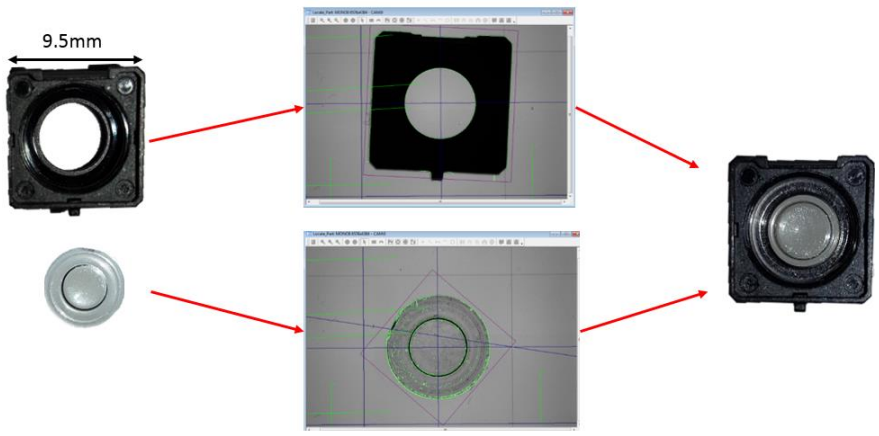

Figure 6.14 Assembly of a lens into a holder

6.6.3 Positioning Accuracy

The test assembly presented in the previous section is important but cannot be used to quantify the accuracy of the assembly. This is why the accuracy of the system is measured by manipulating a single part.

There is no formal way to define the pose accuracy of an assembly system. The accuracy of the systems in the literature is usually limited to the best result achieved or to the accuracy of the manipulator only. The test realised for the fabricated system is inspired by the ISO standard 9283:1998 but is based on only 10 samples for each part. Since this test includes the part detection realised before the manipulation, all the sources of error are taken into account. The pose accuracy could be measured using ink as for the camera offset calibration presented in Section 6.4.2, but this solution wouldn't integrate the error arising from the part detection and other errors. The procedure consists of placing five parts in five grid squares and moving them one by one to the centre of the five grid squares remaining in the workspace. A target distance of 5mm away from the X and Y reference grid lines was chosen but other values could be considered as long as the parts fit in a square. The scattered attained positions are plotted in Figure 6.15 and presented in Table 6.2.

Three methods are used to characterise the positioning accuracy. The first method is to calculate the mean error and the standard deviation along each axis for each part. The maximum error at 3σ is $11\pm18\mu m$ along the X-axis and $0\pm28\mu m$ along the Y-axis. The difference between the X-axis and the Y-axis errors is caused by the image distortions and the focal length errors being slightly different for the two reference lines.

The second method is to calculate the absolute mean error and repeatability for each part, as it is done in the ISO standard 9283:1998. The maximum absolute mean error is 11µm and the maximum repeatability is 24µm.

The third method is very similar to the second one. It involves using all the samples and calculating the overall absolute mean error and repeatability. This can be used to quantify the pose accuracy for the whole workspace. The resulting absolute mean error is 4µm and the absolute repeatability is 24µm.

Finally, the maximum absolute position error recorded is 21µm while the minimum error is 2µm.

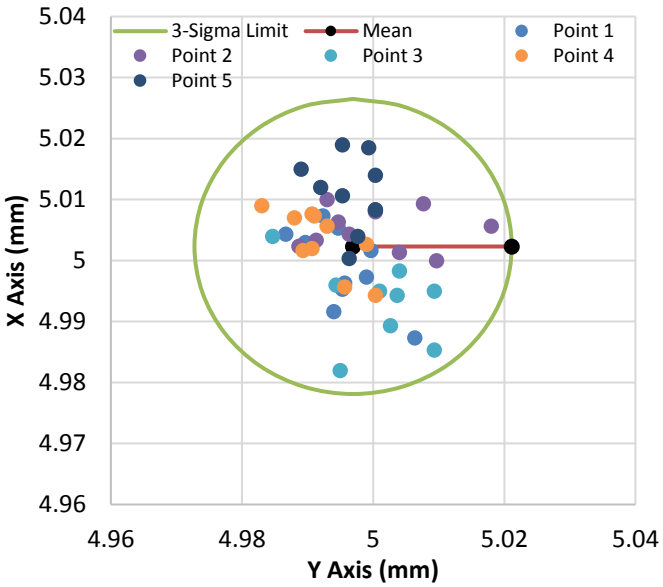

Figure 6.15 Scatter attained position

6.7 Summary

A low-cost compact hybrid manipulator was presented in this chapter. The system includes a conventional manipulator for pick-and-place operations and a dual-range MMS for fine positioning along the X- and Y-axes. The MMS has a positioning accuracy better than ±2µm. The use of a dual-range positioning method allows for low cost and high accuracy. A calibration grid is used as substrate for the assembly, where the grid lines are used as reference. The functions of a high resolution vision system include part detection and visual servoing of the manipulator position relative to the MMS. This enables the system to manipulate parts between 1mm and 10mm within a workspace of $20\times50mm^2$ without a need for expensive actuators and sensors. The overall pose accuracy reached in this application can be as high as 2µm and is ±24µm at 3σ. The concept of hybrid manipulation is therefore proven to be suitable for low-cost desktop size prototyping systems.

	Point P1		Point P2		Point P3		Point P4		Point P5	
Test ID	**X (mm)**	**Y (mm)**	**X (mm)**	**Y (mm)**	**X (mm)**	**Y (mm)**	**X (mm)**	**Y (mm)**	**X (mm)**	**Y (mm)**
1	5.004	4.987	5.000	5.010	4.982	4.995	5.003	4.999	5.008	5.000
2	5.002	5.000	5.006	5.018	4.996	4.994	4.994	5.000	5.019	4.999
3	5.007	4.992	5.002	4.989	4.998	5.004	5.007	4.991	5.004	4.998
4	4.995	4.995	5.008	5.000	4.989	5.003	5.008	4.991	5.015	4.989
5	4.997	4.999	5.003	4.991	5.004	4.985	5.009	4.983	5.014	5.000
6	4.996	4.996	5.009	5.008	4.995	5.009	5.002	4.989	5.019	4.995
7	5.005	4.995	5.010	4.993	4.985	5.009	5.002	4.991	5.012	4.992
8	5.003	4.990	5.001	5.004	4.995	5.001	5.006	4.993	5.008	5.000
9	4.987	5.006	5.006	4.995	4.994	5.004	4.996	4.996	5.011	4.995
10	4.992	4.994	5.004	4.996	4.992	4.999	5.007	4.988	5.000	4.996
Min Error (mm)	**-0.002**	**-0.000**	**0.000**	**0.000**	**-0.002**	**0.001**	**0.002**	**-0.001**	**0.000**	**0.000**
Max Error (mm)	**-0.013**	**0.013**	**0.010**	**0.018**	**-0.018**	**-0.015**	**0.009**	**-0.017**	**0.019**	**-0.011**
Mean Error (mm)	**-0.001**	**-0.005**	**0.005**	**0.000**	**-0.007**	**0.000**	**0.003**	**-0.008**	**0.011**	**-0.003**
3 × Standard Deviation (mm)	**0.019**	**0.017**	**0.010**	**0.028**	**0.019**	**0.023**	**0.015**	**0.016**	**0.018**	**0.011**
Absolute mean Error (mm)	**0.005**		**0.005**		**0.007**		**0.009**		**0.011**	
Repeatability at 3σ (mm)	**0.019**		**0.021**		**0.024**		**0.016**		**0.014**	

Table 6.2 Attained positions, accuracy and repeatability of the hybrid manipulator

Chapter 7Conclusion and Outlook

This chapter gives a summary of the work carried out in this thesis. The key contributions are highlighted and future work is proposed.

7.1 Summary

In an effort to reduce the cost and the size of miniaturised component assembly systems for prototyping applications, this thesis has proposed a hybrid manipulator combining a conventional pick-and-place manipulator for coarse positioning and a MMS for fine positioning. To meet the need for efficient design tools, a CMMS was designed using a new, simplified analytical model. From this thesis, the following conclusions were drawn:

1) A linear analytical model was derived and used to characterize a CMMS with basic parallelogram structures. The relationship between the actuation force and the resulting displacement was established using the PRBM and the Euler-Bernoulli model. The results of a comparison with FEA clearly show that the linear models give similar results but these results are only accurate for a very short range of motion (in this case, less than 1.5% of the beam's length). The fabrication of a 3-D printed prototype allowed for a first evaluation of the structure and a water jet machined prototype was then fabricated at full size to study the suitability of Nylon-66 instead of Aluminium 7075-T6 for the CMMS. The conclusion drawn is that this design offers a low cost CMMS solution with a low input force requirement and a large range of motion but lower resonant frequencies. Furthermore, the mechanical properties of this material change over time, mainly because of its sensitivity to temperature and humidity.

2) A simplified nonlinear stiffness model was derived to overcome the inaccuracies observed with the PRBM and the Euler-Bernoulli model. Meanwhile, another linear stiffness model was derived using the stiffness matrix method to obtain a 6-DOF dynamic model. Finally, the stress and nonlinear buckling were included so that a single analytical model could be used to fully characterise the CMMS in terms of actuation force, resonant frequencies and range of motion. This model was used for design optimisation using a multi-objective genetic algorithm, thus obtaining the best dimensional parameters in accordance with the design constraints. An Aluminium-7075 CMMS was then fabricated and the analytical model was verified using FEA and experimental validation. As the

results were all in accordance, the simplified analytical model was considered as an accurate design tool for CMMS composed with basic parallelogram structures.

3) The Nylon-66 CMMS was then used in the first prototype of a MMS actuated by VCAs. It was observed that the positioning error could reach more than 100μm by only controlling the input position. That is why a second set of sensors was integrated to measure the output position of the MMS within a shorter range of motion. By using the concept of dual-range manipulation, the positioning error was reduced to a few micrometres. A final MMS was then fabricated using the Aluminium-7075 CMMS to obtain a stiffer structure with constant mechanical properties and a smaller moving mass. A relative positioning accuracy of less than 2μm was achieved.

4) A miniaturised product assembly system was fabricated using the concept of hybrid manipulation. A standard pick-and-place manipulator was used as the coarse positioning mechanism. This allowed for a 4-DOF mobility and a positioning accuracy of less than 1mm along the X- and the Y-axes, less than 100μm along the Z-axis and less than 0.5° around the θ-axis. This system had the ability to manipulate parts between 1mm and 10mm in size using a vacuum gripper. The micro-motion was then implemented as the fine positioning mechanism used to compensate the positioning error along the X- and the Y-axes. A high resolution vision system was used for part detection and visual servoing, allowing for a fully automatic assembly. After calibration, the system's performance was evaluated by measuring the overall positioning accuracy over 50 pick-and-place operations. The results showed a positioning accuracy at 3σ of $\pm 24\mu m$.

5) The total hardware cost was kept below £50k (Table 7.1). The highest budget was allocated to the vision system as it is the key element of the overall positioning accuracy. The second highest budget was allocated to the manufacturing cost, mainly because of the setup time allocated to each unit. The rest of the cost is mainly due to the high resolution actuators, sensors and controllers used.

Subsystem	**Cost (£k)**
Vision System	27
Gantry Manipulator	7
MMS	4.5
Manufacturing	<11
Estimate of Total Cost	**<50**

Table 7.1 Cost estimation

7.2 Contribution

The main contributions of this thesis are listed below:

1) The 3-D printed prototype of a CMMS was fabricated and a test rig was proposed to generate forced vibrations and measure the resonant frequencies of the fabricated prototype.

2) A polymer-based CMMS was designed, fabricated and characterised. The use of abrasive jet machining with Nylon-66 instead of the usual WEDM with Aluminium-7075 shows a great potential for a low cost CMMS when implemented within an MMS. However, the change of mechanical properties over time and the reduced stiffness limit its application.

3) A new, simplified analytical model was proposed, including a nonlinear stiffness model and a dynamic model. Stress and buckling analyses for large beam deflections were integrated and used as a travel range limitation. The model was used as a tool for the design optimisation of an Aluminium-7075 CMMS. The experimental tests carried out on the fabricated CMMS were used to validate the analytical model.

4) The fabricated compliant CMMS was implemented in a dual-range MMS. A positioning accuracy better than 2µm was achieved with a range of motion of $4.6\times4.6mm^2$.

5) The MMS was implemented within a hybrid manipulator, allowing for the automatic assembly of two parts with a positioning accuracy of up to 2µm with a hardware cost smaller than £50k.

7.3 Future Work

7.3.1 Micro-Motion XY Stage

Although CMMSs are now well known and their advantages have been exploited for micro-assembly applications, their design methodology and characterisation techniques can still be improved. The analytical model developed in this thesis is proven to be efficient but can be further developed along with the experimental validation tests. Some future work is suggested below:

1) The fatigue life should be included in the analytical model and used as a constraint for the optimisation. Also, the evolution of accuracy under fatigue loading of compliant mechanisms could be studied in depth.

2) More testing should be carried out to validate the analytical model, especially the range limitation. A destructive test with buckling and plastic deformation could be carried out.

3) The fabricated CMMS should be made stiffer by increasing the thickness of the beams or by adding a set of beams to the outer parallelogram structures, so that the rotational stiffness is also increased. The range of motion would be reduced but would still be greater than the positioning error of the coarse manipulator.

4) The control system should be improved to increase the position resolution of the MMS without significantly increasing the cost. This can be achieved using a controller with a higher position command resolution.

5) Finally, the dual-range manipulation concept showing promising results, investing in more expensive hardware such as higher resolution sensors and motor controllers would result in a positioning accuracy way below one micrometre.

7.3.2 Hybrid Assembly System

Low-cost, flexible miniaturised product assembly is challenging as products are becoming smaller and smaller and the demand for custom, single unit production is increasing. The system designed in this thesis shows a great potential to answer this need but some improvement and optimisation must be carried out. Future work on the assembly system is proposed below:

1) The stiffness of the pick-and-place manipulator should be increased, for instance using preloaded bearings on the carriages and thicker mounting plates to fix the vision system. The mounting plate could be designed in a way so that the tilt can be adjusted manually to compensate any error caused by assembling the overall system. Finally, the Z-axis screw-drive could be replaced with a smaller, lighter and more accurate linear actuator.

2) Further work can be carried out on the gripper. A tool exchange mechanism could be integrated to the design so that different gripping techniques can be used, such as a vacuum gripper and compliant grippers of different sizes and gripping angle. A glue dispensing system should be added to the end-effector. Force sensing should be added to

the gripper so the force feedback along the Z-axis can be used along with position feedback.

3) Since most of the accuracy relies on the vision system, the position resolution could be improved by optimising the vision system. Firstly, some lens distortion was observed and could be compensated using a distortion correction algorithm. Additionally, the orientation of the plate used to mount the vision system should be made adjustable to ensure the FOV is perfectly parallel to the assembly substrate.

4) The substrate could be modified so the assembled parts are held in position without tape, thus no residual glue is left on the bottom part.

5) Vibration isolation should be integrated so that the coarse manipulator doesn't generate any vibration of the MMS. This can be achieved by making the CMMS stiffer, by using a high-order controller or by physically isolating the coarse manipulator from the fine manipulator.

REFERENCES

[1] Finetech. FINEPLACER® pico ma die bonder. http://www.finetechusa.com/bonders/products/fineplacerr-pico-ma.html, accessed on 20/02/2018, 2018.

[2] FemtoTools. FT-MTA03 Micromechanical Testing And Assembly System. http://www.femtotools.com/products/ft-mta03/description/, accessed on 20/02/2018, 2018.

[3] SmarAct. Automated Microassembly. http://www.smaract.com/products/automated-microassembly-stations, accessed on 20/02/2018, 2018.

[4] K.-B. Choi and J. J. Lee, "Analysis and Design of Linear Parallel Compliant Stage for Ultra-precision Motion Based on 4-PP Flexural joint Mechanism," in *Proceeding of the International Conference on Smart Manufacturing Application (ICSMA)*, 2008, pp. 35-38.

[5] D. Popa, R. Murthy, M. Mittal, S. Jeongsik, and H. Stephanou, "M3-Modular Multi-Scale Assembly System for MEMS Packaging," in *Proceeding of the IEEE/RSJ International Conference on Intelligent Robots and Systems* 2006, pp. 3712-3717.

[6] D. O. Popa and H. E. Stephanou, "Micro and Mesoscale Robotic Assembly," *Journal of Manufacturing Processes,* vol. 6, pp. 52–71, 2004.

[7] P. Kobel and R. Clavel, "Micro robot for rotary desktop assembly line," in *Proceeding of the IEEE International Symposium on Assembly and Manufacturing (ISAM)*, 2011, pp. 1-6.

[8] N. Siltala, A. Vuola, R. Heikkilae, and R. Tuokko, "A H-Scara Mini Robot - a Dual Parallel Kinematics Mini Manipulator," in *Robotics (ISR), 41st International Symposium on and 6th German Conference on Robotics (ROBOTIK)*, 2010, pp. 1-7.

[9] J. J. Uusitalo , H. Viinikainen, and R. Heikkilä, "Mini assembly cell for the assembly of mini-sized planetary gearheads," *Assembly Automation,* vol. 24, pp. 94 - 101, 2004.

[10] X. Hui, C. Liguo, S. Lining, and R. Weibin, "Hybrid Vision-Force Control for Automatic Assembly of Miniaturized Gear System," in *Proceedings of the IEEE International Conference on Robotics and Automation*, 2005, pp. 1368-1373.

[11] Q. Qi and R. Du, "A Vision Based Micro-Assembly System for Assembling Components in Mechanical Watch Movements," in *Proceeding of the International Symposium on Optomechatronic Technologies (ISOT)*, 2010.

[12] M. Probst, K. Vollmers, B. E. Kratochvil, and B. J. Nelson, "Design of an Advanced Microassembly System for the Automated Assembly of Bio-Microrobots," in *Proceeding of the 5th International Workshop on Microfactories*, 2004.

[13] M. Probst, C. Hürzeler, R. Borer, and B. J. Nelson, "A Microassembly System for the Flexible Assembly of Hybrid Robotic Mems Devices," *International Journal of Optomechatronics,* vol. 3, pp. 69-90, 2009.

[14] M. Kagerer, K. L. Eiler, F. Irlinger, and T. C. Lueth, "Development and application of a low-cost manual micro assembly system with integrated heater," in *Proceeding of the IEEE International Conference on Robotics and Biomimetics (ROBIO)*, 2011, pp. 2963-2968.

[15] B. Kim, H. Kang, D.-H. Kim, and J.-O. Park, "A flexible microassembly system based on hybrid manipulation scheme for manufacturing photonics components," *The International Journal of Advanced Manufacturing Technology,* vol. 28, pp. 379-386, 2006.

[16] W. Chen, F. Yu, J. Qu, W. Chen, and J. Zhang, "Micro-vision servo control of a multi-axis alignment system for optical fiber assembly," *Journal of Micromechanics and Microengineering,* vol. 27, p. 045010, 2017.

[17] R. H. Heikkila, I. T. Karjalainen, J. J. Uusitalo, A. S. Vuola, and R. O. Tuokko, "Possibilities of a Microfactory in the Assembly of Small Parts and Products - First Results of the M4-project," in *Proceeding of the IEEE International Symposium on Assembly and Manufacturing*, 2007, pp. 166-171.

[18] A. N. Das, P. Zhang, W. H. Lee, D. O. Popa, and H. E. Stephanou, "μ3: Multiscale, Deterministic Micro-Nano Assembly System for Construction of On-Wafer Microrobots," in *Proceeding of the IEEE International Conference on Robotics and Automation*, 2007, pp. 461-466.

[19] N. Dechev, R. Lu, W. Liu, W. L. Cleghorn, and J. K. Mills, "Development of a 6 degree of freedom robotic micromanipulator for use in 3D MEMS microassembly," in *Proceeding of the IEEE International Conference on Robotics and Automation*, 2006, pp. 281-288.

[20] E. D. Kunt, A. T. Naskali, I. S. M. Khalil, A. Sabanovic, and E. Yüksel, "Design and development of workstation for microparts manipulation and assembly,"

Turkish Journal of Electrical Engineering & Computer Sciences, vol. 19, pp. 973-992, 2011.

[21] H. Bilen and M. Unel, "Micromanipulation Using a Microassembly Workstation with Vision and Force Sensing," in *Advanced Intelligent Computing Theories and Applications*, D.-S. Huang, D. C. Wunsch, D. S. Levine, and K.-H. Jo, Eds., ed Berlin, Heidelberg: Springer Berlin Heidelberg, 2008, pp. 1164-1172.

[22] J. Hesselbach, K. Schöttler, R. Tutsch, and M. Berndt, "Assembly of Hybrid Microsystems Using an Assembly System with 3D Optical Sensor," *CIRP Annals - Manufacturing Technology,* vol. 55, pp. 11-14, 2006.

[23] A. Burisch, J. Wrege, A. Raatz, J. Hesselbach, and R. Degen, "PARVUS – miniaturised robot for improved flexibility in micro production," *Assembly Automation,* vol. 27, pp. 65-73, 2007.

[24] G. Borchert, A. Burisch, and A. Raatz, "APIS — A miniaturized robot for precision assembly with low-cost piezoelectric motors," *International Journal of Precision Engineering and Manufacturing,* vol. 12, pp. 629-634, 2011.

[25] N. Siltala, T. Prusi, A. Vuola, R. Heikkila, and R. Tuokko, "Modular microfactory system for gas sensor assembly," in *Proceeding of the IEEE International Symposium on Assembly and Manufacturing (ISAM)*, 2011, pp. 1-6.

[26] E. D. Kunt, A. T. Naskali, and A. Sabanovic, "Miniaturized modular manipulator design for high precision assembly and manipulation tasks," in *Proceeding of the IEEE International Workshop on Advanced Motion Control (AMC)*, 2012, pp. 1-6.

[27] Z. Zhakypov, T. Uzunovic, A. O. Nergiz, E. A. Baran, E. Golubovic, and A. Sabanovic, "Desktop microfactory for high precision assembly and machining," in *Proceeding of the IEEE International Symposium on Industrial Electronics (ISIE)*, 2014, pp. 1192-1197.

[28] S. Perroud, A. Codourey, and Y. Mussard, "PocketDelta: a miniature robot for micro-assembly," in *Procceding of the 5th International Workshop on Microfactories*, 2006.

[29] C. Clévy, A. Hubert, and N. Chaillet, "Flexible micro-assembly system equipped with an automated tool changer," *Journal of Micro-Nano Mechatronics,* vol. 4, pp. 59-72, 2008.

[30] A. N. Das, R. Murthy, D. O. Popa, and H. E. Stephanou, "A Multiscale Assembly and Packaging System for Manufacturing of Complex Micro-Nano Devices," *IEEE Transactions on Automation Science and Engineering,* vol. 9, pp. 160-170, 2012.

[31] F. Shen, W. Wu, D. Yu, D. Xu, and Z. Cao, "High-Precision Automated 3-D Assembly With Attitude Adjustment Performed by LMTI and Vision-Based Control," *IEEE/ASME Transactions on Mechatronics,* vol. PP, pp. 1-13, 2014.

[32] M. Santochi, M. Porta, and G. Fantoni, "AN ASSEMBLY MICROFACTORY FOR HYBRID MICROPRODUCTS," in *Proceedings of the 9th Biennial ASME Conference on Engineering Systems Design and Analysis*, Haifa, Israel, 2008.

[33] B. Tamadazte, N. Le Fort-Piat, S. Dembele, and E. Marchand, "Microassembly of complex and solid 3D MEMS by 3D vision-based control," in *Proceeding of the IEEE/RSJ International Conference on Intelligent Robots and Systems*, 2009, pp. 3284-3289.

[34] S. Xiao and Y. Li, "Visual Servo Feedback Control of a Novel Large Working Range Micro Manipulation System for Microassembly," *Journal of Microelectromechanical Systems,* vol. 23, pp. 181-190, 2014.

[35] D. O. Popa, L. W. Ho, R. Murthy, A. N. Das, and H. E. Stephanou, "High Yield Automated MEMS Assembly," in *Proceeding of the IEEE International Conference on Automation Science and Engineering*, 2007, pp. 1099-1104.

[36] S. Xiao and Y. Li, "Design and analysis of a novel flexure-based XY micro-positioning stage driven by electromagnetic actuators," in *Proceeding of the International Conference on Fluid Power and Mechatronics*, 2011, pp. 953-958.

[37] X. D. Wang, Y. Luo, X. W. Zhang, L. Teng, W. M. Yang, and L. Chen, "Precision equipments for assembly of miniature devices: System architecture and technological approaches," in *Proceeding of the IEEE International Symposium on Assembly and Manufacturing (ISAM)*, 2013, pp. 148-150.

[38] Z. Zhang, J. Zhang, and D. Xu, "Design of microassembly system and research on coarse-to-fine alignment strategy in combination with active zooming," in *Proceeding of the IEEE Workshop on Robot Vision (WORV)*, 2013, pp. 76-81.

[39] S. Liu, D. Xu, D. Zhang, and Z. Zhang, "High Precision Automatic Assembly Based on Microscopic Vision and Force Information," *IEEE Transactions on Automation Science and Engineering,* vol. 13, pp. 382-393, 2016.

[40] M. Bartenwerfer, C. Diederichs, and S. Fatikow, "Automated robotic assembly for a micro-cartridge system inside the scanning electron microscope," in *Proceeding of the IEEE International Conference on Robotics and Automation (ICRA)*, 2014, pp. 5197-5202.

[41] B. Tamadazte, E. Marchand, S. Dembélé, and N. L. Fort-Piat, "CAD Model-based

Tracking and 3D Visual-based Control for MEMS Microassembly," *The International Journal of Robotics Research,* vol. 29, pp. 1416-1434, 2010.

[42] A. V. Kudryavtsev, G. J. Laurent, C. Clevy, B. Tamadazte, and P. Lutz, "Stereovision-based control for automated MOEMS assembly," in *Proceeding of the IEEE/RSJ International Conference on Intelligent Robots and Systems (IROS)*, 2015, pp. 1391-1396.

[43] L. Ren, L. Wang, J. K. Mills, and D. Sun, "3-D automatic microassembly by vision-based control," in *Proceeding of the IEEE/RSJ International Conference on Intelligent Robots and Systems*, 2007, pp. 297-302.

[44] L. Ren, L. Wang, J. K. Mills, and D. Sun, "Vision-Based 2-D Automatic Micrograsping Using Coarse-to-Fine Grasping Strategy," *IEEE Transactions on Industrial Electronics,* vol. 55, pp. 3324-3331, 2008.

[45] L. Wang, L. Ren, J. K. Mills, and W. L. Cleghorn, "Automated 3-D Micrograsping Tasks Performed by Vision-Based Control," *IEEE Transactions on Automation Science and Engineering,* vol. 7, pp. 417-426, 2010.

[46] Y. Okazaki, N. Mishima, and K. Ashida, "Microfactory—Concept, History, and Developments," *Journal of Manufacturing Science and Engineering,* vol. 126, pp. 837-844, 2005.

[47] T. Gaugel, M. Bengel, and D. Malthan, "Building a mini‐assembly system from a technology construction kit," *Assembly Automation,* vol. 24, pp. 43-48, 2004.

[48] G. Borchert, A. Burisch, and A. Raatz, "Advantages of task‐adapted parallel Robot Systems featuring Modularity and Reconfigurability," in *13th World Congress in Mechanism and Machine Science*, Guanajuato, México, 2011.

[49] E. Järvenpää, R. Heikkilä, N. Siltala, T. Prusi, and R. Tuokko, "Micro-factories," in *Micromanufacturing Engineering and Technology*, 2nd ed: Elsevier, 2015, pp. 549-579.

[50] E. Järvenpää, R. Heikkilä, and R. Tuokko, "TUT-microfactory – a small-size, modular and sustainable production system," in *Proceeding of the 11th Global Conference on Sustainable Manufacturing - Innovative Solutions*, Berlin, Germany, 2013, pp. 78 - 83.

[51] T. Prusi, A. Vuola, N. Siltala, R. Heikkilae, and R. Tuokko, "Robots for Micro and Desktop Factories: Examples and Experiences," in *Proceeding of the 41st International Symposium on Robotics (ISR) and 6th German Conference on*

Robotics (ROBOTIK), 2010, pp. 1-7.

[52] A. Hofmann, B. Hummel, O. Firat, G. Bretthauer, M. Bar, and M. Meyer, "microFLEX - A new concept to address the needs for adaptable meso and micro assembly lines," in *Proceeding of the IEEE International Symposium on Assembly and Manufacturing (ISAM)*, 2011, pp. 1-5.

[53] R. Tuokko, R. Heikkilä, E. Järvenpää, A. Nurmi, T. Prusi, N. Siltala*, et al.*, "Micro and Desktop Factory Roadmap," Tampere University of Technology, 2012.

[54] J. Ellwood, A. Burisch, K. Schöttler, G. Pokar, A. Raatz, and J. Hesselbach, "Size-Adapted Manipulation Robots for Microassembly," in *Design and Manufacturing of Active Microsystems*, ed: Springer Berlin Heidelberg, 2011, pp. 269-286.

[55] Z. Zhakypov, T. Uzunovic, A. O. Nergiz, E. A. Baran, E. Golubovic, and A. Sabanovic, "Modular and reconfigurable desktop microfactory for high precision manufacturing," *The International Journal of Advanced Manufacturing Technology,* pp. 1-11, 2016.

[56] R. S. Fearing, "Survey of sticking effects for micro parts handling," in *Proceedings of the IEEE/RSJ International Conference on Intelligent Robots and Systems. Human Robot Interaction and Cooperative Robots*, 1995, pp. 212-217.

[57] E. T. Enikov, "Micro- and Nano-assembly and Manipulation Techniques for MEMS," in *Microsystems Mechanical Design*, F. De Bona and E. T. Enikov, Eds., ed: Springer Vienna, 2006, pp. 135-156.

[58] M. Savia and H. N. Koivo, "Contact Micromanipulation—Survey of Strategies," *IEEE/ASME Transactions on Mechatronics,* vol. 14, pp. 504-514, 2009.

[59] L. Pierre and D. Alain, "A study of capillary forces as a gripping principle," *Assembly Automation,* vol. 25, pp. 275-283, 2005.

[60] J. Cecil, D. Powell, and D. Vasquez, "Assembly and manipulation of micro devices—A state of the art survey," *Robotics and Computer-Integrated Manufacturing,* vol. 23, pp. 580–588, 2007.

[61] R. K. Jain, S. Majumder, B. Ghosh, and S. Saha, "Design and manufacturing of mobile micro manipulation system with a compliant piezoelectric actuator based micro gripper," *Journal of Manufacturing Systems,* vol. 35, pp. 76-91, 2015.

[62] D. Heriban and M. Gauthier, "Robotic micro-assembly of microparts using a piezogripper," in *IEEE/RSJ International Conference on Intelligent Robots and Systems (IROS)* 2008, pp. 4042-4047.

[63] J. Agnus, N. Chaillet, C. Clévy, S. Dembélé, M. Gauthier, Y. Haddab*, et al.*,

"Robotic Microassembly and micromanipulation at FEMTO-ST," *Journal of Micro-Bio Robotics.,* vol. 8, pp. 91-106, 2013 2013.

[64] R. K. Jain, S. Datta, S. Majumder, and A. Dutta, "Development of Multi Micro Manipulation System Using IPMC Micro Grippers," *Journal of Intelligent & Robotic Systems,* vol. 74, pp. 547-569, 2014.

[65] B. P. Solano, A. J. Gallant, and D. Wood, "Design and Optimisation of a Microgripper: Demonstration of Biomedical Applications Using the Manipulation of Oocytes," in *Symposium on Design, Test, Integration & Packaging of MEMS/MOEMS*, 2009, pp. 61-65.

[66] X. Huang, X. Lv, and M. Wang, "Development of A Robotic Microassembly System with Multi-Manipulator Cooperation," in *Proceedings of the IEEE International Conference on Mechatronics and Automation*, 2006, pp. 1197-1201.

[67] M. Helal, L. Chen, L. Sun, and B. Shao, "Micro/nano grip and move compliant mechanism with parallel movement tips," in *in Proceeding of the IEEE Conference on Nanotechnology*, 2009, pp. 130-132.

[68] B. H. Kang and J. T. Wen, "Design of Compliant MEMS Grippers for Micro-Assembly Tasks," in *Proceeding of the IEEE/RSJ International Conference on Intelligent Robots and Systems*, 2006, pp. 760-765.

[69] Q. Xu, "Structure design of a new compliant gripper based on Scott-Russell mechanism," in *Proceeding of the IEEE International Conference on Robotics and Biomimetics (ROBIO)*, 2013, pp. 1623-1628.

[70] Y. Jia and Q. Xu, "MEMS Microgripper Actuators and Sensors: The State-of-the-Art Survey," *Recent Patents on Mechanical Engineering,* vol. 6, 2013.

[71] W. Aia and Q. Xu, "Overview of flexure-based compliant microgrippers," *Advances in robotics research,* vol. 1, pp. 1-19, 2014.

[72] X. Sun, W. Chen, Y. Tian, S. Fatikow, R. Zhou, J. Zhang*, et al.*, "A novel flexure-based microgripper with double amplification mechanisms for micro/nano manipulation," *Review of Scientific Instruments,* vol. 84, p. 085002, 2013.

[73] D. Petrovic, G. Popovic, E. Chatzitheodoridis, O. Del Medico, A. Almansa, F. Sumecz*, et al.*, "Gripping tools for handling and assembly of microcomponents," in *Proceeding of the 23rd International Conference on Microelectronics*, 2002, pp. 247-250 vol.1.

[74] W.-r. Wu, D.-h. Yu, K. Du, Z.-r. Qiu, and X.-h. Huang, "A precision robotic system for 3-D Micro-Assembly," in *Proceeding of the IEEE International Conference on*

Robotics and Biomimetics, 2012, pp. 1518-1522.

[75] G. Hao and X. Kong, "Conceptual Design and Modelling of a Self-Adaptive Compliant Parallel Gripper for High-Precision Manipulation," pp. 161-167, 2012.

[76] N. Dechev, W. L. Cleghorn, and J. K. Mills, "Microassembly of 3-D Microstructures Using a Compliant, Passive Microgripper," *Journal of Microelectromechanical Systems,* vol. 13, pp. 176-189, 2004.

[77] X. Huang, L. Chang, and W. Ming, "An automatic vacuum microgripper," in *Proceeding of the 8th World Congress on Intelligent Control and Automation (WCICA)*, 2010, pp. 5528-5532.

[78] W. Mann, G. Peschl, and C. Wogerer, "Development of flexible gripper for precision assembly of cylinder locks," in *Proceeding of the IEEE International Symposium on Assembly and Manufacturing*, 2007, pp. 19-24.

[79] A. Burisch, C. Loechte, A. Raatz, and A. Fabrizi, "Cambio – A Miniaturized Tool Changer for Desktop Factory Application," in *Proceedings of EUCOMES 08*, ed: Springer Netherlands, 2009, pp. 541-548.

[80] H. Choi and M. Koç, "Design and feasibility tests of a flexible gripper based on inflatable rubber pockets," *International Journal of Machine Tools and Manufacture,* vol. 46, pp. 1350-1361, 2006.

[81] X.-D. Wang, Y.-Z. Chi, Y. Luo, X.-W. Zhang, L. Chen, and W.-M. Yang, "An exchangeable gripper module integrated in the assembly system for multi miniature parts," in *Proceeding of the IEEE International Conference on Information and Automation (ICIA)*, 2014, pp. 887-891.

[82] T.-R. Hsu, "Micro Assembly - A technology on the frontier of new industrial automation," in *Proceeding of the 8th International Conference on Automation Technology*, 2005.

[83] X. Kong and C. M. Gosselin, *Type synthesis of parallel mechanisms* vol. 33: Springer, 2007.

[84] J.-P. Merlet, C. Gosselin, and T. Huang, "Parallel Mechanisms," in *Springer Handbook of Robotics*, B. Siciliano and O. Khatib, Eds., ed Cham: Springer International Publishing, 2016, pp. 443-462.

[85] H. Kozuka, J. Arata, K. Okuda, A. Onaga, M. Ohno, A. Sano*, et al.*, "Compliant-Parallel Mechanism for High Precision Machine with a Wide Range of Working Area," in *Proceeding of the IEEE/RSJ International Conference on Intelligent Robots and Systems (IROS)*, 2012, pp. 2519-2524.

[86] D. Jie, L. Sun, Y. Liu, Y. Zhu, and H. Cai, "Design and Simulation of a Macro-micro Dual-drive High Acceleration Precision XY-stage for IC Bonding Technology," in *Proceeding of the 6th International Conference on Electronic Packaging Technology*, 2005, pp. 161-165.

[87] W. Dong, L. N. Sun, and Z. J. Du, "Design of a precision compliant parallel positioner driven by dual piezoelectric actuators," *Sensors and Actuators,* vol. 135, pp. 250–256, 2007.

[88] L. Hau-Wei, L. Chien-Hung, C. Yu-Ying, and F. Te-Hua, "Design and control of an optical alignment system using a parallel XXY stage and four CCDs for micro pattern alignment," in *Proceeding of the Symposium on Design, Test, Integration and Packaging of MEMS/MOEMS (DTIP)*, 2012, pp. 13-17.

[89] S. Lin, Y. Jia, I. P. Lei, and Q. Xu, "Design and Optimization of a Long-Stroke Compliant Micropositioning Stage Driven by Voice Coil Motor," in *Proceeding of the 12th International Conference on Control Automation Robotics & Vision (ICARCV)*, 2012, pp. 1716-1721.

[90] K. Yonemoto, Y. Takeda, Z. Tong, and M. Higuchi, "A New Flexure Revolute Joint with Leaf springs and Its Application to Large Workspace Parallel Robot," *Journal of Advanced Mechanical Design, Systems, and Manufacturing,* vol. 6, pp. 76-87, 2012.

[91] J. Hesselbacha, A. Raatz, and H. Kunzmannb, "Performance of Pseudo-Elastic Flexure Hinges in Parallel Robots for Micro-Assembly Tasks," *CIRP Annals - Manufacturing Technology,* vol. 53, pp. 329–332, 2004.

[92] A. Raatz, J. Wrege, A. Burisch, and J. Hesselbach, "Compliant Parallel Robots," *IFIP Precision Assembly Technologies for Mini and Micro Products,* vol. 198, pp. 83-92, 2006.

[93] Y.-M. Moon and S. Kota, "Design of Compliant Parallel Kinematic Machines," in *in Proceeding of the ASME International Design Engineering Technical Conferences and Computers and Information in Engineering Conference*, 2002, pp. 35-41.

[94] H. Kozuka, J. Arata, K. Okuda, A. Onaga, M. Ohno, A. Sano*, et al.*, "A Bio-Inspired Compliant Parallel Mechanism for High-Precision Robots," in *in Proceeding of the IEEE International Conference on Robotics and Automation* 2012, pp. 3122-3127.

[95] J. Cecil, D. Powell, and D. Vasquez, "A review of gripping and manipulation techniques for micro-assembly applications," *International Journal of Production*

Research, vol. 43, pp. 819-828, 2005.

[96] X. Yang, W. Li, Y. Wang, L. Zhang, G. Ye, and X. Su, "Analysis of The Displacement of Complaint Double Parallel Fourbar Mechanism," in *Proceeding of the IEEE Conference on Industrial Electronics and Applications (ICIEA)*, 2009, pp. 2760-2763.

[97] N. Tolou, V. A. Henneken, and J. L. Herder, "Statically Balanced Compliant Micro Mechanisms (SB-MEMS): Concepts and Simulation," in *Proceedings of the ASME International Design Engineering Technical Conferences & Computers and Information in Engineering Conference (IDETC/CIE)*, 2010, pp. 447-454.

[98] G. Hao and X. Kong, "Novel XY Compliant Parallel Manipulators for Large Displacement Translation With Enhanced Stiffness," in *Proceedings of the ASME International Design Engineering Technical Conferences & Computers and Information in Engineering Conference (IDETC/CIE)*, Montreal, 2010 pp. 1037-1047.

[99] B. P. Trease, Y. Moon, and S. Kota, "Design of Large-Displacement Compliant Joints," *Journal of Mechanical Design,* vol. 127, pp. 788-798, 2005.

[100] F. Dirksen, M. Anselmann, T. I. Zohdi, and R. Lammering, "Incorporation of flexural hinge fatigue-life cycle criteria into the topological design of compliant small-scale devices," *Precision Engineering,* vol. 37, pp. 531-541, 2013.

[101] Y. Tian, B. Shirinzadeh, and D. Zhang, "Design and dynamics of a 3-DOF flexure-based parallel mechanism for micro/nano manipulation," *Microelectronic Engineering,* vol. 87, pp. 230-241, 2010.

[102] Y. Li, J. Huang, and H. Tang, "A Compliant Parallel XY Micromotion Stage With Complete Kinematic Decoupling," *IEEE Transactions on Automation Science and Engineering,* vol. 9, pp. 538-553, 2012.

[103] Y. Yun and Y. Li, "Design and analysis of a novel 6-DOF redundant actuated parallel robot with compliant hinges for high precision positioning," *Nonlinear Dynamics,* vol. 61, pp. 829-845, 2010.

[104] D. Kang and D. Gweon, "Analysis of large range rotational flexure in precision 6-DOF tripod robot," in *Proceeding of the 12th International Conference on Control, Automation and Systems* 2012, pp. 2117-2120.

[105] L. L. Howell, S. P. Magleby, and B. M. Olsen, "Elements of Mechanisms," in *Handbook of Compliant Mechanisms*, ed New York: John Wiley & Sons Ltd., 2013.

[106] G. Hao and J. Yu, "Design, Modelling and Analysis of a Completely-Decoupled

XY Compliant Parallel Manipulator," *Mechanism and Machine Theory,* vol. 102, pp. 179-195, 2016.

[107] B. Deshmukha, S. Pardeshib, R. Mistrya, S. Kandharkarb, and S. Waghb, "Development of a Four bar Compliant Mechanism using Pseudo Rigid Body Model (PRBM)," *Procedia Materials Science,* vol. 6, pp. 1034–1039, 2014.

[108] H. Tang and Y. Li, "Design, Analysis, and Test of a Novel 2-DOF Nanopositioning System Driven by Dual Mode," *IEEE Transactions on Robotics,* vol. 29, pp. 650-662, 2013.

[109] G. Hao and J. Yu, "A Completely Kinematostatically Decoupled XY Compliant Parallel Manipulator through New Topology Structure," in *Proceedings of the IFToMM Workshop on Fundamental Issues and Future Research Directions for Parallel Mechanisms and Manipulators*, Tianjin, China, 2014.

[110] Y. Li and Q. Xu, "Design and Analysis of a Totally Decoupled Flexure-Based XY Parallel Micromanipulator," *IEEE Transactions on Robotics* vol. 25, pp. 645-657, 2009.

[111] Q. Wang and X. Zhang, "Fatigue reliability based optimal design of planar compliant micropositioning stages," *Review of Scientific Instruments,* vol. 86, p. 105117, 2015.

[112] I. Ivanov and B. Corves, "Flexure Hinge-Based Parallel Manipulators Enabling High-Precision Micro Manipulations," in *Micromechanics and Microactuators*. vol. 2, ed: Springer Netherlands, 2012, pp. 49-60.

[113] D. Kang and D. Gweon, "Development of flexure based 6-degrees of freedom parallel nano-positioning system with large displacement," *Review of Scientific Instruments,* vol. 83, p. 035003, 2012.

[114] H. Kozukaa, J. Arataa, K. Okudab, A. Onagab, M. Ohnob, A. Sanoa*, et al.*, "A Compliant-Parallel Mechanism with Bio-Inspired Compliant Joints for High Precision Assembly Robot," in *Proceeding of the CIRP Conference on BioManufacturing* 2013, pp. 175–178.

[115] T. Noll, "Three axis rotational flexure joints of high axial stiffness," *Precision Engineering,* vol. 26, pp. 460-465, 2002.

[116] K. Schöttler, A. Raatz, and J. Hesselbach, *Size-adapted Parallel and Hybrid Parallel Robots for Sensor Guided Micro Assembly*, 2008.

[117] S. Polit and J. Dong, "Design of high-bandwidth high-precision flexure-based nanopositioning modules," *Journal of Manufacturing Systems,* vol. 28, pp. 71-77,

7// 2009.

[118] P. R. Ouyang, "A spatial hybrid motion compliant mechanism: Design and optimization," *Mechatronics,* vol. 21, pp. 479–489, 2011.

[119] Q. Yao, J. Dong, and P. M. Ferreira, "Design, analysis, fabrication and testing of a parallel-kinematic micropositioning XY stage," *International Journal of Machine Tools and Manufacture* vol. 47, pp. 946–961, 2007.

[120] S. Xiao and Y. Li, "Optimal Design, Fabrication, and Control of an XY Micropositioning Stage Driven by Electromagnetic Actuators," *IEEE Transactions on Industrial Electronics,* vol. 60, pp. 4613 - 4626, 2013.

[121] X. Zhang and Q. Xu, "Design and analysis of an in-plane flexure XYZ micro/nano-positioning stage," in *Proceeding of the International Conference on Advanced Robotics and Mechatronics*, Macau, 2016.

[122] Y. K. Yong, S. S. Aphale, and S. O. R. Moheimani, "Design, Identification, and Control of a Flexure-Based XY Stage for Fast Nanoscale Positioning," *IEEE Transactions on Nanotechnology,* vol. 8, pp. 46-54, 2009.

[123] Y. Du, T. Li, W. Ji, and Y. Jiang, "Design and Testing of a 2-DOF Flexure-based Compliant Stage," *MATEC Web Conf.,* vol. 95, p. 07013, 2017.

[124] P. R. Ouyang, W. J. Zhang, and M. M. Gupta, "A New Compliant Mechanical Amplifier Based on a Symmetric Five-Bar Topology," *Journal of Mechanical Design,* vol. 130, pp. 104501-104501-5, 2008.

[125] X. Zhang, Y. Zhang, and Q. Xu, "Design and control of a novel piezo-driven XY parallel nanopositioning stage," *Microsystem Technologies,* vol. 23, pp. 1067-1080, 2017.

[126] J. Yu, Y. Xie, Z. Li, and G. Hao, "Design and Experimental Testing of an Improved Large-Range Decoupled XY Compliant Parallel Micromanipulator," *Journal of Mechanisms and Robotics,* vol. 7, pp. 044503-044503-6, 2015.

[127] G. Hao, Q. Meng, and Y. Li, "Design of Large-range XY Compliant Parallel Manipulators Based on Parasitic Motion Compensation," in *Proceedings of the ASME International Design Engineering Technical Conferences & Computers and Information in Engineering Conference (IDETC/CIE)*, 2013

[128] S. Awtar and G. Parmar, "Design of a Large Range XY Nanopositioning System," *Journal of Mechanisms and Robotics,* vol. 5, pp. 021008-021008-10, 2013.

[129] Q. Xu, "New Flexure Parallel-Kinematic Micropositioning System With Large Workspace," *IEEE Transactions on Robotics,* vol. 28, pp. 478-491, 2012.

[130] S. Wan and Q. Xu, "Design of a new compliant XY micro-positioning stage based on Roberts mechanism," in *Proceeding of the International Conference on Manipulation, Manufacturing and Measurement on the Nanoscale (3M-NANO)*, 2014, pp. 139-144.

[131] G. Hao and X. Kong, "A Novel Large-Range XY Compliant Parallel Manipulator With Enhanced Out-of-Plane Stiffness," *Journal of Mechanical Design,* vol. 134, pp. 061009-061009-9, 2012.

[132] Q. Xu, "Design and Development of a Compact Flexure-Based Precision Positioning System With Centimeter Range," *IEEE Transactions on Industrial Electronics,* vol. 61, pp. 893-903, 2014.

[133] K. H. Ho, S. T. Newman, S. Rahimifard, and R. D. Allen, "State of the art in wire electrical discharge machining (WEDM)," *International Journal of Machine Tools and Manufacture,* vol. 44, pp. 1247-1259, 2004.

[134] S. Mahendran, R. Devarajan, T. Nagarajan, and A. Majdi, "A Review of Micro-EDM," in *Proceeding of the International MultiConference of Engineers and Computer Scientists*, Hong Kong, 2010.

[135] L. L. Howell, S. P. Magleby, and B. M. Olsen, "Introduction to Compliant Mechanisms," in *Handbook of Compliant Mechanisms*, ed New York: John Wiley & Sons Ltd., 2013.

[136] Y. Yun and Y. Li, "Optimal design of a 3-PUPU parallel robot with compliant hinges for micromanipulation in a cubic workspace," *Robotics and Computer-Integrated Manufacturing* vol. 27, pp. 977–985, 2011.

[137] C.-H. Liu, W.-Y. Jywe, Y.-R. Jeng, T.-H. Hsu, and Y.-t. Li, "Design and control of a long-traveling nano-positioning stage," *Precision Engineering,* vol. 34, pp. 497-506, 2010.

[138] L. L. Howell and A. Midha, "A Method for the Design of Compliant Mechanisms With Small-Length Flexural Pivots," *Journal of Mechanical Design,* vol. 116, pp. 280-290, 1994.

[139] D. C. Handley, T.-F. Lu, Y. K. Yang, and C. Eales, "Workspace investigation of a 3 DOF compliant micro-motion stage," in *Proceeding of the ICARCV International Conference on Control, Automation, Robotics and Vision* 2004, pp. 1279-1284.

[140] Y. Li and Z. Wu, "Design, analysis and simulation of a novel 3-DOF translational micromanipulator based on the PRB model," *Mechanism and Machine Theory,* vol. 100, pp. 235-258, 2016.

[141] G. Hao, J. Yu, and H. Li, "A Brief Review on Nonlinear Modelling Methods and Applications of Compliant Mechanisms," *Frontiers of Mechanical Engineering,* 2016.

[142] O. A. Turkkan and H. J. Su, "DAS-2D: a concept design tool for compliant mechanisms," *Mech. Sci.,* vol. 7, pp. 135-148, 2016.

[143] V. Kalpathy Venkiteswaran and H.-J. Su, "A 3-Spring Pseudo-Rigid-Body Model for Soft Joints with Significant Elongation Effects," *Journal of Mechanisms and Robotics,* 2016.

[144] V. K. Venkiteswaran and H.-J. Su, "A parameter optimization framework for determining the pseudo-rigid-body model of cantilever-beams," *Precision Engineering,* vol. 40, pp. 46-54, 2015.

[145] A. Midha, S. G. Bapat, A. Mavanthoor, and V. Chinta, "Analysis of a Fixed-Guided Compliant Beam With an Inflection Point Using the Pseudo-Rigid-Body Model Concept," *Journal of Mechanisms and Robotics,* vol. 7, pp. 031007-031007-10, 2015.

[146] Y. Zhang, H.-J. Su, and Q. Liao, "Mobility criteria of compliant mechanisms based on decomposition of compliance matrices," *Mechanism and Machine Theory,* vol. 79, pp. 80-93, 2014.

[147] H.-J. Su, H. Shi, and J. Yu, "A Symbolic Formulation for Analytical Compliance Analysis and Synthesis of Flexure Mechanisms," *Journal of Mechanical Design,* vol. 134, pp. 051009-051009, 2012.

[148] Y. Li, S. Xiao, L. Xi, and Z. Wu, "Design, modeling, control and experiment for a 2-DOF compliant micro-motion stage," *International Journal of Precision Engineering and Manufacturing,* vol. 15, pp. 735-744, 2014.

[149] L.-J. Lai, G.-Y. Gu, and L.-M. Zhu, "Design and control of a decoupled two degree of freedom translational parallel micro-positioning stage," *Review of Scientific Instruments,* vol. 83, p. 045105, 2012.

[150] K.-B. Choi and D.-H. Kim, "Monolithic parallel linear compliant mechanism for two axes ultraprecision linear motion," *Review of Scientific Instruments,* vol. 77, p. 065106, 2006.

[151] H. Shi, H.-J. Su, and N. Dagalakis, "A stiffness model for control and analysis of a MEMS hexapod nanopositioner," *Mechanism and Machine Theory,* vol. 80, pp. 246-264, 2014.

[152] J. Shang, Y. Tian, Z. Li, F. Wang, and K. Cai, "A novel voice coil motor-driven

compliant micropositioning stage based on flexure mechanism," *Review of Scientific Instruments,* vol. 86, p. 095001, 2015.

[153] Y. Du, T. Li, Y. Jiang, and H. Wang, "Design and analysis of a 2-degree-of-freedom flexure-based micro-motion stage," *Advances in Mechanical Engineering,* vol. 8, pp. 1-13, 2016.

[154] H.-H. Phama and I.-M. Chen, "Stiffness modeling of flexure parallel mechanism," *Precision Engineering,* vol. 29, pp. 467–478, 2005.

[155] X. Xiao, Y. Li, and S. Xiao, "Development of a novel large stroke 2-DOF micromanipulator for micro/nano manipulation," *Microsystem Technologies,* pp. 1-11, 2016.

[156] Q. Xu, "Design and Testing of a Novel XY Micropositioning Stage with Dual Ranges and Resolutions," in *Proceeding of the IEEE International Conference on Robotics and Automation (ICRA)*, 2014, pp. 2351-2356.

[157] Q. Xu, "A Modular Two-Axis Compliant Parallel Micropositioning Stage with Long Travel Range," in *Proceeding of the IEEE International Conference on Information and Automation (ICIA)*, 2013, pp. 898-903.

[158] Y. Shimizu, Y. Peng, J. Kaneko, T. Azuma, S. Ito, W. Gao*, et al.*, "Design and construction of the motion mechanism of an XY micro-stage for precision positioning," *Sensors and Actuators A: Physical,* vol. 201, pp. 395-406, 2013.

[159] P. M. Moore, M. Rakotondrabe, C. Clevy, and G. J. Wiens, "Development of a Modular Compliant Microassembly Platform with Integrated Force Measurement Capabilities," in *Proceeding of the 7th International Conference on MicroManufacturing (ICOMM)*, 2012.

[160] S. Xiantao, C. Weihai, Z. Rui, Z. Jianbin, and C. Wenjie, "Development of a flexure-based XY positioning stage for micro/nano manipulation," in *Proceeding of the International Conference on Manipulation, Manufacturing and Measurement on the Nanoscale (3M-NANO)*, 2013, pp. 319-324.

[161] G. Hao, "Extended Nonlinear Analytical Models Of Compliant Parallelogram Mechanisms: Third-Order Models," *Transactions of the Canadian Society for Mechanical Engineering,* vol. 39, pp. 71 - 83, 2014.

[162] G. Hao and H. Li, "Extended Static Modeling and Analysis of Compliant Compound Parallelogram Mechanisms Considering the Initial Internal Axial Force," *Journal of Mechanisms and Robotics,* vol. 8, pp. 041008-041008-11, 2016.

[163] G. Hao and H. Li, "Nonlinear Analytical Modeling and Characteristic Analysis of

a Class of Compound Multibeam Parallelogram Mechanisms," *Journal of Mechanisms and Robotics,* vol. 7, pp. 041016-041016-9, 2015.

[164] S. Awtar, A. H. Slocum, and E. Sevincer, "Characteristics of Beam-Based Flexure Modules," *Journal of Mechanical Design,* vol. 129, pp. 625-639, 2006.

[165] A. Zhang and G. Chen, "A Comprehensive Elliptic Integral Solution to the Large Deflection Problems of Thin Beams in Compliant Mechanisms," *Journal of Mechanisms and Robotics,* vol. 5, pp. 021006-021006, 2013.

[166] P. Wang and Q. Xu, "Design of a compact compliant constant-force XY precision positioning stage," in *Proceeding of the IEEE/ASME International Conference on Mechatronic and Embedded Systems and Applications (MESA)*, 2016, pp. 1-6.

[167] Y. Yun and Y. Li, "A general model of a kind of parallel manipulator for active control based on KANE's dynamics," in *Proceeding of the IEEE Asia Pacific Conference on Circuits and Systems*, 2008, pp. 1830-1833.

[168] Y. Park, "Precision motion control of a three degrees-of-freedom hybrid stage with dual actuators," *IET Control Theory & Applications,* vol. 2, pp. 392-401, 2008.

[169] Y. M. Choi and D. G. Gweon, "A High-Precision Dual-Servo Stage Using Halbach Linear Active Magnetic Bearings," *IEEE/ASME Transactions on Mechatronics,* vol. 16, pp. 925-931, 2011.

[170] J.-C. Shen, C.-H. Wu, B.-Y. Chen, and W.-Y. Jywe, "Control of a Long-stroke Precision Scanning Stage," in *Proceeding of the Mediterranean Conference of Control and Automation (MED)*, 2014, pp. 311-315.

[171] S. Jing-Chung, J. Wen-Yue, L. Qun-Zhong, and W. Chia-Hung, "Control of a High Precision Positioning Stage," in *Proceeding of the 7th IEEE Conference on Industrial Electronics and Applications (ICIEA)*, 2012, pp. 931-935.

[172] F. Wang, C. Liang, Y. Tian, X. Zhao, and D. Zhang, "A Flexure-Based Kinematically Decoupled Micropositioning Stage with a Centimeter Range Dedicated to Micro/nano Manufacturing," *IEEE/ASME Transactions on Mechatronics,* vol. PP, pp. 1-1, 2015.

[173] Y. Song, J. Wang, K. Yang, W. Yin, and Y. Zhu, "A dual-stage control system for high-speed, ultra-precise linear motion," *The International Journal of Advanced Manufacturing Technology,* vol. 48, pp. 633-643, 2009.

[174] H. Zhu, C. K. Pang, and T. J. Teo, "Integrated Servo-Mechanical Design of a Fine Stage for a Coarse-Fine Dual-Stage Positioning System," *IEEE/ASME Transactions on Mechatronics,* vol. 21, pp. 329-338, 2016.

[175] S. Kwon, W. K. Chung, and Y. Youm, "On the Coarse/fine Dual-stage Manipulators with Robust Perturbation Compensator," in *Proceeding of the IEEE International Conference on Robotics and Automation (ICRA)*, 2001, pp. 121-126 vol.1.

[176] L. Zhang, Z. Long, J. Cai, and J. Fang, "Design of a linear macro–micro actuation stage considering vibration isolation," *Advances in Mechanical Engineering,* vol. 7, pp. 1 - 13, 2015.

[177] K. Tadano, T. Arai, K. Kawashima, T. Fujita, and T. Kagawa, "Precise position control of coarse-fine dual stage using pneumatic actuators," in *World Automation Congress (WAC)*, 2010, pp. 1-6.

[178] Y.-T. Liu and B.-J. Li, "Precision positioning device using the combined piezo-VCM actuator with frictional constraint," *Precision Engineering,* vol. 34, pp. 534-545, 2010.

[179] J. Fang, Z. Long, L. Zhang, and L. Nian, "Driving Process and Control Analysis in Macro-micro Dual Stage," in *Proceeding of the IEEE International Conference on Information and Automation (ICIA)*, 2013, pp. 37-42.

[180] G. Y. Gu, L. M. Zhu, C. Y. Su, H. Ding, and S. Fatikow, "Modeling and Control of Piezo-Actuated Nanopositioning Stages: A Survey," *IEEE Transactions on Automation Science and Engineering,* vol. 13, pp. 313-332, 2016.

[181] S. Xiao and Y. Li, "Development of a large working range flexure-based 3-DOF micro-parallel manipulator driven by electromagnetic actuators," in *Proceeding of the IEEE International Conference on Robotics and Automation* 2013, pp. 4506-4511.

[182] N. C. Cheung, "High Performance Linear Actuation Systems," in *Procceding of the International Conference on Power Electronics Systems and Applications*, 2006, pp. 36-39.

[183] K. F. Ehmann, R. E. DeVor, S. G. Kapoor, and J. Cao, "Design and Analysis of Micro/Meso-scale Machine Tools," in *Smart Devices and Machines for Advanced Manufacturing*, ed: Springer London, 2008, pp. 283-318.

[184] G. Hao, "A Multiaxis, Large-Output, Sensing Framework of Integrating Linear Optical Encoders for Nanopositioning Systems," *IEEE Sensors Letters,* vol. 1, pp. 1-4, 2017.

[185] C. Shuo Hung, T. Chung Kai, and C. Hon Chan, "An ultra-precision XY/spl Theta//sub Z/ piezo-micropositioner. II. Experiment and performance," *IEEE Transactions on Ultrasonics, Ferroelectrics, and Frequency Control,* vol. 46, pp.

906-912, 1999.

[186] Q. Liang, D. Zhangc, Z. Chi, Q. Song, Y. Gea, and Y. Ge, "Six-DOF micro-manipulator based on compliant parallel mechanism with integrated force sensor," *Robotics and Computer-Integrated Manufacturing,* vol. 27, pp. 124-134, 2011.

[187] A. E. M. C. Carrozza, A. Menciassi, D. Campolo, S. Micera and P. Dario, "Towards a force-controlled microgripper for assembling biomedical microdevices," *Journal of Micromechanics and Microengineering,* vol. 10, pp. pp. 271-276, 2000.

[188] M. Rakotondrabe, C. Clevy, K. Rabenorosoa, and K. Ncir, "Presentation, Force Estimation and Control of an Instrumented platform dedicated to Automated Micromanipulation Tasks," in *Proceeding of the IEEE Conference on Automation Science and Engineering*, 2010, pp. 722-727.

[189] L. L. Howell, "Pseudo-Rigid-Body-Model," in *Compliant Mechanisms*, ed: John Wiley and Sons, 2001, pp. 135-217.

[190] R. G. Budynas and J. K. Nisbett, "Deflection and Stiffness," in *Shigley's Mechanical Engineering Design*, 9th ed New York: McGraw-Hill, 2011, pp. 148 - 191.

[191] M. Vable, *Mechanics of Materials*, Second Edition ed.: Oxford University Press, 2010.

[192] B. M. Tymrak, M. Kreiger, and J. M. Pearce, "Mechanical properties of components fabricated with open-source 3-D printers under realistic environmental conditions," *Materials & Design,* vol. 58, pp. 242-246, 2014.

[193] M. Jamshidian, E. A. Tehrany, M. Imran, M. Jacquot, and S. Desobry, "Poly-Lactic Acid: Production, Applications, Nanocomposites, and Release Studies," *Comprehensive Reviews in Food Science and Food Safety,* vol. 9, pp. 552-571, 2010.

[194] Y. Koseki, T. Tanikawa, N. Koyachi, and T. Arai, "Kinematic Analysis of Translational 3-DOF Micro Parallel Mechanism Using Matrix Method," in *Proceeding of the IEEE/RSJ International Conference on Intelligent Robots and Systems*, 2000, pp. 786-792 vol.1.

[195] M. Jia, R. P. Jia, and J. J. Yu, "A Compliance-Based Parameterization Approach for Type Synthesis of Flexure Mechanisms," *Journal of Mechanisms and Robotics,* vol. 7, pp. 031014-031014, 2015.

[196] J. M. Selig and X. Ding, "A screw theory of static beams," in *Proceedings of the IEEE/RSJ International Conference on Intelligent Robots and Systems*, 2001, pp.

312-317.

[197] G. R. Fowles and G. L. Cassiday, *Analytical mechanics*: Saunders college, 1999.

[198] S. Timoshenko, "HARMONIC VIBRATIONS OF SYSTEMS HAVING ONE DEGREE OF FREEDOM," in *Vibration Problems in Engineering*, Second ed New-York: D van Nostrand Company, Inc., 1937, pp. 1 - 110.

[199] S. Timoshenko and D. Young, "Vibration Problems in Engineering," ed: D van Nostrand Company, Inc., New-York, 1937.

[200] D. Zhang, Z. Gao, and I. Fassi, "Design optimization of a spatial hybrid mechanism for micromanipulation," *International Journal of Mechanics and Materials in Design,* vol. 7, pp. 55-70, 2011.

[201] G. A. Kumar and P. S. S. Srinivasan, "Design of Force and Displacement Amplifying Compliant Mechanisms- A Multicriteria Optimization Approach," *CURIE Journal,* vol. 2, pp. 23-32, 2009.

[202] Y. Tian, C. Liu, X. Liu, F. Wang, X. Li, Y. Qin*, et al.*, "Design, modelling and characterization of a 2-DOF precision positioning platform," *Transactions of the Institute of Measurement and Control,* vol. 37, pp. 396-405, 2015.

[203] A. Konak, D. W. Coit, and A. E. Smith, "Multi-objective optimization using genetic algorithms: A tutorial," *Reliability Engineering & System Safety,* vol. 91, pp. 992-1007, 2006.

[204] Tamadazte, Brahim, S. Dembélé, G. Fortier, and N. L. Fort-Piat, "Automatic micromanipulation using multiscale visual servoing," in *Proceeding of the IEEE International Conference on Automation Science and Engineering*, 2008, pp. 977-982.

[205] B. Tamadazte, N. L. F. Piat, and S. Dembélé, "Robotic micromanipulation and microassembly using monoview and multiscale visual servoing," *IEEE/ASME Transactions on Mechatronics,* vol. 16, pp. 277-287, 2011.

[206] R. Pieters, P. Jonker, and H. Nijmeijer, "High performance visual servoing for controlled um-positioning," in *Proceeding of the 8th World Congress on Intelligent Control and Automation (WCICA)*, 2010, pp. 379-384.

[207] L. Clark, B. Shirinzadeh, U. Bhagat, and J. Smith, "A vision-based measurement algorithm for micro/nano manipulation," in *IEEE/ASME International Conference on Advanced Intelligent Mechatronics*, Wollongong, Australia, 2013, pp. 100-105.

[208] N. Tan, C. Clévy, G. J. Laurent, P. Sandoz, and N. Chaillet, "Accuracy Quantification and Improvement of Serial Micropositioning Robots for In-Plane

Motions," *IEEE Transactions on Robotics,* vol. 31, pp. 1497-1507, 2015.

[209] N. Tan, C. Clevy, G. J. Laurent, P. Sandoz, and N. Chaillet, "Characterization and compensation of XY micropositioning robots using vision and pseudo-periodic encoded patterns," in *IEEE International Conference on Robotics and Automation (ICRA)*, 2014, pp. 2819-2824.

[210] V. Guelpa, P. Sandoz, C. Clévy, N. L. Fort-Piat, and G. J. Laurent, "Pattern-based vision for microrobotic manipulators calibration and servoing," in *Proceeding of the 13th International Conference on Ubiquitous Robots and Ambient Intelligence (URAI)*, 2016, pp. 308-310.

[211] V. Guelpa, P. Sandoz, M. A. Vergara, C. Clévy, N. Le Fort-Piat, and G. J. Laurent, "2D visual micro-position measurement based on intertwined twin-scale patterns," *Sensors and Actuators A: Physical,* vol. 248, pp. 272-280, 2016.

[212] N. Tan, C. Clévy, G. J. Laurent, and N. Chaillet, "Calibration and validation of XYΘ micropositioners with vision," in *Proceeding of the IEEE/ASME International Conference on Advanced Intelligent Mechatronics (AIM)*, 2012, pp. 256-261.

[213] N. T. Thomopoulos, *Essentials of Monte Carlo simulation: Statistical methods for building simulation models*: Springer Science & Business Media, 2012.

[214] D. P. Landau and K. Binder, *A guide to Monte Carlo simulations in statistical physics*: Cambridge university press, 2014.